

# Development of a Split Hopkinson Bar type machine to measure the impact resistance of bonded joints

*António Francisco de Galhano Tenreiro*

**Master Dissertation**

Supervisor: Prof. Dr. António Manuel Ferreira Mendes Lopes  
Co-supervisors: Inv. Carlos Manuel de Sousa Moreira da Silva  
Prof. Dr. Lucas Filipe Martins da Silva



**Master in Mechanical Engineering**

**Specialization of Automation**

September 2018



*"Measure what is measurable, and make measurable what is not so."*

Galileo Galilei



# Abstract

Adhesive joints are becoming a common manufacturing technique for joining two elements, especially in the automobile and aerospace industry. However, only recently is the scientific community studying adhesives' mechanical behaviour, especially their mechanical behaviour on impact situations. FEUP's Adhesive Group (ADFEUP) and its research fellows are among the scientists studying these materials and bonding techniques. It is in their interests to have a Split Hopkinson Pressure Bar (SHPB) test machine that is able to test adhesives and bonded joints under high speed impact conditions. This work begins the project of designing a SHPB apparatus that is able to test bulk and bonded joint specimen under compression and tensile loads.

At first, a study of the physical behaviour of stress wave propagation on solid bars is made, as well as mathematical models that describe the mechanical and energy behaviour of bars and specimen. Also a literature review of several SHPB Tensile setups and design requirement is made. A study of these requirements applied to adhesive bulk and bonded joint specimens is made, using the mathematical models mentioned beforehand. With the results, a geometry for bonded joint specimen was established, as well as an architecture for the SHPB Tensile and Compression test machine.

In this architecture, a novel pneumatic actuator system was proposed, which needed to be simulated in order to be validated. In this manner, several mathematical models were used to simulate the various dynamics of the actuation system. Results proved that the proposed system can attain high speeds and is able to launch effectively the striking element that will generate the stress wave. With this, the mechanical design of the non-conventional actuator was made, and the various elements of the pneumatic circuit were selected. From this work, a patent proposal of the proposed SHPB setup was submitted.



# Resumo

Juntas adesivas começam a ser uma técnica de fabrico commum para unir duas peças, especialmente na industria automóvel e aeroespacial, Contudo, só recentemente é que a comunidade científica está a estudar o comportamento mecânico de adesivos, especialmente em condições de impacto. O Grupo de Adesivos da FEUP (ADFEUP) e os seus investigadores estão entre os cientistas que estudam estes materiais e tecnicas de adesão. Está no interesse deles ter uma máquina de ensaios do tipo *Split Hopkinson Pressure Bar* (SHPB) que é capaz de testar adesivos e juntas adesivas em condições de impacto a elevadas velocidades. Este trabalho inicia o projeto de dimensionar um dispositivo SHPB que é capaz de testar provetes de adesivos e juntas adesivas a sollicitações de tração e compressão.

Em primeiro lugar, um estudo do comportamento físico da propagação de ondas de tensão em barras sólidas é feito, assim como modelos matemáticos que descrevem o comportamento mecânico e energético das barras e provetes. Uma revisão bibliográfica de vários sistemas SHPB de teste em tração e de requisitos de dimensionamento é feita. Um estudo destes requisitos aplicados a provetes de adesivos e juntas adesivas é feito, usando os modelos matemáticos previamente mencionados. Com estes resultados, a geometria dos provetes de juntas adesivas foram definidas, assim como a arquitetura da máquina SHPB para ensaios de tração e compressão.

Nesta arquitetura, um novo sistema de atuação pneumática é proposto, que necessita de ser simulado de forma a poder ser validado. Desta forma, vários modelos matemáticos foram usados para simular as várias dinâmicas do sistema de atuação. Os resultados provaram que o sistema proposto consegue atingir elevadas velocidades e é capaz de lançar o impactos que irá gerar a onda de tensão. Com isto, o dimensionamento mecânico do atuador não convencional foi feito, e os diversos elementos do circuito pneumático foram escolhidos. Deste trabalho, um pedido de patente do dispositivo SHPB proposto, foi submetido.





# Agradecimentos

Em primeiro lugar, gostava de agradecer aos orientadores, Prof. António Mendes Lopes, Inv. Carlos Moreira da Silva e Prof. Lucas da Silva, pela orientação, disponibilidade, paciência e, acima de tudo, apoio ao longo deste trabalho.

Ao grupo de Adesivos da FEUP (ADFEUP) pela cooperação e apoio ao longo deste projeto. Um agradecimento especial ao Eduardo Marques, ao José Machado e ao Ricardo Carbas pela informação e conselhos fornecidos.

Ao corpo docente e técnicos do Departamento de Engenharia Mecânica (DEMec) pelo apoio, conselho e oportunidades que me deram.

Aos meus amigos pela ajuda e pelo camaradismo destes cinco anos.

Finalmente, à minha família pelo forte apoio que me deram em todo o meu percurso académico e pessoal ao longo do Mestrado, e não só.



# Contents

<b>Abstract</b>	<b>iii</b>
<b>Resumo</b>	<b>v</b>
<b>Agradecimentos</b>	<b>vii</b>
<b>Contents</b>	<b>ix</b>
<b>List of Figures</b>	<b>xi</b>
<b>List of Tables</b>	<b>xiv</b>
<b>List of Symbols</b>	<b>xvii</b>
<b>1 Introduction</b>	<b>1</b>
1.1 Background . . . . .	1
1.2 Motivation . . . . .	1
1.3 Dissertation Goals . . . . .	2
1.4 Layout of the Dissertation . . . . .	3
<b>2 Literature Review</b>	<b>5</b>
2.1 Analysis of the Physical Behavior . . . . .	5
2.1.1 Wave propagation and mechanical impedance . . . . .	7
2.1.2 Reflection and transmission of waves . . . . .	9
2.1.3 Stress and Strain in Specimen . . . . .	12
2.1.4 Energetic study of the Specimen's plastic deformation . . . . .	13
2.2 SHPB Machine architectures for tensile testing . . . . .	15
2.3 SHPB Design Requirements and Recommendations . . . . .	21
<b>3 SHPB Machine Dynamics</b>	<b>25</b>
3.1 Machine Characterization Model . . . . .	25
3.1.1 Considerations . . . . .	25
3.1.2 Actuation Requirements . . . . .	28
3.1.3 Wave Impedance & Stiffness Analysis . . . . .	30

3.2	Results . . . . .	32
3.2.1	Striker Bar Velocity . . . . .	33
3.2.2	Striker Bar Length . . . . .	37
3.2.3	Impedance & Stiffness Ratios . . . . .	40
3.3	Specimen & Bar Specifications . . . . .	45
<b>4</b>	<b>Functional Simulations</b>	<b>51</b>
4.1	Subsystem Models . . . . .	54
4.1.1	Reservoir . . . . .	54
4.1.2	Pneumatic Valves . . . . .	55
4.1.3	Pneumatic Cylinder . . . . .	57
4.1.4	Actuator Mechanics . . . . .	65
4.2	Results . . . . .	69
<b>5</b>	<b>Mechanical Design</b>	<b>73</b>
5.1	Pneumatic Circuit . . . . .	73
5.1.1	Reservoir . . . . .	73
5.1.2	Air Filter & Regulator . . . . .	74
5.1.3	Pneumatic Valves . . . . .	75
5.2	Mechanical Design of the Actuator . . . . .	76
5.2.1	Piston . . . . .	77
5.2.2	Rod . . . . .	79
5.2.3	Head . . . . .	80
5.2.4	Seals and O'rings . . . . .	86
5.2.5	Cylinder Wall . . . . .	87
5.2.6	Mid Support . . . . .	87
5.2.7	Structural Simulations . . . . .	87
<b>6</b>	<b>Conclusions and Future Works</b>	<b>91</b>
6.1	Conclusions . . . . .	91
6.2	Future Works . . . . .	92
	<b>Bibliography</b>	<b>95</b>
<b>A</b>	<b>Machine Characterization</b>	<b>99</b>
A.1	Steel Bars . . . . .	99
A.2	Aluminium Alloy Bars . . . . .	101
A.3	Titanium Alloy Bars . . . . .	106
<b>B</b>	<b>Mechanical Drawings</b>	<b>111</b>
<b>C</b>	<b>Patent Request</b>	<b>125</b>

# List of Figures

1.1	Bonded Joint Specimens for different Loading Modes: (a) Mode I; (b) Mode II; (c) Mixed Mode. . . . .	2
2.1	Simplified representation of a SHPB compression machine. . . . .	5
2.2	Types of loading device Systems of the Kolsky Bar machine: (a) Static Loading; (b) Dynamic Loading. . . . .	6
2.3	Generic loading on a bar: (a) Bar; (b) Infinitesimal Element. . . . .	8
2.4	Simplified representation of the reflection of the displacement and stress wave in the free end side of a bar. . . . .	10
2.5	Representation of the incident, reflected and transmitted waves at the interface between two different bars. . . . .	11
2.6	Representation of stress waves in bars and specimen. . . . .	12
2.7	Tensile SHPB setup by Harding, Wood and Campbell: (a) Elastic Alloy-Bar Assembly; (b) Specimen Inertia-Bar Assembly. . . . .	16
2.8	Specimen used by Harding, Wood and Campbell in their setup. . . . .	17
2.9	SHPB Tension setup designed by Lincoln and Yeakley. . . . .	17
2.10	Schematic SHPB Tension setup designed by Nicholas. . . . .	18
2.11	Direct Loading SHPB Tension setup with tubular Striker. . . . .	19
2.12	Specimen support for direct loading Kolsky machine by Ferreira. . . . .	20
2.13	SHPB Tension setup designed by Gerlach, Kettenbeil and Petrinic. . . . .	20
2.14	Lagrange diagram (or $x - t$ diagram) for Compression Split Hopkinson Bar. . . . .	21
2.15	Incident stress pulse due to mismatched impedance between the striker and the input bars. . . . .	23
3.1	Most used Joint Specimen for SHPB Machines: (a) Single Lap Joint Specimen; (b) Double Lap Joint Specimen. . . . .	26
3.2	Pin loading arrangement. . . . .	26
3.3	Stress-Strain curve for composite materials. . . . .	27
3.4	Schematic representation of a mode II BJS. . . . .	32
3.5	Striker bar velocity required for Stainless Steel bars and specimen of length $L_s = 20$ mm. . . . .	33
3.6	Striker bar velocity required for Aluminium Alloy bars and specimen of length $L_s = 20$ mm. . . . .	34

List of Figures

---

3.7	Striker bar velocity required for Titanium Alloy bars and specimen of length $L_s = 20$ mm. . . . .	34
3.8	Striker bar velocity required for Stainless Steel bars and specimen of length $L_s = 10$ mm. . . . .	35
3.9	Striker bar velocity required for Stainless Steel bars and specimen of length $L_s = 0.2$ mm. . . . .	36
3.10	Striker bar velocity required for Stainless Steel bars and specimen of length $L_s = 2$ mm. . . . .	36
3.11	Striker bar length required for Stainless Steel bars and BJS. . . . .	37
3.12	Striker bar length required for Aluminium Alloy bars and BJS. . . . .	38
3.13	Striker bar length required for Titanium Alloy bars and BJS. . . . .	38
3.14	Striker bar length required for BS of length $L_s = 1$ mm. . . . .	39
3.15	Striker bar length required for BS of length $L_s = 2$ mm. . . . .	40
3.16	Striker bar length required for BS of length $L_s = 5$ mm. . . . .	40
3.17	Ratio comparison for BJS of 20 mm length, with rigid adhesives and Stainless Steel bars. . . . .	41
3.18	Ratio comparison for BJS of 20 mm length, with rigid adhesives and Aluminium Alloy bars. . . . .	41
3.19	Ratio comparison for BJS of 20 mm length, with rigid adhesives and Titanium Alloy bars. . . . .	42
3.20	Ratio comparison for BJS of 20 mm length, with flexible adhesives and Stainless Steel bars. . . . .	43
3.21	Ratio comparison for BJS of 10 mm length, with rigid adhesives and Stainless Steel bars. . . . .	44
3.22	Ratio comparison for BS, with rigid adhesives and Stainless Steel bars. . . . .	44
3.23	Ratio comparison for BS, with flexible adhesives and Stainless Steel bars. . . . .	45
3.24	Designed Bonded Joint Specimen (BJS): (a) Mode I Specimen; (b) Mixed-Mode (Mode I + II) Specimen; (c) Mode II Specimen. . . . .	46
3.25	Adopted SHPB setup architecture: (a) Compression setup; (b) Tensile setup. . . . .	49
4.1	Schematic representation of the non-conventional actuator. . . . .	51
4.2	Proposed Pneumatic Circuit for the Actuator. . . . .	52
4.3	Schematic representation of the actuation system in block diagrams. . . . .	54
4.4	Simulink <sup>®</sup> Model of the Reservoir sub-system. . . . .	55
4.5	Simulink <sup>®</sup> Model of Valve. . . . .	56
4.6	Simulink <sup>®</sup> Pneumatic Cylinder sub-system. . . . .	58
4.7	Simulink <sup>®</sup> model of the Pneumatic Chamber 1, for the Adiabatic Process. . . . .	61
4.8	Schematic representation of leaks between chambers. . . . .	63
4.9	Simulation Model of the Actuator Mechanics. . . . .	66
4.10	Comparison of ACE Shock Absorber Force versus its stroke, with other damping systems. . . . .	68

---

---

4.11	The rod position, $x$ , versus time for the adiabatic ( $n = \gamma = 1.4$ ) and the isothermic ( $n = 1$ ) cases. . . . .	70
4.12	The rod velocity, $\dot{x}$ , versus time for the adiabatic ( $n = \gamma = 1.4$ ) and the isothermic ( $n = 1$ ) cases. . . . .	71
4.13	Pressures, $p_1$ and $p_2$ , as a function of time for the adiabatic ( $n = \gamma = 1.4$ ) and the isothermic ( $n = 1$ ) cases. . . . .	71
5.1	Pressurised gas cylinder from <i>Amtrol-Alfa</i> . . . . .	73
5.2	3D representation of F.R. unit model AC40B-F06D. . . . .	74
5.3	Selected valves: (a) Directional Valve VP 742; (b) SMC <sup>®</sup> Quick Exhaust Valve AQ5000-F06; (c) SMC <sup>®</sup> Check Valve XTO-647. . . . .	75
5.4	Pneumatic Actuator Assembly. . . . .	77
5.5	Cut view of the Piston. . . . .	78
5.6	Front View of Key Ring. . . . .	79
5.7	Rod Design details: (a) Screwed End; (b) Notch to place key rings. . . . .	80
5.8	Isometric views of the Head: (a) Isometric Front View; (b) Isometric Back View. . . . .	80
5.9	Halfway cut of the Head, showing the air bushing and head cap. . . . .	81
5.10	Tensile Load on screws. . . . .	82
5.11	Bending Load on screws. . . . .	83
5.12	Model of the air bushing OAV040MB. . . . .	84
5.13	Halfway cut of the Head, showing the air bushing and head cap. . . . .	85
5.14	Dimensions of sealing elements: (a) O'ring dimensions; (b) Rod Seal dimensions. . . . .	86
5.15	Cut view of the mid support sub assembly. . . . .	88
5.16	Stress distribution on the various elements of the actuator assembly. . . . .	88
5.17	Deflection of the various elements of the actuator in the vertical direction ( $y$ axis). . . . .	89
A.1	Striker bar velocity required for Stainless Steel bars and specimen of length $L_s = 0.1$ mm . . . . .	99
A.2	Striker bar velocity required for Stainless Steel bars and specimen of length $L_s = 0.5$ mm. . . . .	100
A.3	Striker bar velocity required for Stainless Steel bars and specimen of length $L_s = 1$ mm. . . . .	100
A.4	Striker bar velocity required for Aluminium Alloy bars and specimen of length $L_s = 0.1$ mm. . . . .	101
A.5	Striker bar velocity required for Aluminium Alloy bars and specimen of length $L_s = 0.2$ mm. . . . .	101
A.6	Striker bar velocity required for Aluminium Alloy bars and specimen of length $L_s = 0.5$ mm. . . . .	102
A.7	Striker bar velocity required for Aluminium Alloy bars and specimen of length $L_s = 1$ mm. . . . .	102

---

List of Figures

---

A.8 Striker bar velocity required for Aluminium Alloy bars and specimen of length  $L_s = 2$  mm. . . . . 103

A.9 Striker bar velocity required for Aluminium Alloy bars and specimen of length  $L_s = 10$  mm. . . . . 103

A.10 Ratio comparison for BJS of 20 mm length, with flexible adhesives and Aluminium Alloy bars. . . . . 104

A.11 Ratio comparison for BJS of 10 mm length, with rigid adhesives and Aluminium Alloy bars. . . . . 104

A.12 Ratio comparison for BS, with rigid adhesives and Aluminium Alloy bars. 105

A.13 Ratio comparison for BS, with flexible adhesives and Aluminium Alloy bars.105

A.14 Striker bar velocity required for Titanium Alloy bars and specimen of length  $L_s = 0.1$  mm. . . . . 106

A.15 Striker bar velocity required for Titanium Alloy bars and specimen of length  $L_s = 0.2$  mm. . . . . 106

A.16 Striker bar velocity required for Titanium Alloy bars and specimen of length  $L_s = 0.5$  mm. . . . . 107

A.17 Striker bar velocity required for Titanium Alloy bars and specimen of length  $L_s = 1$  mm. . . . . 107

A.18 Striker bar velocity required for Titanium Alloy bars and specimen of length  $L_s = 2$  mm. . . . . 108

A.19 Striker bar velocity required for Titanium Alloy bars and specimen of length  $L_s = 10$  mm. . . . . 108

A.20 Ratio comparison for BJS of 20 mm length, with flexible adhesives and Titanium Alloy bars. . . . . 109

A.21 Ratio comparison for BJS of 10 mm length, with rigid adhesives and Titanium Alloy bars. . . . . 109

A.22 Ratio comparison for BS, with rigid adhesives and Titanium Alloy bars. . 110

A.23 Ratio comparison for BS, with flexible adhesives and Titanium Alloy bars. 110



# List of Tables

3.1	Material properties for bars. . . . .	27
3.2	Material properties for substracts. . . . .	28
4.1	Parameters for simulation of valves. . . . .	57
4.2	Geometric variables and values for <code>Pneumatic Chamber 1</code> and <code>Pneumatic Chamber 2</code> . . . . .	62
4.3	Geometric variables used in <code>iterative_leaks</code> . . . . .	65
4.4	Characteristics of Industrial Shock Absorber CA3X12EU-1. . . . .	68
5.1	Pressurised gas cylinder characteristics. . . . .	74
5.2	Air filter and regulator specifications. . . . .	75
5.3	SMC <sup>®</sup> VP 742 valve flow characteristics. . . . .	75
5.4	SMC <sup>®</sup> VP 742 valve specifications. . . . .	76
5.5	SMC <sup>®</sup> AQ5000-F06 valve specifications. . . . .	76
5.6	SMC <sup>®</sup> XTO-647-04E valve specifications. . . . .	76
5.7	Mechanical properties of Steel material class 8.8. . . . .	81
5.8	OAV <sup>®</sup> bushing model OAV040MB specifications. . . . .	84
5.9	Mechanical properties of Stainless Steel AISI 304. . . . .	85
5.10	O’ring specifications. . . . .	86
5.11	Rod Seal specifications. . . . .	87
5.12	Mechanical properties of Steel Alloy St 52.3. . . . .	87

List of Tables

---

# List of Symbols

## Nomenclature

$A$  Area [ $\text{m}^2$ ]

$A_e$  Effective Area [ $\text{m}^2$ ]

$a$  Crack Length [ $\text{m}$ ]

$b$  Damping Coefficient [ $\text{N s m}^{-1}$ ]

$b^*$  Critical Ratio Pressure [-]

$C$  Sonic Conductance [ $\text{s m}^4 \text{kg}^{-1}$ ]

$c$  Wave Propagation Velocity [ $\text{m s}^{-1}$ ]

$E$  Young Modulus [ $\text{GPa}$ ] or [ $\text{MPa}$ ]

$\bar{E}$  Young Modulus for plane stress [ $\text{GPa}$ ]

$E_D$  Dissipation Energy [ $\text{J}$ ]

$e|_j$  Relative Error of iteration  $j$  [-]

$F$  Force [ $\text{N}$ ]

$f$  Distributed Force per unit length [ $\text{N m}^{-1}$ ]

$G_C$  Critical Energy Release Rate [ $\text{N mm}^{-1}$ ]

$K$  Kinetic Energy [ $\text{J}$ ]

$K_C$  Critical Stress Intensity Factor [ $\text{N m}^{\frac{3}{2}}$ ]

$K_L$  Local Loss Coefficient [-]

$k$  Stiffness [ $\text{N m}^{-1}$ ]

$L$  Length [ $\text{m}$ ]

$l$  Cylinder Stroke [ $\text{m}$ ]

## List of Symbols

---

$m$	Mass [kg]
$\dot{m}$	Mass Flow [kg s <sup>-1</sup> ]
$n$	Polytropic Index [-]
$p$	Pressure [Pa]
$p^*$	Critical Pressure [Pa]
$p_o$	Stagnation Pressure [Pa]
$\dot{Q}$	Heat Transfer [J s <sup>-1</sup> ]
$R$	Specific Gas Constant [J (kg K) <sup>-1</sup> ]
$r_p$	Ratio Pressure [-]
$S$	Auxiliary Variable [-]
$s$	Coefficient of Compressibility Effect [-]
$T$	Temperature [K]
$t$	Time [s]
$U$	Deformation Energy [J]
$u$	Axial Displacement [m]
$V$	Volume [m <sup>3</sup> ]
$\dot{V}$	Rate of Volume Change [m <sup>3</sup> s <sup>-1</sup> ]
$v$	Velocity [m s <sup>-1</sup> ]
$x$	Position [m]
$\dot{x}$	Rod Velocity [m s <sup>-1</sup> ]
$Y$	Parameter for specimen geometry [-]
$Z$	Wave Impedance [N s m <sup>-1</sup> ]
$\alpha_Z$	Impedance Ratio [-]
$\alpha_k$	Stiffness Ratio [-]
$\gamma$	Heat Capacity Ratio [-]
$\Delta K$	Kinetic Energy contribution to the Specimen deformation [J]
$\Delta t$	Loading Time Lapse [s]
$\Delta U$	Deformation Energy contribution to the Specimen deformation [J]
$\dot{\epsilon}$	Strain Rate [s <sup>-1</sup> ]

---

$\mu$  Viscosity [N s m<sup>-2</sup>]  
 $\bar{\mu}$  Dry Friction Coefficient [-]  
 $\nu$  Poisson Coefficient [-]  
 $\rho$  Mass Density [kg m<sup>-3</sup>]  
 $\sigma$  Stress [MPa] or [Pa]  
 $\Psi$  Constants of Leakage Model [various]  
 $\varnothing$  Diameter [m] or [mm]

## Subscripts

*A* referring to the Antechamber  
*Ad* referring to the Adhesive  
*a* referring to the Atmosphere  
*air* referring to the air  
*B* referring to the Bars  
*BS* referring to Bulk Specimen  
*D* referring to the Dead Volume of a chamber  
*d* referring to a variable on an Downstream Point  
*I* referring to Mode I BJS  
*II* referring to Mode II BJS  
*i* referring to the Incident Pulse  
*in* referring to an element that enters  
*l* referring to the Air Leakage  
*out* referring to an element that leaves  
*p* referring to the Pulse/Wave  
*r* referring to the Reflected Pulse  
*R* referring to the fluid reservoir  
*SA* referring to the Shock Absorber  
*SB* referring to the Striker Bar  
*Sp* referring to the Springs

*Sub* referring to the Substract

*s* referring to the Specimen

*t* referring to the Transmitted Pulse

*tr* referring to the Transition from the Antechamber to the Complete Chamber

*u* referring to a variable on an Upstream Point

1 of the First Medium

2 of the Second Medium

## **Abbreviations**

**ADFEUP** FEUP's Adhesives Group

**BJS** Bonded Joint Specimen

**BS** Bulk Specimen

**CFRP** Carbon Fiber Reinforced Polymer

**DIC** Digital Image Correlation

**FEUP** Faculty of Engineering of the University of Porto

**LOME** Laboratory of Optics and Experimental Mechanics

**SHPB** Split Hopkinson Pressure Bar

# Chapter 1

## Introduction

In this chapter, the subject of this dissertation is introduced. As such, this chapter contains a brief background, the motivation, the goals, the methodology employed and the dissertation organization.

### 1.1 Background

An adhesive is a nonmetallic substance capable of joining surfaces of similar or dissimilar materials, which are called substrates or adherents. Historically, adhesive bonding has been recognized and used as a manufacturing technique, but only in the last century it has been applied as a structural mean of joining two components. Therefore, the study of adhesive bonding in engineering and manufacturing is recent and of high interest both to the scientific and industrial communities.

A structural adhesive is a material that can resist significant mechanical loads and that adds strength and stiffness to the bonded structure. It is a common bonding method in high-end industries such as the automotive, the aeronautical and the aerospace industries, where the manufactured products are required to be lightweight.

This bonding technique is common due to its possibility of joining large surfaces and different materials. No heat is necessary to create a joint, thus, the material structure is not altered and no internal stresses or deformations occur. When a load is applied, the stress distribution on the bonded joint is uniform. The adhesive joint is commonly preferred over welded joints or mechanical connections such as screws or rivets [1, 2].

### 1.2 Motivation

Most material properties, such as the yield or the ultimate stresses, are obtained with quasi-static experiments, using conventional testing machines and standardized procedures. While these properties are of importance in the mechanical design of products, they do not reflect the dynamic or impact condition behaviour. Among these conditions

are vehicle collision, impact of a sports ball on a hard surface, bird collision on airplane structures, difference in ambient pressure, etc. For optimal design, quality and safety of a component seeing high-rate loading conditions, material properties and behaviour under these conditions must be determined [3, 4].

Conventionally, strain rates greater than  $\dot{\epsilon} = 1 \text{ s}^{-1}$  are defined as dynamic strain rate conditions. As a reference, conventional tensile test machines can rarely obtain strain rates of  $\dot{\epsilon} = 10 \text{ s}^{-1}$ . Special machines must be designed in order to characterize an adhesive dynamic behaviour, such as the Split Hopkinson Pressure Bar (SHPB). These machines can test materials under strain rates of  $10^2 \text{ s}^{-1}$  to  $10^4 \text{ s}^{-1}$  [4]. Originally, this type of machine was conceived to test materials under dynamic compression loading, but recently, variants of the SHPB machine were developed for tension, torsion, triaxial and axial/shear combination tests [3].

The study and analysis of adhesive and adhesive bonds is gaining importance in the scientific and industrial communities, specially under dynamic conditions. The FEUP's Adhesives Group (ADFEUP) is responsible for various research projects in this field and has several test machines for various loading conditions. Among these, there is a Drop-weight test machine, a dynamic loading test machine with impact velocities of up to  $5 \text{ m}\cdot\text{s}^{-1}$  [5]. Although this machine can help characterize adhesive bonds under dynamic behaviour, its test range is limited. Therefore, a SHPB testing machine has been requested by ADFEUP.

### 1.3 Dissertation Goals

The main goal of this dissertation is to design a SHPB Test Machine that can measure impact resistance of bonded joints in mode I, mode II and mixed mode (I + II), like it is shown in Figure 1.1, as well as Bulk Specimen. With this, ADFEUP should be able to determine the Mechanical Properties and Fracture Mechanics behaviour of adhesives in bonded joints with different orientations.

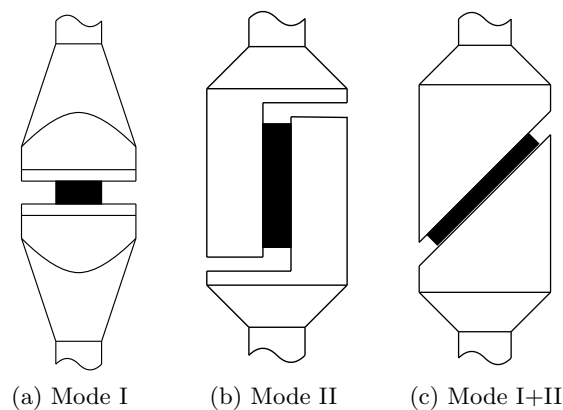


Figure 1.1: Bonded Joint Specimens for different Loading Modes [6].



In case one is testing with adhesive bulk specimen, one should note that these materials can have a Young's modulus,  $E$ , that can range from 1 MPa to 4 GPa. In the case of bonded joint testing, the specimen's substrate can be of Carbon Fiber Reinforced Polymers (CFRP) ( $E = 108$  GPa), an Aluminium Alloy ( $E \approx 72,4$  GPa) or Steel ( $E \approx 210$  GPa) [7].

The machine should be able to test specimens with a strain rate that can vary from  $\dot{\epsilon}_s = 1500 \text{ s}^{-1}$  to  $10^4 \text{ s}^{-1}$ . The specimen should not be visibly obstructed by any machine component, because it is the intent of ADFEUP to implement high-speed cameras to record a specimen's behaviour during a test, as well as have some measurement of the strain field.

Given that ADFEUP already uses specimens with specific geometries for impact testing on the Drop-weight test machine, it was suggested that the specimen should have the same diameter,  $\varnothing_s = 12.5$  mm.

## 1.4 Layout of the Dissertation

This dissertation is divided into six chapters that cover the developed work on the SHPB test machine setup and its actuation system. In this present chapter, an introduction of the project is made.

In Chapter 2, a literature review of the SHPB setup is presented. Firstly, a study on unidirectional wave mechanics is made, describing physically and mathematically its behaviour. Afterwards, a brief description of several SHPB Tensile test machines is made, and lastly, several design requirements and recommendations are listed.

Chapter 3 presents a mathematical study of both the requirements found on the the literature review, as well as the project requirements, in order to establish geometric and cinematic restrictions on the design of the machine elements.

Chapter 4 delves on the functional simulations made to define the architecture of the actuation system of the test machine. As such, firstly a study of several models based on physical laws is presented, and afterwards an analysis of several architectures is made, in order to determine a stable and functional architecture.

Chapter 5 presents the mechanical design of the actuator, as well as it's pneumatic circuit.

Lastly, Chapter 6 concludes this dissertation and presents a proposal for future works based on work done.



## Chapter 2

# Literature Review

A Split Hopkinson Pressure Bar (SHPB), also known as a Kolsky Bar, is a test machine specifically for the study of materials under impact and high strain rate solicitations. In the first section of this chapter, a literature review of the physical phenomena responsible for the behavior of the SHPB is presented. In the second section, a description of case studies of Kolsky bar machines is discussed. Lastly, the third section presents some requirements and recommendations for the design of SHPB machines.

### 2.1 Analysis of the Physical Behavior

In recent years, the scope of applications of the Kolsky Bar method has been extended to several loading conditions, such as tension stress state, torsion, triaxial stress state and axial-shear stress state combination. The differences between these versions of the machine are the loading methods and the specimen gripping systems.

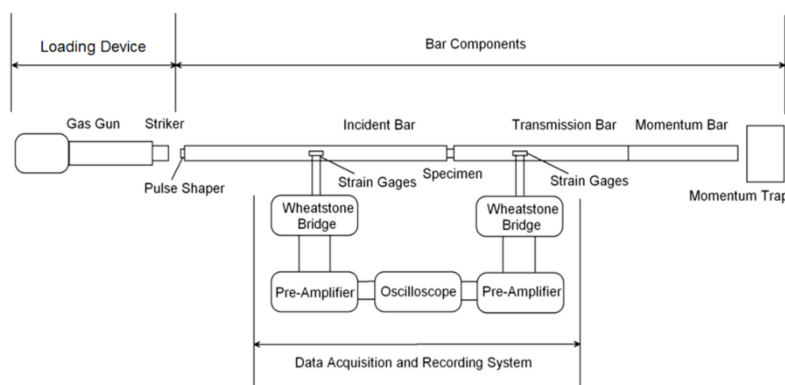


Figure 2.1: Simplified representation of a SHPB compression machine [3].

The SHPB test machine consists of an actuator/loading device, bar components (composed by the striker bar, the incident bar, the transmission bar and the momentum

trap device) and the data acquisition system, shown in Figure 2.1.

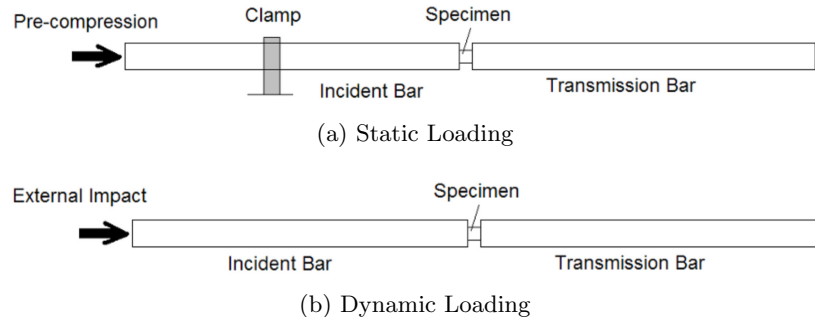


Figure 2.2: Types of loading device Systems of the Kolsky Bar machine [3].

The actuator/loading device system should be controllable, stable and repeatable. There are two loading methods for the actuation of a test: the static loading type and the dynamic loading type, represented in Figure 2.2. In the static loading type, part of the incident bar between the free end and a clamp is statically loaded in compression. When the clamp is released, the deformation energy stored in this section of the bar is transmitted to the rest of the incident bar. This produces a compression wave propagating in the incident bar towards the specimen [3].

The dynamic loading type, more commonly used in Kolsky Bar machines, is to launch a striker bar that impacts on the incident bar, generating a compression stress wave. Gas guns and pneumatic actuation systems have been widely used in this type of machines, since they are efficient, controllable and safe. The striker bar is launched by a sudden increase in pressure and accelerates in a gun barrel [3, 4]. Sometimes, gas venting holes are drilled on the side of the gun barrel near the exit, in order to have an impact between the striker and the incident bars at constant velocity. Although this system is common, other actuation systems, such as hydraulic or electromechanical linear actuators, have been adopted.

The striking speed can be adjusted by changing the pressure of the gas, or by changing the depth of the striker inside the gas gun. The striking velocities are either measured optically or magnetically just before the impact [3].

A SHPB machine has two bars, one on each side of the specimen: The incident bar, also known as the input bar, and the transmission bar, also known as the output bar. The incident bar is struck by the striker bar, that has been launched by the gun barrel, and, at the moment of impact, a compressive stress wave is generated. This wave is propagated towards the specimen. When the wave reaches the interface between the input bar and the specimen, part of the wave is reflected back towards the free end of the incident bar, and the other part of the stress wave is transmitted to the specimen. Afterwards, the transmitted wave reaches the interface between the specimen and the output bar and is divided into a reflected wave and a transmitted wave that propagates on the output bar. These phenomena will be further explained in the following subsections.

At the end of the free side of the output bar, a momentum trap device is installed in order to absorb the transmitted wave and motion.

In scope of the test machine, there must be associated a data acquisition and recording system, in order to have exact measurements, as well as a processing of the gathered information. The stress waves previously described, which must be elastic in nature, generating strains as defined by the Hooke law. It is standard to measure the generated strains using strain gauges on a Wheatstone bridge electrical circuit. Since the signal measured is of small amplitude (of order of magnitude  $10^{-3}$  V), a signal amplifier is required. Afterwards, the amplified signal is read by an oscilloscope or a high-rate data-acquisition system and the signal is sent to a PC. There is also a measuring system for the speed of the striker bar. Often, a laser-beam measurement system is used. A transmitter generates a parallel light curtain, and when the striker bar moves, it progressively blocks the laser light curtain. The light receiver measures this change in light intensity and sends an analog voltage signal, that is read by the data-acquisition system.

It should be noted that this is a test machine with a open-loop feedback control system for the loading conditions imposed on the specimen. This means that the definition of the loading conditions applied to the specimen will not be adjusted in real-time based on the previous measurements acquired with the data-acquisition system. In fact, the experiments must be done by trial and error, in order to obtain the desired testing conditions.

Recently, the Digital Image Correlation (DIC) was implemented in experimental set-ups, including the SHPB apparatus. The DIC is a non-contact measurement method that provides the measurement of deformation of the specimen. A pattern with high contrast is applied on the specimen's surface and a high-speed digital camera is used to obtain images of the changes in the applied pattern, when the specimen is under high-speed deformation. The patterns in the images are correlated with the field deformation of the specimen. The DIC method can also be applied for 3D deformation field measurements using two high-speed synchronized cameras [3].

### 2.1.1 Wave propagation and mechanical impedance

Consider that the bar shown in Figure 2.3a, of constant cross-section area,  $A(x) = A$  and length,  $L$ , is loaded with an axial distributed force (per unit length),  $f(x, t)$ , causing an axial displacement,  $u(x, t)$ . Let us assume the free body diagram of an infinitesimal element of that bar, shown in Figure 2.3b, of length  $dx$ . Consider also that the bar has a mass density,  $\rho(x) = \rho$ , and an elastic modulus,  $E(x) = E$ .

Applying the Newton's 2<sup>nd</sup> law of motion to the infinitesimal element shown in Figure 2.3b, leads to the following equation

$$(F(x, t) + dF(x, t)) - F(x, t) + f(x, t)dx = \rho A dx \frac{\partial^2 u(x, t)}{\partial t^2} \quad (2.1)$$

Considering that  $f(x, t) = 0$  and simplifying equation (2.1), comes

$$dF(x, t) = \rho A dx \frac{\partial^2 u(x, t)}{\partial t^2} \quad (2.2)$$

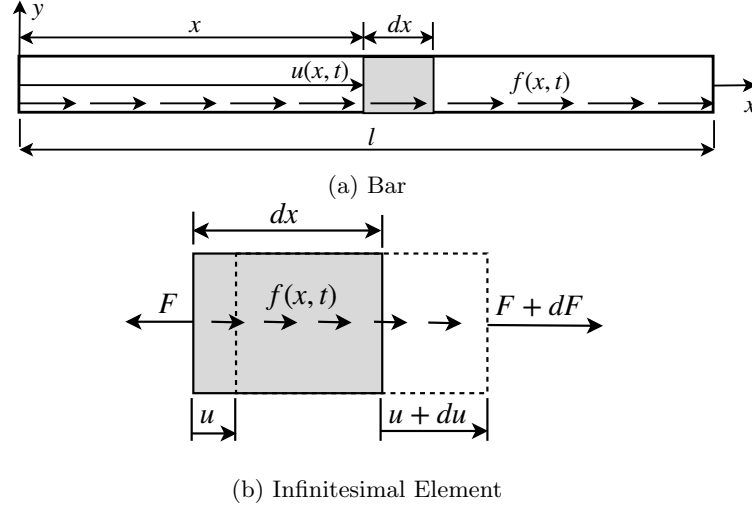


Figure 2.3: Generic loading on a bar.

Considering the Hooke's Law applied to the force  $F(x, t)$ , the following relation is obtained

$$F(x, t) = EA \frac{\partial u(x, t)}{\partial x} \quad (2.3)$$

Deriving equation (2.3) yields

$$dF(x, t) = \frac{\partial F(x, t)}{\partial x} dx = EA \frac{\partial^2 u(x, t)}{\partial x^2} dx \quad (2.4)$$

Replacing (2.4) in equation (2.2), one obtains

$$\frac{\partial^2 u(x, t)}{\partial x^2} = \frac{\rho}{E} \frac{\partial^2 u(x, t)}{\partial t^2} \Leftrightarrow \frac{\partial^2 u(x, t)}{\partial x^2} = \frac{1}{c^2} \frac{\partial^2 u(x, t)}{\partial t^2} \quad (2.5)$$

where  $c = \sqrt{\frac{E}{\rho}}$  is the wave propagation velocity on the bar. Equation (2.5) is known as the one-dimensional differential Wave equation, and can be solved by applying the d'Alembert solution [4, 8, 9, 10, 11]. After applying the transformation of variables  $v^*$  and  $w^*$

$$v^* = x + ct \wedge w^* = x - ct$$

one can obtain the axial displacement equation for a wave,  $u(x, t)$  [8, 9]

$$u(x, t) = f(x - ct) + g(x + ct) \quad (2.6)$$

where  $f(x - ct)$  and  $g(x + ct)$  are functions that correspond to waves traveling in positive and negative  $x$  direction respectively, illustrated in Figure 2.3. One must note that, while these two functions are arbitrary, they must satisfy initial conditions [4, 9, 10, 11]. Considering that the wave propagates in the positive direction, it comes that  $u(x, t) = f(x - ct)$ . Differentiating the axial displacement leads to the axial strain, such that

$$\varepsilon(x, t) = \frac{\partial u(x, t)}{\partial x} = f'(x - ct) \quad (2.7)$$

Rewriting equation (2.3), one obtains

$$F(x, t) = EA \frac{\partial u(x, t)}{\partial x} = EA \varepsilon(x, t) \quad (2.8)$$

The velocity,  $v(x, t)$ , of a particle in the bar that moves due to the wave, can be determined as

$$v(x, t) = \frac{\partial u(x, t)}{\partial t} = \begin{cases} -c \varepsilon(x, t) & \text{if } u(x, t) = f(x - ct); \\ c \varepsilon(x, t) & \text{if } u(x, t) = g(x + ct) \end{cases} \quad (2.9)$$

The Impedance of the bar,  $Z$ , is defined with equations (2.8) and (2.9), resulting

$$Z = \frac{F}{v} = \mp \frac{EA}{c} = \mp \rho A c = \mp A \sqrt{\rho E} \quad (2.10)$$

This means that the impedance of a bar is defined by its diameter,  $\varnothing$ , and by the bar material's properties. One should note that the  $\mp$  sign refers to the cases of positive and negative displacement, respectively [4, 10, 11]. When talking of the wave impedance, one normally consider its modulus,  $|Z|$ .

### 2.1.2 Reflection and transmission of waves

The equations presented in section 2.1.1 were defined for a rod with infinite length. Nevertheless, the bars of the Kolsky Bar test machine have a finite length, and therefore, the boundaries of the rods have to be considered. When an incident wave reaches a boundary, it may occur either a reflection of the wave, or both a reflection of the wave (through the same medium), and the transmission of the wave to the adjacent medium. Such phenomena depend on the boundary conditions. This sub-section analyzes only the boundary conditions that reflect the mechanical behaviour of the SHPB machine: Free-end boundary conditions, and interface between bars and specimen.

When a rod has a free-end at  $x = 0$ , its boundary condition is given by

$$\frac{\partial u(0, t)}{\partial x} = 0 \quad (2.11)$$

Considering that the displacement is given by equation (2.6), it can be obtained that

$$\frac{\partial u(0, t)}{\partial x} = f'(0 - c_B t) + g'(0 + c_B t) = 0 \quad (2.12)$$

and, therefore

$$f'(-c_B t) = -g'(c_B t) \Leftrightarrow f(-c_B t) = -g(c_B t) \quad (2.13)$$

which means that, when a compression wave reaches the free end of a rod, it becomes a tension wave, and vice-versa, as represented in Figure 2.4.

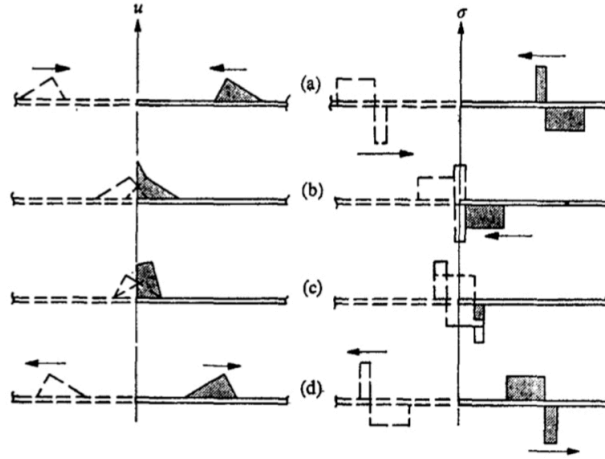


Figure 2.4: Simplified representation of the reflection of the displacement and stress wave in the free end side of a bar [4, 10].

When the wave reaches the free end of the bar, the superposition of both the incident and the reflected waves occurs. It can be observed in Figure 2.4 (b) and (c) that, when this superposition is generated, the displacement of the rod particles increases, as described by equation (2.6). Conversely to the displacement, there are tension and compression stress waves that, when superposed, nullify themselves. This means that the free end will have no stress.

Now, the second boundary condition is analyzed. When there are two rods of different cross-section areas,  $A_1$ ,  $A_2$ , of different mass density,  $\rho_1$ ,  $\rho_2$ , and of different Young moduli,  $E_1$ ,  $E_2$ , such as represented in Figure 2.5, one part of the incident wave is transmitted to the next bar, and the other part is reflected backwards. The displacements of any particle due to the incident wave,  $u_i$ , due to the reflected wave,  $u_r$ , and due to the transmitted wave,  $u_t$ , are given by

$$u_i = u_i(x - c_1 t) \quad (2.14a)$$

$$u_r = u_r(x + c_1 t) \quad (2.14b)$$

$$u_t = u_t(x - c_2 t) \quad (2.14c)$$

Considering Hooke's law, defined in equation (2.3), one obtains the corresponding incident stress wave,  $\sigma_i$ , reflected stress wave,  $\sigma_r$ , and transmitted stress wave,  $\sigma_t$ , from (2.14)



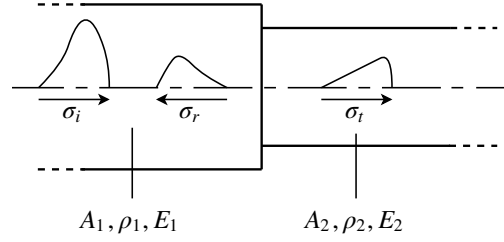


Figure 2.5: Representation of the incident, reflected and transmitted waves at the interface between two different bars [10].

$$\sigma_i = E_1 u'_i(x - c_1 t) \quad (2.15a)$$

$$\sigma_r = E_1 u'_r(x + c_1 t) \quad (2.15b)$$

$$\sigma_t = E_2 u'_t(x - c_2 t) \quad (2.15c)$$

The velocity of the incident wave,  $v_i$ , reflected wave,  $v_r$ , and transmitted wave,  $v_t$ , can be determined according to equation (2.9), yielding

$$v_i = -c_1 u'_i(x - c_1 t) \quad (2.16a)$$

$$v_r = c_1 u'_r(x + c_1 t) \quad (2.16b)$$

$$v_t = -c_2 u'_t(x - c_2 t) \quad (2.16c)$$

For the interface between the rods, shown in Figure 2.5, the balance of forces and the continuity of velocities must hold. Thus, the boundary conditions are

$$A_1 (\sigma_i + \sigma_r) = A_2 \sigma_t \quad (2.17a)$$

$$v_i = v_t - v_r \quad (2.17b)$$

Applying the definitions in equations (2.15) and (2.16) to the equation (2.17), we obtain the transmitted stress wave,  $\sigma_t$ , and the reflected stress wave,  $\sigma_r$ , as a function of the incident stress wave,  $\sigma_i$ , such that

$$\sigma_t = \frac{2A_1\rho_2c_2}{A_1\rho_1c_1 + A_2\rho_2c_2}\sigma_i \quad (2.18a)$$

$$\sigma_r = \frac{A_1\rho_1c_1 - A_2\rho_2c_2}{A_1\rho_1c_1 + A_2\rho_2c_2}\sigma_i \quad (2.18b)$$

From these expressions, one can determine that the reflected and transmitted pulses generated at the interface between the two bars depends on their impedances [10]. From Figure 2.6, one concludes that these two equations are verified for the interface between the incident bar and the specimen and the interface between the specimen and the transmission bar.

### 2.1.3 Stress and Strain in Specimen

As seen in section 2.1.2, when there is a change in impedance, the incident wave is divided in one reflected wave and one transmitted wave. This phenomenon occurs when the incident wave reaches the interface between the input bar and the specimen, as represented in Figure 2.6. If plastic deformation of the specimen is observed, then the amplitudes of the transmitted and reflected pulses may vary, because both the cross-section area and the mechanical properties of the specimen vary with deformation [11].

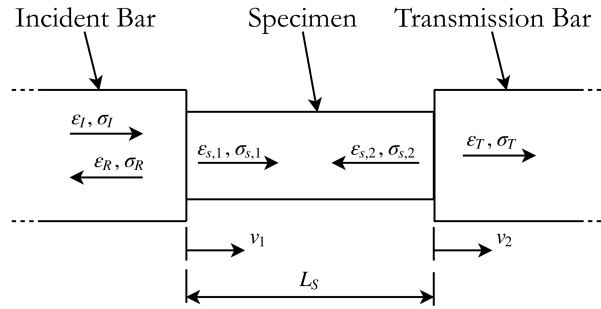


Figure 2.6: Representation of stress waves in bars and specimen [4, 10, 11].

One can write the velocity of a particle in the interface between the incident bar and the specimen,  $v_1$ , as well as the velocity of a particle in the interface between the specimen and the transmission bar,  $v_2$ , as

$$v_1 = c_B (\varepsilon_i - \varepsilon_r) \quad (2.19a)$$

$$v_2 = c_B \varepsilon_t \quad (2.19b)$$

The equation for the specimen strain-rate,  $\dot{\varepsilon}_s$ , is defined as

$$\dot{\varepsilon}_s = \frac{v_1 - v_2}{L_s} = \frac{c_B}{L_s} (\varepsilon_i - \varepsilon_r - \varepsilon_t) \quad (2.20)$$

When applying the force balance in the interface between the incident bar and the specimen, one obtains the transmitted stress to the specimen,  $\sigma_1$ , such that

$$\sigma_1 = \frac{A_B}{A_s} E_B (\varepsilon_i + \varepsilon_r) \quad (2.21)$$

where,  $A_B$ , is the cross-section of a bar (both incident and transmission bars),  $A_s$  is the cross-section of a specimen, and,  $E_B$ , is the Young's modulus of the bars. At the interface between the specimen and the transmission bar, one is able to determine the incident stress to the specimen,  $\sigma_2$ , with the force balance equation

$$\sigma_2 = \frac{A_B}{A_s} E_B \varepsilon_t \quad (2.22)$$

Considering that the specimen is at stress equilibrium, one has that

$$\sigma_1 = \sigma_2 \Leftrightarrow \varepsilon_t = \varepsilon_i + \varepsilon_r \quad (2.23)$$

This assumption must be verified in a Kolsky Bar test machine, when fulfilling the dynamic characterization of materials properties. This means that the specimen deforms almost uniformly, and the specimen response over its volume is a good approximation of a material response on a given point. Applying equation (2.23) in equation (2.20), yields

$$\dot{\varepsilon}_s = -2 \frac{c_B}{L_s} \varepsilon_r \quad (2.24)$$

The specimen strain,  $\varepsilon_s$ , is obtained by integrating equation (2.24), yielding

$$\varepsilon_s = -2 \frac{c_B}{L_s} \int_0^t \varepsilon_r dt \quad (2.25)$$

The stress applied in the specimen,  $\sigma_s$ , is

$$\sigma_1 = \sigma_2 = \sigma_s = \frac{A_B}{A_s} E_B \varepsilon_t \quad (2.26)$$

One should note that, when the specimen equilibrium is not verified, one can define an averaged specimen stress,  $\bar{\sigma}_s$ , following the expression

$$\bar{\sigma}_s = \frac{1}{2} (\sigma_1 + \sigma_2) = \frac{1}{2} \frac{A_B}{A_s} E_B (\varepsilon_t + \varepsilon_i + \varepsilon_r) \quad (2.27)$$

#### 2.1.4 Energetic study of the Specimen's plastic deformation

The incident stress-strain wave generated by the impact between the striker and the incident bars is associated with an amount of energy that causes the plastic deformation of the specimen. In order to determine the necessary amount energy required for the actuating system, one must first study the energetic behaviour of a SHPB test.

The elastic strain energy carried out by the incident wave,  $U_i$ , can be calculated as an average value

$$U_i = V \int_0^{\varepsilon_i} \sigma d\varepsilon \quad (2.28)$$

where  $V$  is the deformed volume of the incident bar. This deformed volume is only a portion of the incident bar, since it is only dependent on the loading time lapse,  $\Delta t$ , of the striker bar. Therefore, the volume  $V$  can be defined as

$$V = A_B c_B \Delta t \quad (2.29)$$

One should also note that the stress waves that pass through the bars have amplitudes below the yield stress of the Bar material; therefore, this is an elastic wave,

where  $\sigma = E_B \varepsilon$ . Equation (2.28) can be rewritten as

$$U_i = A_B c_B \Delta t E_B \int_0^{\varepsilon_i} \varepsilon d\varepsilon = A_B c_B \Delta t E_B \frac{\varepsilon_i^2}{2} \quad (2.30)$$

The same deduction can be made for determining the elastic strain energy associated with the reflected and transmitted waves,  $U_r$  and  $U_t$ , respectively.

$$U_r = A_B c_B \Delta t E_B \frac{\varepsilon_r^2}{2} \quad (2.31a)$$

$$U_t = A_B c_B \Delta t E_B \frac{\varepsilon_t^2}{2} \quad (2.31b)$$

Once having the three components, the contribution of elastic strain energy to the specimen deformation,  $\Delta U$ , can be determined.

$$\Delta U = U_i - U_t - U_r = \frac{1}{2} A_B c_B \Delta t E_B (\varepsilon_i^2 - \varepsilon_t^2 - \varepsilon_r^2) \quad (2.32)$$

When the specimen is under dynamic stress equilibrium, equation (2.23) is verified, and equation (2.32) can be rewritten as

$$\Delta U = -A_B c_B \Delta t E_B \varepsilon_r \varepsilon_t \quad (2.33)$$

It should be noted that, in equation (2.33), the energy difference is positive, since the reflected and the transmitted strains,  $\varepsilon_t$  and  $\varepsilon_r$ , respectively, have opposite signs.

There is also the contribution of the kinetic energy to the plastic deformation of the specimen. Considering that the kinetic energy of the incident bar after elapsing the incident wave,  $K_i$ , is defined as

$$K_i = \frac{1}{2} m v_i^2 \quad (2.34)$$

where  $m$  and  $v_i$  are respectively, the mass of the deformed portion of the input bar, and the particle velocity when a wave passes through. The mass,  $m$ , can be defined as

$$m = \rho_B V = \rho_B A_B c_B \Delta t \quad (2.35)$$

where  $\rho_B$  is the bar's mass density. The velocity of a particle when a incident wave passes through the input bar can be obtained from equation (2.19), where  $v_1 = v_i - v_r$ . This means that  $v_i = c_B \varepsilon_i$  and equation (2.34) can be rewritten as

$$K_i = \frac{1}{2} \rho_B A_B c_B^3 \Delta t \varepsilon_i^2 \quad (2.36)$$

The same principles can be applied to determine the kinetic energy of a particle

associated with the reflected and transmitted waves,  $K_r$  and  $K_t$ , respectively, so that

$$K_r = \frac{1}{2} \rho_B A_B c_B^3 \Delta t \varepsilon_r^2 \quad (2.37a)$$

$$K_t = \frac{1}{2} \rho_B A_B c_B^3 \Delta t \varepsilon_t^2 \quad (2.37b)$$

With these kinetic energies, the contribution of kinetic energy to the specimen deformation,  $\Delta K$ , can be obtained,

$$\Delta K = K_i - K_t - K_r = \frac{1}{2} \rho_B A_B c_B^3 \Delta t (\varepsilon_i^2 - \varepsilon_t^2 - \varepsilon_r^2) \quad (2.38)$$

When the specimen is in stress equilibrium, equation (2.23) is verified and equation (2.38) simplifies to

$$\Delta K = -\rho_B A_B c_B^3 \Delta t \varepsilon_r \varepsilon_t \quad (2.39)$$

Since the incident and transmission bars must work in the elastic domain and, using the mathematical definition of wave propagation velocity on a bar, equation (2.39) can be simplified

$$\Delta K = -A_B c_B E_B \Delta t \varepsilon_r \varepsilon_t \quad (2.40)$$

It should be noted that equations (2.33) and (2.40), for  $E_U$  and  $E_K$ , respectively, are identical.

Assuming that the specimen has a perfectly plastic response, the specimen deformation energy,  $U_s$ , can be defined as

$$U_s = A_s L_s \sigma_s \varepsilon_s \quad (2.41)$$

where  $A_s$  and  $L_s$  are the initial cross-section area and length of the Specimen, respectively. The specimen's yield strength,  $\sigma_s$ , and plastic strain,  $\varepsilon_s$ , are the defined in equations (2.26) and (2.25), respectively. In equation (2.25), the time integral of the reflected strain can be simplified and, equation (2.41) is rewritten as

$$U_s = -2 A_B c_B E_B \Delta t \varepsilon_r \varepsilon_t = \Delta K + \Delta U \quad (2.42)$$

It can be seen from equation (2.42) that the energy required for plastic deformation of the specimen is the sum of two identical energy components, which are the kinetic energy,  $\Delta K$ , and the elastic strain energy from the bars,  $\Delta U$ . It should be noted that this analysis doesn't include the kinetic energy of the specimen [3].

## 2.2 SHPB Machine architectures for tensile testing

The Split-Hopkinson Pressure Bar, presented in section 2.1, was conceived by Kolsky in 1949 and could only perform high-strain rate compression tests. Since the

---

1960's, several versions of the Kolsky Bar for tensile tests were conceived [3]. In this section, a description of several SHPB Tensile test machines is presented.

One of the first machine setups designed specifically to test materials in tension was developed by Harding, Wood and Campbell in 1960. The pressure bar setup is presented in Figure 2.7a and 2.7b. In this design, the compression impact is generated on the free end of the hollow weightbar, leading to a compression stress wave that travels towards the yoke. The yoke connects the weightbar to the alloy bar. When the generated compression wave reaches the extremity of the yoke, it becomes a tensile stress wave that travels towards the alloy bar and the hollow weightbar. Strain gauges measure the resultant wave and, with that information, one can adjust the input loading condition.

Afterwards, the specimen assembly shown in Figure 2.7b replaces the alloy bar assembly setup and a dynamic tension test is made under the same loading conditions. In this assembly, strain gauges are located on the yoke and on the inertia bar, made of the same material as the alloy bar. The specimen, shown in Figure 2.8, is fixed in both ends with threads [3, 12].

This tension test setup was latter modified by Harding and Welsh in 1983. They implemented the traditional incident and transmission pressure bars inside the hollow weightbar, in order to to test composite specimen under tensile high-strain rate conditions. Hauser also made a similar design, where both input and output bars were inside a hollow transmitter bar. This hollow bar has a tubular impact cross-section.

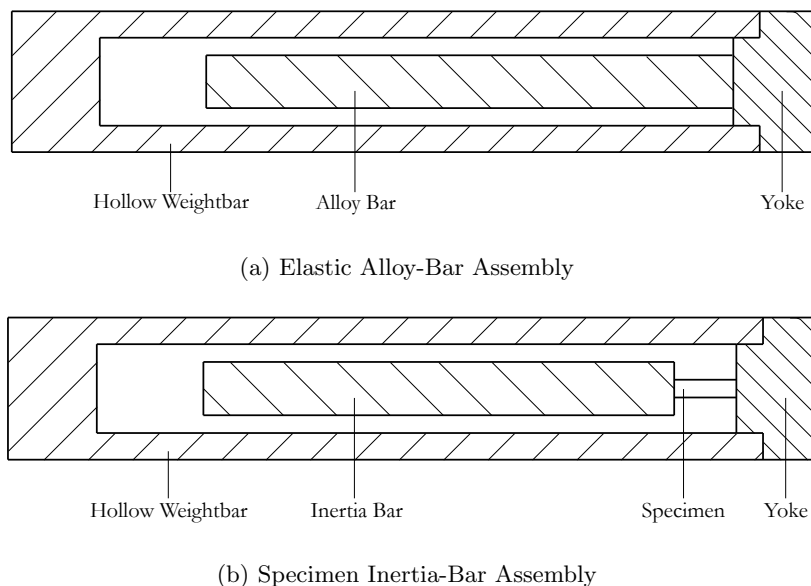


Figure 2.7: Tensile SHPB setup by Harding, Wood and Campbell [3, 12].

This setup is quite easy to use, since it works in a similar way as the original Compression SHPB setup. It also has the benefit of verifying that the striker bar is

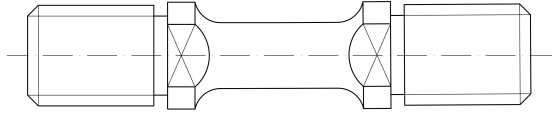


Figure 2.8: Specimen used by Harding, Wood and Campbell in their setup [12].

aligned with the hollow weightbar [12]. However, the setup is inside a tubular solid bar, which is inefficient in terms of instrumentation, since it forces the drilling of holes in the weightbar in order to have the electrical wiring from the strain gauges to the DAQ system. Also, this machine design does not allow any type of visual observation system of the specimen deformation process [3]. Furthermore, the existence of the yoke as a connector between the tubular bar and the specimen (or the input bar) may cause a slight reduction in the stress wave velocity [12].

Afterwards, Lincoln and Yeakley proposed in 1968 a tensile Kolsky test design, where a "top hat" specimen is placed between a solid incident bar and a tubular transmission bar, shown in Figure 2.9. The incident compression wave reaches the inside of the specimen from the incident bar, and causes a tensile solicitation on the specimen gage section. Afterwards, the tensile load is transmitted to the transmission bar as a compression wave.

In order to increase the resulting tension stress amplitude, the tube portion of the "hat-type" specimen was divided in four arms with a length to width ratio of approximately 2 to 1. Due to the unusual specimen geometry, the authors compared its stress-strain behaviour with the ASTM standard of  $\frac{1}{2}$  inches diameter tensile test specimen [3, 13]. This study revealed that both specimens had a similar stress-strain behaviour up to 30% strain, indicating that the geometry used in this specimen had no significant effect in the tension loading conditions [13].

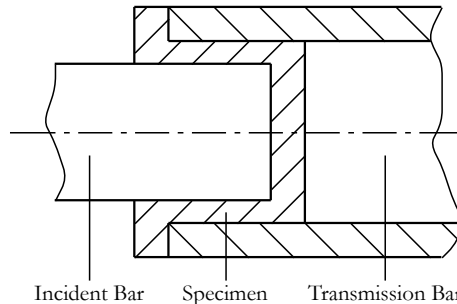


Figure 2.9: SHPB Tension setup designed by Lincoln and Yeakley [3, 11, 13].

This SHPB Tensile setup was designed with both input and output bars having the same cross-section area, ensuring that condition presented in equation (2.23) is true. Furthermore, the design does not need excessive modifications to the Compression SHPB setup. Also, this setup does not require the user to attach the the specimen to the bars using threaded connections, which may add uncertainty to wave transmission

[3, 13]. Unfortunately, this machine design allows only the testing of processed metallic specimens and composite material specimens [11].

In 1981, Nicholas proposed an alternative SHPB Tensile test machine, also very similar in behaviour to the traditional Compression test machine. The actuation system, which is identical to the Compression SHPB machine, is composed of a striker bar that is launched by a gas gun and that strikes the incident bar generating a compression wave. The specimen is threaded on both ends, so that it remains fixed to both the incident and transmission bars. A collar, made of the same material as the pressure bars, is placed over the specimen and has contact with both the incident and transmission bars. When the compression wave reaches the interface between the incident bar and the specimen/collar, it passes through both elements, leaving, ideally, the specimen undeformed. This setup is schematically represented in Figure 2.10.

Afterwards, the compression wave reaches the free end of the transmission bar, reflecting itself as a tension wave. When this wave reaches the specimen, the collar can't support the tensile load, which means that it will transmit the pulse to the specimen. In this interface, the incident wave is partially reflected back towards the transmission bar, and is partially transmitted to the specimen and, afterwards, to the input bar.

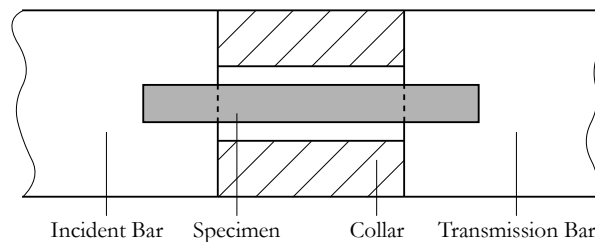


Figure 2.10: Schematic SHPB Tension setup designed by Nicholas [3, 14].

This design must use a collar with a large mechanical impedance, to avoid the plastic deformation of the specimen when the compression wave passes through both the specimen and the collar. To prevent this, the collar is made of the same material as the Bars (ANSI 4130 Steel Alloy) and has a ratio of cross-section of collar and pressure bar of  $\frac{3}{4}$ , while the ratio of cross-section of collar and specimen is of  $\frac{12}{1}$ . One should also note that this setup is not ideal for DIC analysis [3, 14].

It should be noted that the three bars do not have the same length. The striker bar is half the length of the transmission bar, which is the same as the SHPB Compression setup. However, unlike the traditional Kolsky Bar Compression setup, the incident bar is twice as long as the transmission bar. In fact, when the initial compression wave reaches the interface between the incident bar and the specimen/collar, a undesired reflected wave is generated. This first pressure bar is very long in order to avoid the superposition of any tensile wave with this "noise" compression wave [14].

A common direct loading system for Tensile SHPB systems is to have a tubular striker, actuated by a gas gun, so that it moves towards the free end of the incident bar,



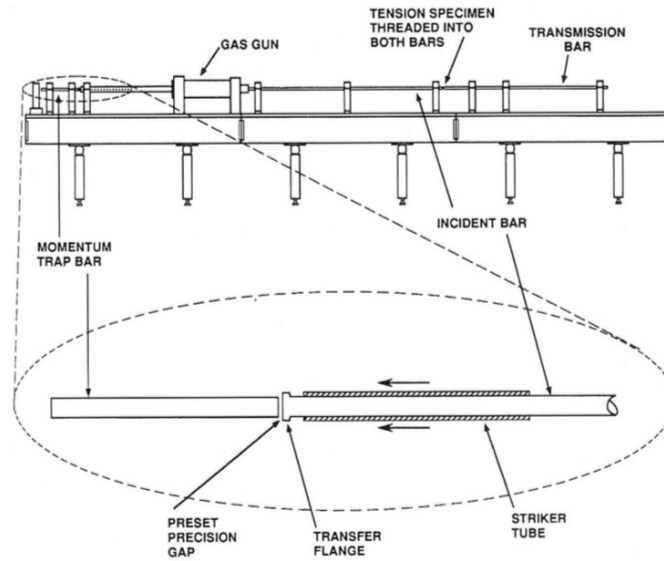


Figure 2.11: Direct Loading SHPB Tension setup with Tubular Striker [3, 15].

as shown in Figure 2.11. At this extremity, there is a transfer flange (also known as impact flange), and when the striker tube hits the transfer flange, a tensile stress wave is generated.

Next to the impact flange is the momentum trap bar that is separated by a preset precision gap. This gap is set such that the contact between the momentum trap bar and the input bar occurs once the entire tensile pulse is transferred from the tubular striker to the incident bar. The incident wave reaches the specimen, where one part is transmitted to the specimen and the transmitted bar, and the other part is reflected back as a compression wave. This compression wave is transmitted to the momentum trap bar and is reflected from its free end as a tensile wave. Since the interface between the incident bar and the momentum trap cannot support tensile pulses, the momentum trap bar stores the resulting reflected wave, forcing it to move forward the input bar [3, 11, 15].

This gap must be precisely adjusted. If the gap is too small, it will be closed during the loading of the tension pulse by the striker tube. Conversely, if the gap is too large, the reflected compressive wave will not be transmitted to the momentum trap bar. Either way, this may affect the stress wave or move the momentum trap bar into an undesirable position, or both, which may consequently invalidate the test results.

The free end of the transmission bar also has a transfer flange and a tubular momentum trap, just like the one present in the incident bar. In this case, the tension wave transmitted to the output bar reaches the transfer flange and reflects as a compression pulse to the tubular momentum trap. This element must be in physical contact with the transfer flange and must have the same impedance as the output bar, in order to trans-

mit the reflected compressive pulse to the momentum trap. When this wave reaches the extremity of the momentum trap, it reflects once again as a tensile pulse and remains trapped in the tube, which begins to move away from the flange. This phenomenon is similar to the one in the incident bar and its momentum trap [15].

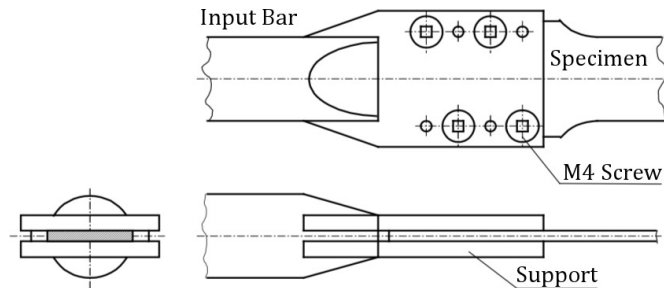


Figure 2.12: Specimen support for Direct Loading Kolsky Machine by Ferreira [11].

Ferreira applied the same architecture to the SHPB tension and compression machine located in the Laboratory of Optics and Experimental Mechanics (LOME) of FEUP. However, unlike the architecture presented by Nemat-Nasser et Al., the dissipation of the kinetic and deformation energy is performed by means of a Nylon momentum trap next to the free end of the output bar. The test machine also has specimen support welded on the bars, like the one shown in Figure 2.12. In this design, the specimen is fixed to the support thanks to M4 screws as well as to a high roughness of support's inner surface, which avoids any slipping motion between the specimen and the bars [11].

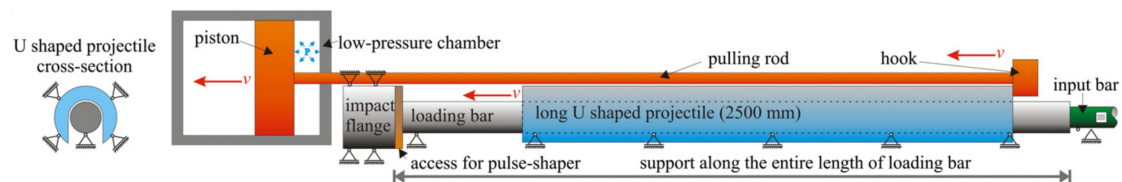


Figure 2.13: SHPB Tension setup designed by Gerlach, Kettenbeil and Petrinic [16].

This design, while being extensively used with minor differences, has some limitations. By using a tubular striker bar, the portion of the input bar where the tubular bar moves, must not be supported in order to allow the motion of the striking element. Projectile lengths must be short (of up to 500 mm), which means that the stress pulse has a limited duration of approximately 0.2 ms. One must also take into account that there is bending of the input bar where it is unsupported, causing undesirable contact between this and the striker tube. This means that the resulting stress wave will be affected by both problems, making the loading pulse of low quality. The contact between elements may also cause unwanted motion of the entire pressure bar setup, including the specimen, putting it out of focus of any image or optical measuring devices.

These problems have motivated Gerlach, Kettenbeil and Petrinic to present an alternative SHPB Tension machine architecture, that is presented in Figure 2.13. With

this new design, the authors propose a machine that generates a clean and almost rectangular stress pulse, with a duration of at least one millisecond and free of any stress oscillations or disturbances. In order to accomplish this, the striker bar consists of a U-shaped projectile. In the lower end of the loading bar, which is an extension of the incident bar, there is no physical obstruction caused by the striker tube, since it is U-shaped, allowing the loading bar to be supported. The non-circular striker bar surrounds the loading bar, while not being in contact with each other. It should be noted that the striker projectile is also supported through bronze railings.

The striker element is actuated due to an hook connected to the rod of a pneumatic cylinder, moving the non-circular projectile towards the impact flange. The piston of the actuator is accelerated with low pressures, thanks to its large cross section. With this design, the projectile is also accelerated, until the piston decelerates, causing the hook to loose contact with the striker. Afterwards, this striker continues moving until it hits the flange, where the stress wave is generated [16].

### 2.3 SHPB Design Requirements and Recommendations

The design of any machine must always follow a set of guidelines in order to accomplish its purpose. On conventional mechanical projects, one starts with former experience and tools. If these are not available, one must find design requirements on specialized bibliography. In this section, some mechanical design requirements that were found in the literature are presented.

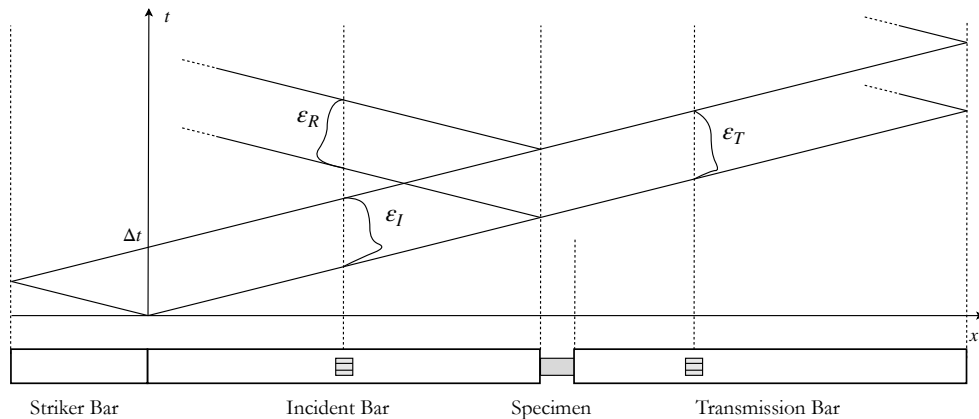


Figure 2.14: Lagrange Diagram (or  $x - t$  Diagram) for Compression Split Hopkinson Bar [3, 11]

The pressure bars used in the SHPB must sustain the stress pulses generated without any plastic deformation, since these elements must only conduct the stress pulses. In other words, these bars must be linearly elastic, otherwise, the measured deformation waves would have significant fluctuations, invalidating the test. As such, the bars must be made of a material with linear elastic behaviour and high yield strength.

The bars must also be perfectly aligned, to allow the transmission of the pulse without disturbances. Any significant misalignment may cause unwanted reflection of waves, producing a low quality pulse. Therefore, the bars must be designed with tight geometric tolerances. To guarantee the alignment of the bars when the machine is assembled, a Laser aligning system may be used. Support of the bars must have low friction, in order to maintain the pulse loading without significant losses [3].

Normally, the incident bar should have a length of more than twice the length of the striker bar, in order to maintain the stress wave trapped only in the incident bar, without having any reflection or transmission into another medium. This can be easily seen on a Lagrange diagram (or  $x - t$  diagram) for the Split Hopkinson Bar setup, as depicted in Figure 2.14. In this case, when the striker bar hits the incident bar, a stress wave with a duration,  $\Delta t$ , is generated such as

$$\Delta t = \frac{2 L_{SB}}{c_B} \quad (2.43)$$

where  $L_{SB}$  is the length of the striker bar. This can be seen in Figure 2.14, where two compression waves are generated on impact: one on the incident bar, and one on the striker bar. When this second pulse reaches the free end of the striker, it reflects as a tensile pulse, canceling the initial compression wave. Then, when the "stress free" wave reaches the interface between the two bars, the compression pulse on both bars ends. Thus, the compression pulse has a length of twice the striker bar.

This last characteristic depends on the design setup of the test machine, but, generally speaking, most Kolsky Bar machines have this requirement. If this is not verified, then there will be an overlapping between the incident and the reflected waves, making the setup inadequate for material testing [3, 4, 11].

The strain gauge located in the incident bar must be placed at half length of the incident bar to avoid the reading of overlapped incident and reflected waves. Other transducers should be placed near the specimen, but at the proximity of any interface, there is non uniformity of the wave. Therefore, any other strain gauges should be placed with a distance of at least 10 times the bar's diameter [11].

It should also be noted that the impedance of the striker bar should be identical to the one of the input bar. Mismatched impedances between these two bars may result in changes both in the amplitude and the profile of the generated pulse. If the striker bar impedance is higher, then the unloading of the pulse into the incident bar will occur in a progressive way, with decreasing amplitudes, as shown in Figure 2.15. Because of this, normally, the bars have the same diameter and are of the same material, but this is not mandatory [3, 17].

Usually, these test machines have a small bar diameter, between  $\varnothing_B = 10$  mm and  $\varnothing_B = 25$  mm, although there are machines with larger or smaller bar diameters. When the bars of the pressure setup are of considerable dimensions, the strain-rate is restricted, due to the large specimen size and to the high amount of energy required by

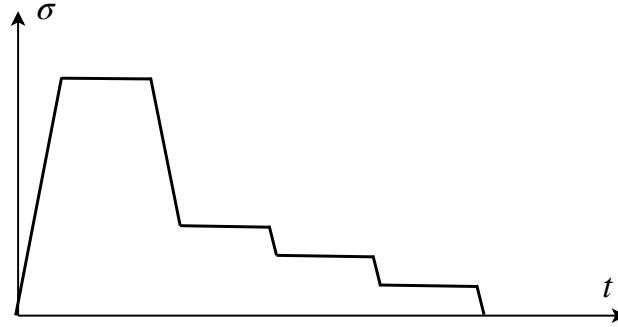


Figure 2.15: Incident stress pulse due to mismatched impedance between the striker and the input bars [3]

the gas gun to launch the striker bar. Large diameter pressure bars also make a more severe radial stress wave dispersion.

On the other hand, when the bars have small diameters, the strain rate range obtained can increase to values of  $\dot{\epsilon}_s = 10^5 \text{ s}^{-1}$ , because, if the specimen dimensions are small, the resultant accelerations are high. During this acceleration period, the specimen's stress-strain state changes drastically, since it quickly changes from rest to high strain rate. Thus, before reaching the desired strain rate, the specimen may have accumulated a significant amount of strain, which, in some cases, may invalidate the test [3].

Another requirement is that the ratio of impedance between the bars and the specimen,  $\alpha_Z = \frac{Z_B}{Z_s}$ , should exhibit values with an order of magnitude of 10, where the variables  $Z_B$  and  $Z_s$  are defined by equation (2.10). This means that the specimen's dynamic behaviour under a pulse load should not be significantly different from one of the bars. This is usually the case for testing metallic specimen and may also be applied to other materials, but this isn't mandatory [11].

One should take into consideration that the bars stiffness should be approximately equal to that of the specimen, since the load wave should have the same behaviour both when it is passing through the bars, and when it is passing through the specimen. Since the pulse cannot be measured on the specimen, one must measure the pulses that travel along the bars.



## Chapter 3

# SHPB Machine Dynamics

In the previous chapters, the requirements for the design of the Kolsky Bar machine were presented, as well as a physical model of the Pressure Bars setup. Based on these, this chapter discusses what these requirements reflect in the behaviour of the test machine.

The first section presents the models used to relate the requirements and the physical behaviour of a SHPB setup in order to estimate values for the design of the various functional groups of the machine. These models are then numerically calculated and the results are presented in the next section. Finally, the last section outlines the conclusions drawn from the results and presents geometric dimensions for the bar setup, as well as some reference values for the actuation system that will launch the striking element.

### 3.1 Machine Characterization Model

In order to design the Kolsky Bar test machine, it is necessary to study its design requirements. In doing so, a rough definition of dimensional and physical quantities is determined. It is important to mention that the mathematical models are independent of which type of test (tensile or compression test) is being carried out.

A study of the wave propagation dynamics is conducted, based on the mathematical models presented in section 2.1, thus determining the required velocity and length of the striker bar in order to fracture a bonded joint. Additionally, based on the design recommendations presented in section 2.3, the wave impedance and stiffness between the bars and the specimen are compared.

#### 3.1.1 Considerations

When modeling the dynamics of the bars and specimen, several simplifications and considerations are made. Without these assumptions, the application of the mod-

els would be extremely difficult or impossible, and the design requisite could only be achieved using Finite Element Method numerical simulations. It should be mentioned that, although the study of the requirements could be made using Finite Element Analysis software, this approach was not made, for it would take too long.

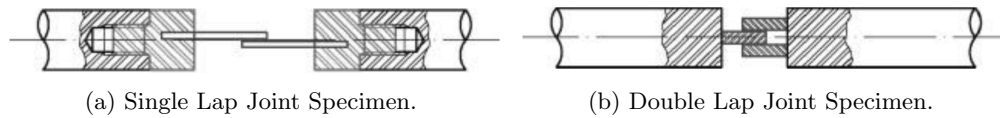


Figure 3.1: Most used Joint Specimen for SHPB Machines [18].

When modeling Bonded Joint Specimens (BJS) for mode II loading, it was initially considered that the specimen had a cylindrical geometry based on the single lap joint, like the one shown in Figure 3.1a. However, this geometry was discarded. Indeed, with the opinion of ADFEUP, that geometry would not allow for rigorous testing of a mode II joint, since the bonding area is small. Furthermore, this specimen design is susceptible to bending effects if the substracts and the loads are not perfectly aligned. In order to solve this problem, a specimen loading with precisely aligned pins using a pin-ball arrangement, like the one presented in Figure 3.2, should be implemented in case a single lap joint specimen is used [18]. Nevertheless, this setup is not recommended, since it causes the existence of several interfaces between elements, that may cause various unwanted pulse reflections. Given these problems, it is more advised to use a specimen with double lap joint, like the one represented in Figure 3.1b, which is not susceptible to these problems.

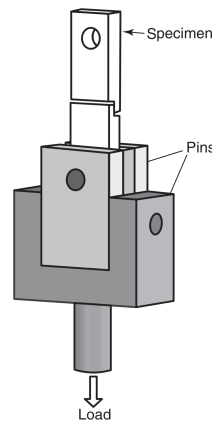


Figure 3.2: Pin loading arrangement [18].

When studying the wave impedance and stiffness relation between the bars and the specimen, only BJS with Steel and Aluminium substracts are considered. Specimens with composite substracts are not studied here since they would add more complexity. If one were to study specimen with composite substracts, it would be necessary to simulate the substract material with fibers aligned in one direction, several specific directions, or



random orientations. This would change drastically the elasticity modulus.

Composite materials can be characterized as having a two stage behaviour, like the one represented in Figure 3.3, where, usually, the fiber is a brittle component and the matrix, being polymeric in nature, is ductile. On stage I, both materials deform elastically, which means that the composite's behaviour can be described by the Hooke Law. On stage II, the fibers remain in the elastic domain, but the matrix starts to deform plastically, which means that the composite has a second elasticity modulus that describes its stress-strain performance during stage II [19]. This change of behaviour is difficult to implement in the mathematical models.

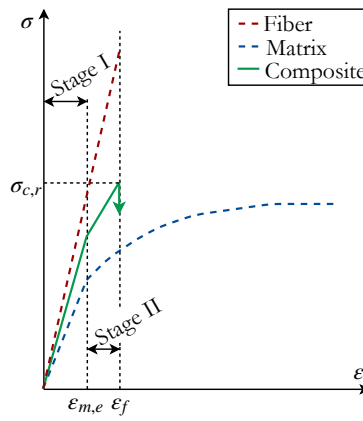


Figure 3.3: Stress-Strain curve for composite materials [19].

It should be noted that the simulations are performed only for modes I and II BJS. Mixed-Mode is not considered, because the properties of adhesives can vary according to the orientation of the adhesive plane as well as on the type of adhesive. For that particular reason, several laws are used for describing the behaviour of an adhesive. However, these laws can vary significantly from material to material and, for that reason, can lead to an high degree of indetermination.

The following studies consider that the adhesive tested is either rigid and with a high Young modulus,  $E_{Ad} = 4$  GPa, or flexible/soft and with a low Young modulus,  $E_{Ad} = 1$  MPa. Usually, adhesives have a mass density,  $\rho_{Ad}$ , between  $1000 \text{ kg m}^{-3}$  and  $1500 \text{ kg m}^{-3}$ , so a reference value of  $\rho_{Ad} = 1250 \text{ kg m}^{-3}$  is considered. Additionally, bars of Stainless Steel, Aluminium and Titanium Alloy are considered. The mechanical properties for bars are presented in Table 3.1. The properties of Steel and Aluminium substract are presented in Table 3.2.

Table 3.1: Material properties for bars [7, 19].

Material	$E$ [GPa]	$\rho$ [ $\text{kg m}^{-3}$ ]
Stainless Steel	220	7700
Aluminium Alloy	72.4	2700
Titanium Alloy	109	4500

Table 3.2: Material properties for substracts [7, 19].

Material	$E$ [GPa]	$\rho$ [kg m <sup>-3</sup> ]
Low Carbon Steel	210	7870
Aluminium Alloy	72.4	2700

### 3.1.2 Actuation Requirements

In subsection 2.1.3, a mathematical model of the stress-strain behaviour of the specimen was presented. The formulation is based on the wave phenomena to determine the average stress,  $\sigma_s$ , and strain,  $\varepsilon_s$ , that are applied on the specimen. This model is useful since it can be reformulated to determine the striker bar velocity,  $v_{SB}$ , in accordance with the desired specimen's stress,  $\sigma_s$ , and the desired specimen's strain rate  $\dot{\varepsilon}_s$ . Also based on these calculations, and on the energy study of the specimen's behaviour of section 2.1.4, the striker bar's length can be estimated.

#### Striker Bar Velocity

Rewriting equation (2.22), one can calculate the transmitted strain,  $\varepsilon_t$ , so that

$$\varepsilon_t = \frac{\sigma_t}{E_B} = \frac{A_s \sigma_s}{A_B E_B} \quad (3.1)$$

The reflected strain,  $\varepsilon_r$ , can be obtained from equation (2.24), which yields

$$\varepsilon_r = \frac{L_s \dot{\varepsilon}_s}{2 c_B} \quad (3.2)$$

where  $c_B$  is the input and output bar's wave propagation velocity. Considering that there is no dissipation of the pulse's energy by the plastic deformation of the specimen, one can determine that the sum of the reflected and transmitted pulse's energy equals that of the incident wave. As such, summing the transmitted strain,  $\varepsilon_t$ , and the reflected strain,  $\varepsilon_r$ , in modulus, one yields the incident strain,  $\varepsilon_i$ , in modulus

$$|\varepsilon_i| = |\varepsilon_t| + |\varepsilon_r| \quad (3.3)$$

With the calculated incident strain,  $\varepsilon_i$ , one can determine the velocity of the striker bar,  $v_{SB}$ , given by

$$v_{SB} = 2 c |\varepsilon_i| \quad (3.4)$$

This equation derives from the momentum equilibrium between the striker bar and the input bar, which states that

$$m_{SB} v_{SB} = m_p v_p \quad (3.5)$$

where:

- $m_{SB}$  and  $m_p$  are the mass of the striker bar and the mass of the incident bar that contains the entire load wave, respectively;
- $v_p$  is the velocity of a particle when the pulse passes through it, and can be defined by equation (2.9).

Considering that  $m = \rho Al$ , the mass density and cross-section area of the striker and incident bars are identical, and that the length of the pulse is the double of the striker bar's length,  $l_p = 2 l_{SB}$ , then one can determine from equation (3.4) that

$$v_p = \frac{v_{SB}}{2} \quad (3.6)$$

Thus, replacing the following relation in equation (2.9) yields equation (3.4) [4, 11].

### Striker Bar Length

Given that an estimation of the reflected and the transmitted strain were calculated using the specimen's stress behaviour model, it is possible to determine an initial value of the striker bar's length using values of the deformation energy,  $U_s$ . Therefore, rearranging equation (2.42) yields the time duration of the stress wave,  $\Delta t$ , namely

$$|\Delta t| = \frac{U_s}{|2 A_B c E_B \varepsilon_r \varepsilon_t|} \quad (3.7)$$

Knowing that the specimen deformation energy,  $U_s$ , can be defined by the critical energy release rate,  $G_C$ , which is function of the critical stress intensity factor,  $K_C$ , and the adhesive Young modulus for plane stress,  $\bar{E}$ , and is expressed by

$$G_C = \frac{K_C}{\bar{E}} \quad (3.8)$$

The critical energy release rate of an adhesive is the maximum energy release rate that a given material can sustain until crack propagation occurs. The critical stress intensity factor,  $K_C$ , is defined by

$$K_C = Y \sigma_{Ad} \sqrt{\pi a} \quad (3.9)$$

where  $Y$  represents a non-dimensional parameter that depends on the geometry of the specimen, load and stress distribution,  $a$  is the crack length, and  $\sigma_{Ad}$  is the stress applied to the perpendicular direction of the crack. The Young modulus of the adhesive for plane stress,  $\bar{E}$ , is defined by

$$\bar{E} = \frac{E}{1 - \nu^2} \quad (3.10)$$

where  $E$  and  $\nu$  are the material's elasticity modulus and the Poisson coefficient, respectively [20].

As such, the Specimen Deformation Energy,  $U_s$ , is estimated by

$$U_s = G_C A \quad (3.11)$$

where  $G_C$  is given by equation (3.8), and  $A$  is the area where the load is applied. This value can vary not only with the material being tested, but also with the fracture mode. A value of  $G_C = 10 \text{ N mm}^{-1}$  can be used for the toughest adhesives being tested.

Knowing the definition of the time duration of a stress pulse,  $\Delta t$ , defined in equation (2.43) and considering the specimen deformation energy,  $U_s$ , previously defined, one can rewrite equation (3.7) to obtain the length of the striker bar,  $L_{SB}$ , yielding

$$L_{SB} = \frac{G_C A_s}{4 A_B E_B \varepsilon_r \varepsilon_t} \quad (3.12)$$

One should note that the reflected and transmitted strains used,  $\varepsilon_r$  and  $\varepsilon_t$ , respectively, are those that are determined when calculating the striker bar velocity,  $V_{SB}$ , which is based on the specimen's stress-strain behaviour that, in turn, is described in subsection 2.1.3. Meanwhile, the length of the striker bar,  $L_{SB}$ , is estimated by a mathematical model that defines the fracture energy of a specimen, as presented in section 2.1.4. However, the aforementioned models were defined with opposing assumptions:

- In the specimen's stress-strain behaviour model, it was considered that the specimen did not present any deformation, as can be seen in equation (2.23);
- In the specimen's plastic deformation energy model, it was assumed that the specimen would only suffer plastic deformation.

These assumptions are contradictory and simplistic, but the truth is that the obtained values for the reflected and transmitted strains are realistic, which means that these models are not numerically incompatible.

As such, rewriting equation (3.12) with the transmitted and reflected strains,  $\varepsilon_t$  and  $\varepsilon_r$ , presented in equations (3.1) and (3.2) respectively, yields

$$L_{SB} = \frac{G_C c_B}{2 \sigma_s L_s \dot{\varepsilon}_s} \quad (3.13)$$

meaning that the striker bar length depends only on the properties of the specimen.

### 3.1.3 Wave Impedance & Stiffness Analysis

As previously mentioned in section 2.3, the impedances and stiffnesses of both the bars and the specimen must be studied.

#### Study of Wave Impedance

When testing materials on a Kolsky Bar machine, the propagation of the wave through different media (bars and specimen) must not be hindered. Then, according to the design recommendations presented in 2.3, the ratio between the bar's impedance,

$Z_B$ , and the specimen's impedance,  $Z_s$ , should be of order of magnitude 10. So, the wave impedance ratio,  $\alpha_Z$ , is defined as

$$\alpha_Z = \frac{Z_B}{Z_s} \quad (3.14)$$

where,  $Z_B$ , the bar's impedance, and,  $Z_s$ , the specimen's impedance, are given by equation (2.10). When calculating the bar's impedance, the bar's Young modulus,  $E_B$ , its cross section area,  $A_B$ , and its mass density,  $\rho_B$ , are considered.

When calculating the wave impedance of the specimen,  $Z_s$ , two cases are considered:

- The Bulk Specimen (BS), where the adhesive mass density,  $\rho_{Ad}$ , the material's Young modulus,  $E_{Ad}$ , and the specimens cross-section area,  $A_s$ , are used;
- The Bonded Joint Specimen, where the mechanical properties of the substract are assumed, and the cross section area used for calculations is that of the entire specimen. This assumption is valid since the specimen consists mostly on the adherend, and a small fraction of the wave will pass through the adhesive.

### Study of Stiffness

The relationship between the bar's stiffness and the specimen's stiffness is made with the stiffness ratio,  $\alpha_k$ , defined as

$$\alpha_k = \frac{k_B}{k_s} \quad (3.15)$$

where:

- $k_B$  is the stiffness of the bars

$$k_B = \frac{E_B A_B}{L_{\text{pulse}}} \quad (3.16)$$

with  $E_B$ ,  $A_B$  and  $L_p$  being the Young modulus, the cross-section area of the bars, and the length of the stress pulse, respectively;

- $k_s$  is the specimen's stiffness. Tests can be made either with BS of any adhesive, or with BJS, where the adhesive is tested in mode I (tensile test), mode II (shear test) or mixed-mode. This means that the specimen's stiffness can be calculated differently according with the type of specimen.

For the BS, its stiffness,  $k_{s,BS}$ , is defined as

$$k_{s,BS} = \frac{E_{Ad} A_s}{L_s} \quad (3.17)$$

where  $A_s$  and  $L_s$  are the cross-section area and the length of the specimen, respectively, and  $E_{Ad}$  is the young modulus of the adhesive being tested.

When testing a mode I BJS, the specimen has three components - two substracts and the adhesive - and the specimen's stiffness,  $k_{s,I}$ , can be defined as

$$\frac{1}{k_{s,I}} = \frac{1}{k_{Ad,I}} + \frac{2}{k_{Sub}} \quad (3.18)$$

where  $k_{Ad,I}$  and  $k_{Sub}$  are the adhesive in mode I and the substract stiffnesses, given by equation (3.17). It should be noted that, when calculating  $k_{Sub}$ , the Young modulus of the substract is considered.

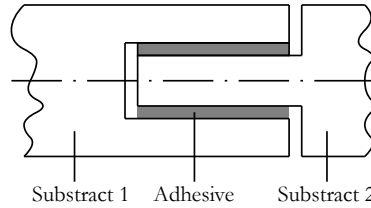


Figure 3.4: Schematic representation of a Mode II BJS.

In case of mode II BJS, the specimen's stiffness,  $k_{s,II}$ , is also defined as a series stiffness. However, since the adhesive will be under shear loading, and given that the substracts have different cross-section areas, the specimen's stiffness is

$$\frac{1}{k_{s,II}} = \frac{1}{k_{Sub1}} + \frac{1}{k_{Ad,II}} + \frac{1}{k_{Sub2}} \quad (3.19)$$

where  $k_{Sub1}$  and  $k_{Sub2}$  are the stiffness of the two substracts. These variables are defined the same way as in equation (3.17), but the cross-section area considered depends on the substract. The stiffness of the adhesive,  $k_{Ad,II}$ , is defined by

$$k_{Ad,II} = \frac{G_{Ag} A_{Ad}}{L_s} \quad (3.20)$$

where  $G_{Ad}$  is the shear modulus and  $A_{Ad}$  is the area of the adhesive where the shear solicitation is applied [21]. The shear modulus can be related to the Young's modulus

$$G = \frac{E}{2(1 + \nu)} \quad (3.21)$$

where  $\nu$  is the Poisson coefficient and is approximately 0.35 for all adhesives [22].

## 3.2 Results

A program in MATLAB<sup>®</sup> was developed to study the behaviour of the SHPB, with Steel, Aluminium Alloy and Titanium Alloy bars, with either soft and rigid adhesives, as stated in subsection 3.1.1.

The obtained results for the striker bar velocity are presented in subsection 3.2.1. Afterwards, the results for striker bar length are discussed in subsection 3.2.2. Finally,

the Impedance and Stiffness ratios are presented and commented in subsection 3.2.3. Additional figures are shown in Appendix A.

### 3.2.1 Striker Bar Velocity

The striker bar velocity,  $v_{SB}$ , is a function of the desired specimen's strain-rate,  $\dot{\epsilon}_s$ , the bar's diameter,  $\varnothing_B$ , the bar's material (which means that it is function of the elasticity modulus,  $E_B$ , and its mass density,  $\rho_B$ ), the length of the specimen,  $L_s$ , and the average specimen's stress,  $\sigma_s$ .

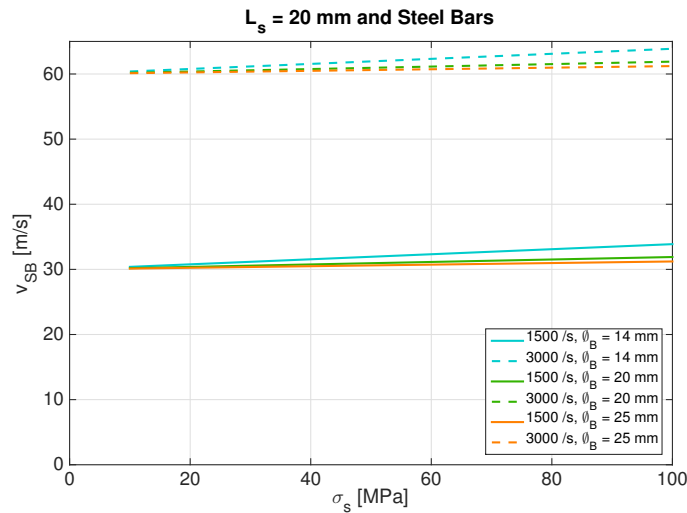


Figure 3.5: Striker bar velocity required for Stainless Steel bars and specimen of length  $L_s = 20$  mm.

Given the number of variables that influence  $v_{SB}$ , its analysis is complex, and it was decided to distinguish different combinations of specimen's length and bar materials. The model does not take into account the type of specimen used, since it does not consider the specimen's material properties.

Figures 3.5, 3.6 and 3.7 show the relation between the striker bar velocity and the specimen stress for a specimen of 20 mm length and Stainless Steel, Aluminium and Titanium Alloy bars, respectively. Figure 3.8 shows the same relation for specimen of 10 mm length and Stainless Steel bars.

It is observed from these figures that the slope of the striker bar velocity,  $v_{SB}$ , tends to lower with higher bar diameter and with higher bar's elasticity modulus,  $E_B$ . This is physically accurate. For the same specimen stress,  $\sigma_s$ , to be attained with a bar of bigger cross-section area, a higher momentum of the striker bar is required and, consequently, a higher striker bar velocity is required.

Also, the higher the bar's Young modulus,  $E_B$ , is, the lower the bar's transmitted strain,  $\epsilon_t$ , will be, and consequently, the lower the striker bar velocity,  $V_{SB}$ , will be. This

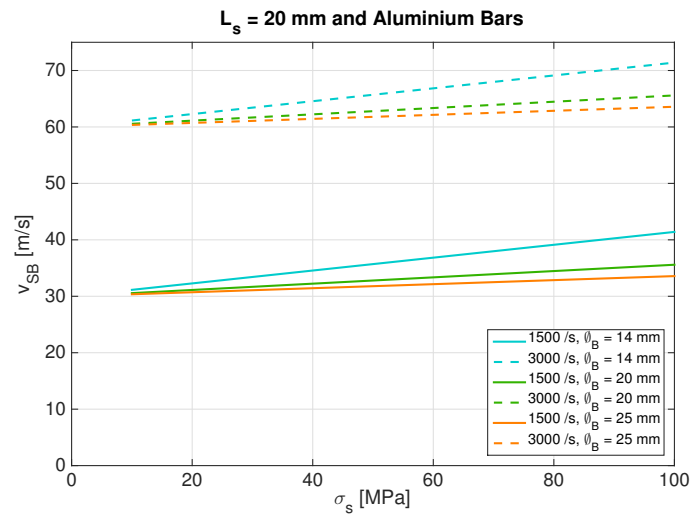


Figure 3.6: Striker bar velocity required for Aluminium Alloy bars and specimen of length  $L_s = 20$  mm.

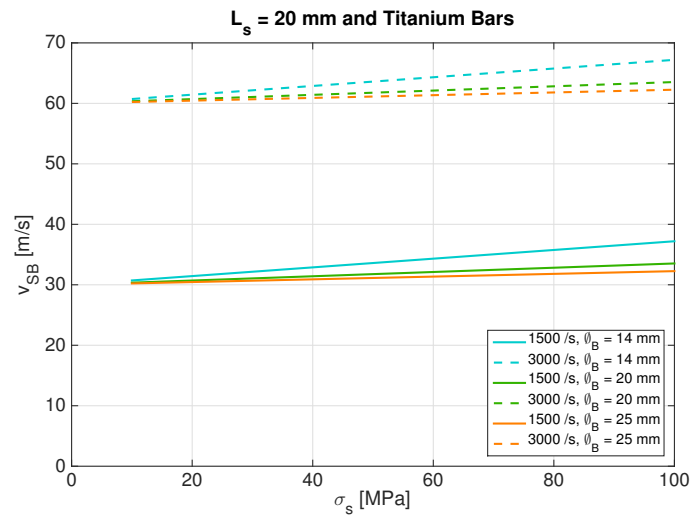


Figure 3.7: Striker bar velocity required for Titanium Alloy bars and specimen of length  $L_s = 20$  mm.

is observed when comparing Figures 3.5, 3.6 and 3.7. For a given bar geometry and specimen's strain-rate,  $\dot{\epsilon}_s$ , Aluminium/Steel bars require a higher/lower striker bar velocity, when compared with Titanium bars, in order to attain the same average specimen stress. The scenario where the Stainless Steel bars are used, is almost equivalent to a Kolsky Bar setup where the bars have an infinite rigidity, so that a small change in  $v_{SB}$  results in an extremely high specimen stress.

For a specimen of given length,  $L_s$ , more energy is required to strain it at a



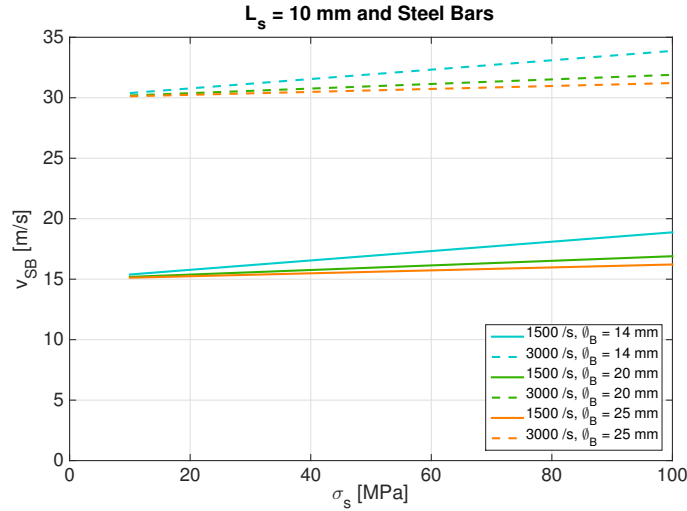


Figure 3.8: Striker bar velocity required for Stainless Steel bars and specimen of length  $L_s = 10$  mm.

higher strain-rate,  $\dot{\epsilon}_s$ , and thus, a higher striker velocity,  $v_{SB}$ , is required. While this is correct, the velocities required for BJS seem extremely high, even if not considering effects such as the added rigidity caused by the adhesive-substrate adherence on high roughness surfaces. As such, the same model was applied under the assumption that the specimen is only the adhesive layer.

Figures 3.9 and 3.10 show the relation between  $v_{SB}$  and  $\sigma_s$  for Stainless Steel bars and specimen of length of 0,2 mm and 2 mm, respectively.

These cases describe with more accuracy the relationship between the striker bar velocity,  $v_{SB}$ , the specimen stress,  $\sigma_s$ , and the specimen's strain-rate,  $\dot{\epsilon}_s$ . Given that the adhesive should have a more flexible behaviour and also has a lower tensile strength, when compared with the substrate, the required striker bar velocity should be lower than what was calculated in Figures 3.5 to 3.8. This model was tested considering that the "specimen" has a length that can vary between  $0,1 \leq L_s \leq 2$  mm. It should also be noted that bulk specimen used for SHPB testing tend to have small diameters and lengths, and thus, these figures are also applicable to bulk specimen.

As observed in the cases where specimen have lengths of 10 and 20 mm, the specimen's strain-rate,  $\dot{\epsilon}_s$ , obtained was of  $3000 \text{ s}^{-1}$ . Indeed, the striker bar velocities mentioned were extremely high corresponding approximately to higher values than the ones observed in results present in the literature review. Conversely, since the length of adhesive layer (or the length of a bulk specimen) is much smaller, it is possible to reach higher strain-rates with a lower striker bar velocity.

It should be noted that all figures result from using the aforementioned model, where the striker bar velocity,  $v_{SB}$ , is a function of both the transmitted strain,  $\epsilon_t$ ,

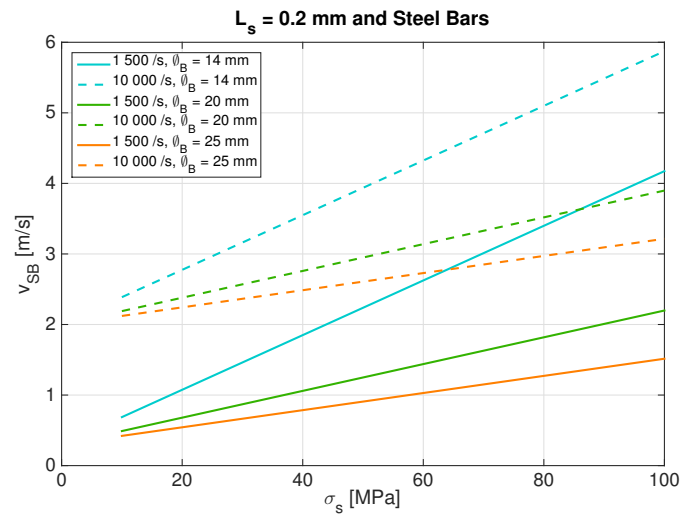


Figure 3.9: Striker bar velocity required for Stainless Steel bars and specimen of length  $L_s = 0.2$  mm.

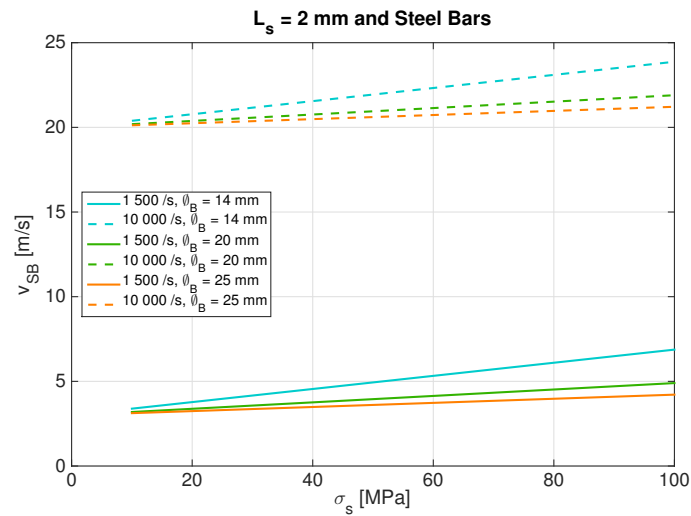


Figure 3.10: Striker bar velocity required for Stainless Steel bars and specimen of length  $L_s = 2$  mm.

and the reflected strain,  $\varepsilon_r$ . For each combination of bar material and geometry, the transmitted strain,  $\varepsilon_t$ , varies with the specimen's stress,  $\sigma_s$ , while the reflected strain,  $\varepsilon_r$ , remains constant. According with this model, for a given strain-rate and a given specimen length, there is a non null striker bar velocity in order to attain a null specimen stress. This does not reflect the physical reality, since a high velocity impact between the striker bar and the incident bar will always cause a stress wave. As such, all striker bar velocity values,  $v_{SB}$ , for specimen stresses below  $\sigma_s = 10$  MPa were considered as

non-valid results.

These results were obtained having in mind how the specimen would behave. In other words, specific values of  $\sigma_s$  and  $\dot{\epsilon}_s$  were imposed beforehand to determine the value of  $v_{SB}$  for a given bar geometry. This strategy was adopted to have an idea of the required striker bar velocity range. However, given a specimen of fixed dimensions and materials, a specified striker bar velocity,  $v_{SB}$ , will yield a specified specimen stress,  $\sigma_s$ , and strain-rate,  $\dot{\epsilon}_s$ .

### 3.2.2 Striker Bar Length

In this subsection, the striker bar length is calculated as a function of the critical energy release rate of an adhesive,  $G_C$ , the bar's material (which, in turn, means that it is a function of both its mass density,  $\rho_B$ , and Young modulus,  $E_B$ ), the specimen's length,  $L_s$ , stress,  $\sigma_s$ , and strain-rate,  $\dot{\epsilon}_s$ , as described by equation (3.13).

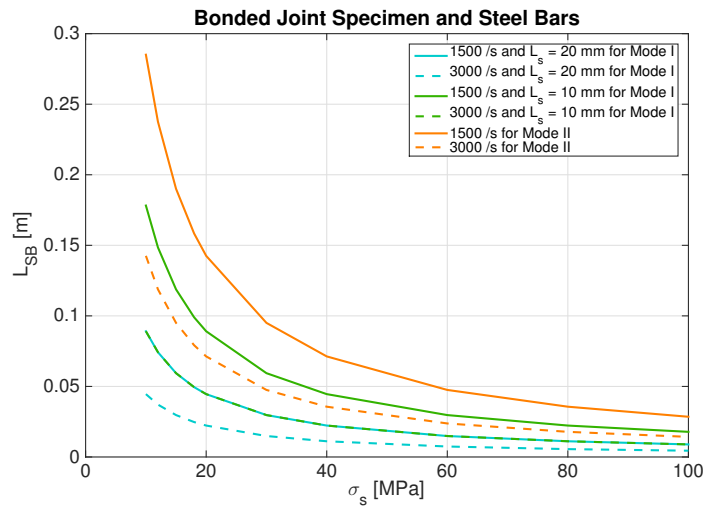


Figure 3.11: Striker bar length required for Stainless Steel bars and BJS.

Given that both bulk and bonded joint specimen are used to study the striker bar length, two types of figures are presented. Figures 3.11, 3.12 and 3.13 show the relation between striker bar length and specimen stress both for mode I and mode II BJS with Stainless Steel, Aluminium and Titanium Alloy bars, respectively. Figures 3.14, 3.15 and 3.16 shows the same relation for bulk specimen of length,  $L_s$ , of 1 mm, 2 mm, and 5 mm, respectively.

From Figures 3.11, 3.12 and 3.13, it is inferred that, for mode I testing, the length of striker bar is dependent of the specimen's strain-rate,  $\dot{\epsilon}_s$ , and the length of the specimen,  $L_s$ , as can be seen in equation (3.13). If the specimen's strain-rate increases, then the striker bar length,  $L_{SB}$ , decreases, if the same specimen deformation energy,  $U_s$ , is considered. The same conclusion can be made when analyzing the variable  $L_s$ .

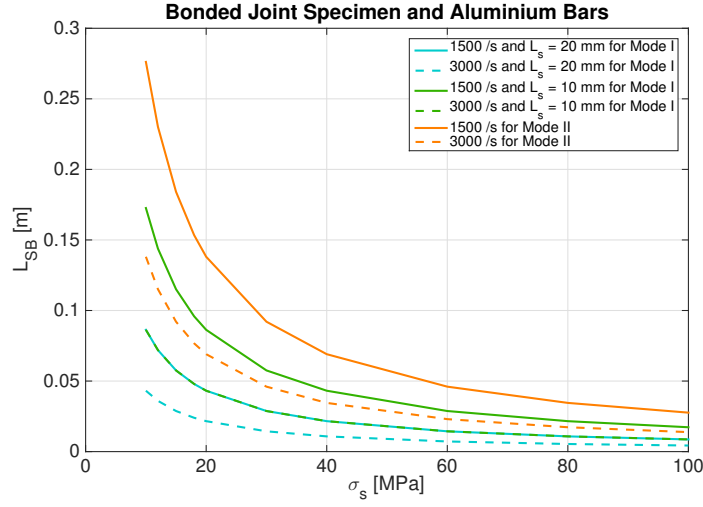


Figure 3.12: Striker bar length required for Aluminium Alloy bars and BJS.

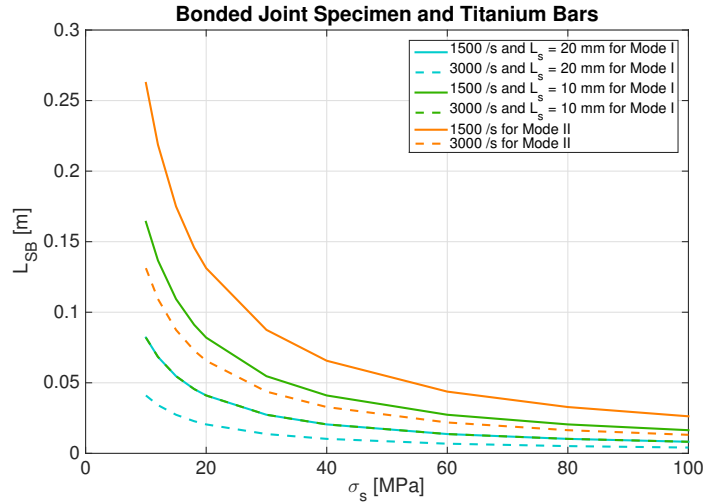


Figure 3.13: Striker bar length required for Titanium Alloy bars and BJS.

It is also deduced that, for mode II BJS,  $L_{SB}$  is not dependent on the length of the specimen,  $L_s$ . This effect occurs because the calculation of specimen deformation energy,  $U_s$  is made using an average area of contact between the substrates and the adhesive,  $A_{s,II}$ , defined as

$$A_{s,II} = L_s \pi \varnothing_{Ad} \quad (3.22)$$

where  $\varnothing_{Ad}$  is the diameter of the cross-section perimeter where there is adhesive. This assumption was considered in the calculations because, in mode II specimen, the adhesive is under shear loading. This premise does not invalidate the use of equation (3.1) to

calculate the transmitted strain, since this equation is deduced from the force balance on the interface between the specimen (or, for mode II specimen, the substract) and the transmission bar. As such, the striker bar length can be defined from equation (3.7) as

$$L_{SB} = \frac{G_C \pi \varnothing Ad}{2 \dot{\epsilon}_s A_s E_B \sigma_s} \quad (3.23)$$

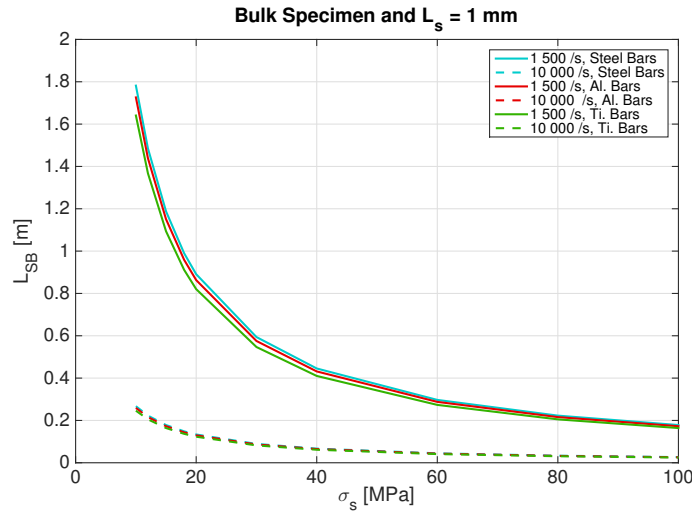


Figure 3.14: Striker bar length required for BS of length  $L_s = 1$  mm.

Figures 3.14, 3.15 and 3.16 presents the calculated striker bar length,  $L_{SB}$ , for BS, using equation (3.13). The previous conclusions for mode I specimen can be repeated when analyzing BS, mainly that a smaller striker bar is required when a longer specimen,  $L_s$ , or a higher strain-rate,  $\dot{\epsilon}_s$ , is required.

It should be noted that the striker bar length needed to fracture a bulk specimen is quite high when a low stress pulse is generated. This is logical, because, in order to transmit the same quantity of energy to the specimen, with a low stress wave generated, a longer pulse needs to be generated, which means that a longer striker bar needs to be used. While this is common to all cases, the values obtained for low stress wave pulses and bulk specimen of length 1 mm and 2 mm are quite high. No Kolsky Bar machines have used a striker bar of length superior to 1 meter, and machines with long striker projectile tend to generate quite long stress waves. Normal SHPB setups tend to have a striker bar of 0.5 meters or lower in length.

A small variation of the striker bar length is observed, when comparing SHPB setups using Stainless Steel, Titanium and Aluminium Alloy bars due to their properties. as can be seen in Figure 3.11 to 3.16. However, these differences tend to be quite small, and, they can be ignored for the design of the machine.

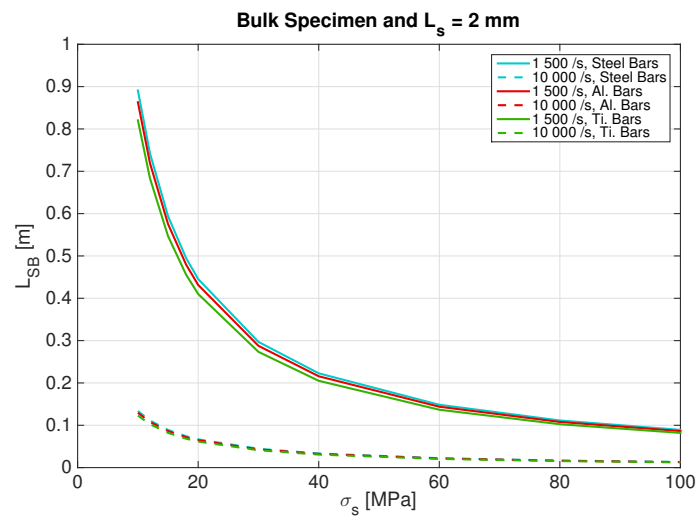


Figure 3.15: Striker bar length required for BS of length  $L_s = 2$  mm.

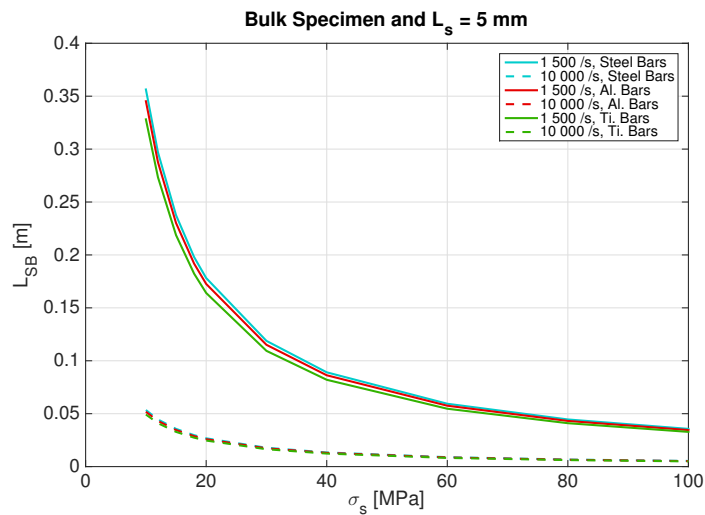


Figure 3.16: Striker bar length required for BS of length  $L_s = 5$  mm.

### 3.2.3 Impedance & Stiffness Ratios

In this subsection, the influence of the impedance and stiffness ratios,  $\alpha_Z$  and  $\alpha_k$ , is considered. These ratios are calculated for either rigid or flexible/soft adhesives with Stainless Steel, Aluminium and Titanium Alloy bars. The properties of both the bars and the adhesives are listed in section 3.1.1. The pulse length,  $L_p$ , considered as a reference value for these calculations, is of 500 mm, given the results obtained in the previous subsection. Therefore, it is considered that the striker bar has a length of 250 mm.

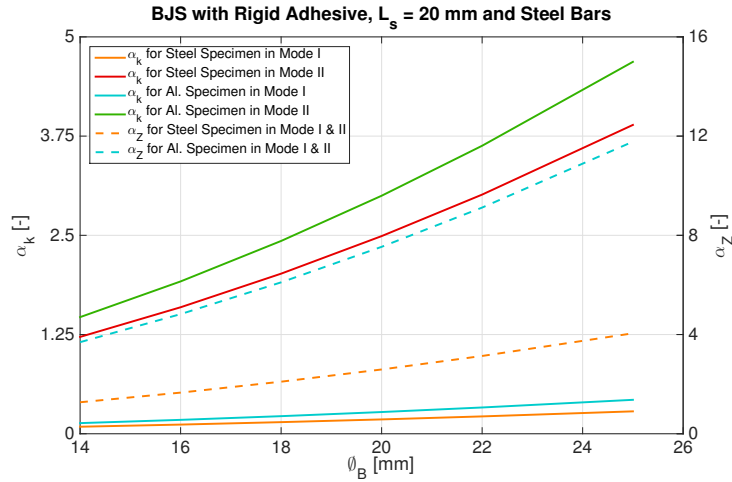


Figure 3.17: Ratio comparison for BJS of 20 mm length, with rigid adhesives and Stainless Steel bars.

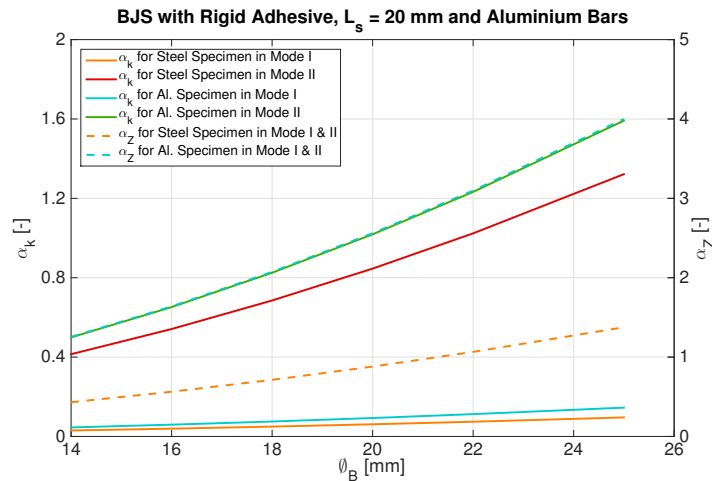


Figure 3.18: Ratio comparison for BJS of 20 mm length, with rigid adhesives and Aluminium Alloy bars.

Figures 3.17, 3.18 and 3.19 show the variation of impedance and stiffness ratios versus the bars diameter,  $\phi_B$ , for BJS of 20 mm length, with rigid Adhesives ( $E_{Ad} = 4$  GPa) and bars of Stainless Steel, Aluminium and Titanium Alloy, respectively.

As stated in subsection 3.1.3, the specimen stiffness,  $k_s$ , depends on the test mode, which means that, for each specimen, there are two stiffness ratio curves - one for mode I specimen and another for mode II specimen. However, as previously referred, it is considered that, when studying the wave impedance ratio, there is no distinction for between modes I and II. This assumption is reasonable, because wave impedance depends only on the specimen's cross-section area,  $A_s$  and the material properties,  $E$

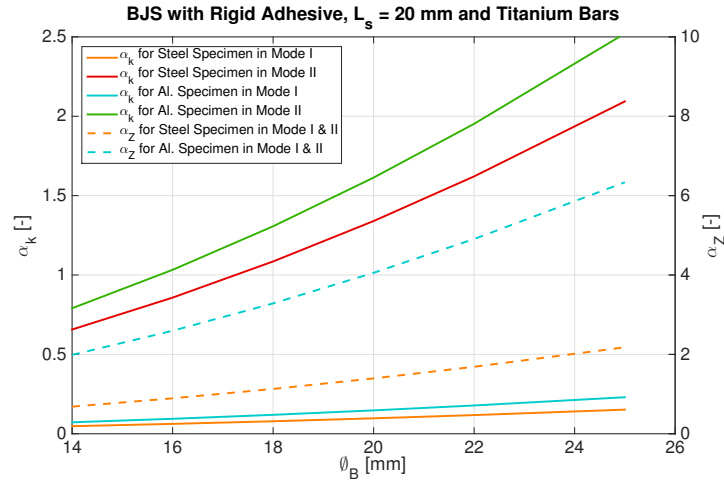


Figure 3.19: Ratio comparison for BJS of 20 mm length, with rigid adhesives and Titanium Alloy bars.

and  $\rho$ .

From Figures 3.17 to 3.19, it is deduced that both impedance and stiffness ratios increase with the bar diameter,  $\phi_B$ , because the bar's stiffness increases with its cross-section area, as seen in equation (3.16). However, when comparing stiffness ratios for various kind of specimen, the aforementioned variation is more visible for mode II specimen, which means that mode I specimen has higher stiffness than mode II specimen.

It is noteworthy to mention that specimen with Steel substracts have higher stiffness than specimen with Aluminium substracts. Therefore, the stiffness ratio for specimen with Steel substracts is smaller than specimen with Aluminium substracts. The same can be said when comparing impedance ratios,  $\alpha_z$ , for specimen with Steel and Aluminium substracts.

The stiffness ratios for Steel bars is higher than that of Titanium Alloy bars, which is also higher than that of Aluminium Alloy bars. This is due to the fact that Steel has a higher elasticity modulus than Titanium, and the latter's elasticity modulus is also higher than Aluminium. This tendency is also observed when comparing impedance ratios for the various bar materials. Impedance ratios are higher when bars are made of Stainless Steel and lower when bars are made of Aluminium Alloy. Setups with Titanium Bars have impedance ratios that are larger than Aluminium bar setups, but smaller than Steel bar setups.

For the cases represented in Figures 3.17 to 3.19, the values obtained for both ratios satisfy the recommendations presented in the scientific literature, reviewed in subsection 2.3.

Figure 3.20 presents the impedance and stiffness ratios versus the bars diameter,



$\varnothing_B$ , for BJS of 20 mm length with soft adhesives ( $E_{Ad} = 1$  MPa) and Stainless Steel bars.

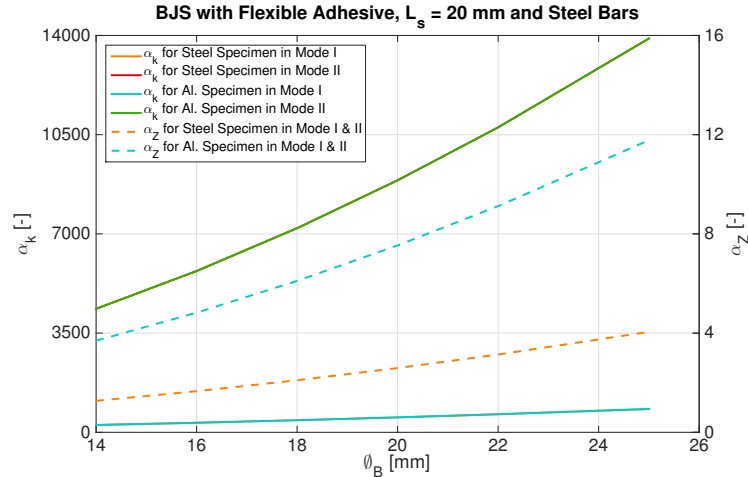


Figure 3.20: Ratio comparison for BJS of 20 mm length, with flexible adhesives and Stainless Steel bars.

It should be noted that for both impedance ratios, the results presented in Figures 3.20 and 3.21 are identical to those of Figure 3.17, since both substrates and bars are of the same material.

However, one can observe that the resulting stiffness ratios have increased drastically, being of at least two orders of magnitude higher than those for BJS with rigid adhesives. In other words, the specimen stiffness is much lower than the bars stiffness. It's also noteworthy to mention that the stiffness ratios are slightly higher for specimen with Aluminium substrates, although the difference is almost negligible given their order of magnitude.

It is verified that there is a drastic change in order of magnitude between stiffness for mode I and mode II specimen. While mode I specimen has a range of stiffness ratio roughly between 100 and 1000, mode II specimen's range of stiffness ratio varies between 4000 and 14000.

These values do not correspond to the recommendations outlined in section 2.3, where the bar and the specimen stiffness should be approximately equal. This is observed even for Aluminium Alloy bars, which are used for SHPB machines that test soft materials [3]. Consequently, further studies of Ratios with BJS are required for flexible bonding materials.

Figure 3.21 shows the impedance and stiffness ratios versus the bars diameter,  $\varnothing_B$ , for BJS of 10 mm length with rigid adhesives and Stainless Steel bars. Once again, it can be observed that the impedance ratios are identical to those of Figures 3.20 and 3.17, due to the aforementioned reasons. It is also observed that specimen with Aluminium

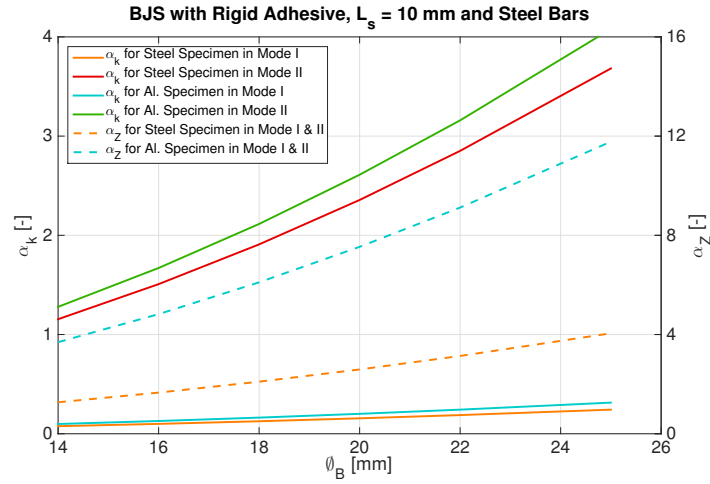


Figure 3.21: Ratio comparison for BJS of 10 mm length, with rigid adhesives and Stainless Steel bars.

Substrates have higher stiffness ratios than specimen with steel substrates, and that mode I specimen are stiffer than mode II specimen.

Upon closer comparison with the results obtained in Figure 3.17, it is observed that while the specimen stiffness is higher with a lower length (due to the fact the stiffness ratios are slightly lower), the differences are negligible. This means that the specimen stiffness does not vary significantly with the specimen length.

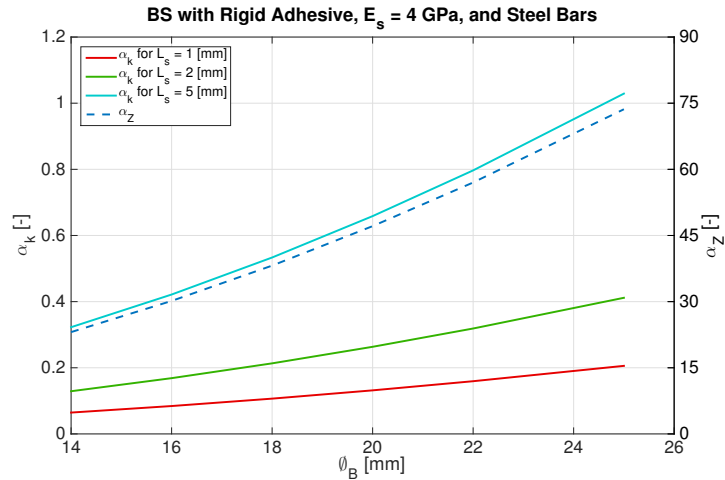


Figure 3.22: Ratio comparison for BS, with rigid adhesives and Stainless Steel bars.

Figures 3.22 and 3.23 present the impedance and stiffness ratios versus the bars diameter,  $\phi_B$ , for Stainless Steel bars and BS of rigid and flexible adhesives, respectively.

Similarly to the previous cases, it is observed that the stiffness ratio is higher for a higher bar diameter,  $\varnothing_B$ , and is lower for a smaller length of specimen,  $L_s$ . However, stiffness ratios are lower for BS, when compared to BJS with both rigid and soft adhesives, respectively. This occurs because adhesive Young Modulus is smaller than any of the metallic materials considered for the Pressure Bars.

Upon a closer look at the stiffness ratio of rigid bulk specimen, it can be said the obtained values depend significantly with the specimen's length,  $L_s$ . Specimen of length 5 mm have almost the same stiffness as those of the Stainless Steel bars, but a 1 mm length specimen has approximately ten times the stiffness of the bar. This tendency is even more visible with both Titanium and Aluminium Alloy bars, whose elasticity moduli are quite smaller than that of Steel.

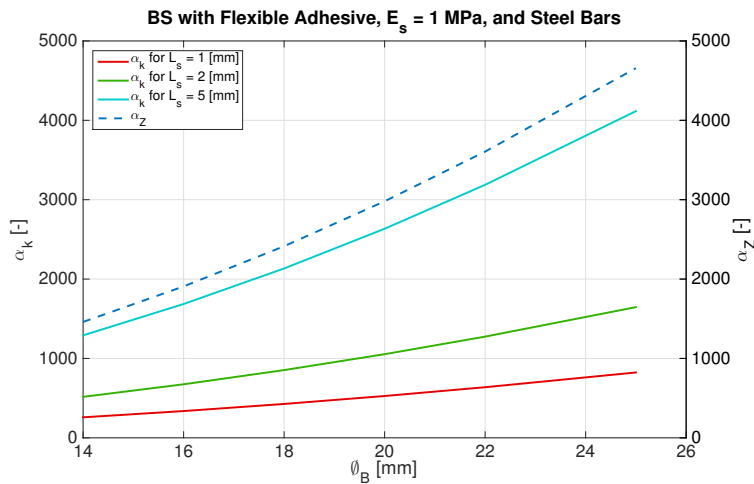


Figure 3.23: Ratio comparison for BS, with flexible adhesives and Stainless Steel bars.

Conversely, the impedance ratio for this case is quite high when compared with cases where BJS are studied, because both the elasticity moduli and mass densities of metals are quite higher than those of the adhesives. This tendency is less significant for Aluminium and Titanium bars, but they are still visible. This is also observed when studying the same relation for flexible bulk specimen, with  $E_{Ad} = 1$  MPa, where pulse impedance ratios are two order of magnitude higher than those of BS of rigid adhesives.

Comparing the stiffness ratios of soft adhesive BS with their rigid counterparts, one sees that flexible specimen are less stiffer than the bars of any metallic material. Once again, this is due to the low elastic modulus of a flexible adhesive.

### 3.3 Specimen & Bar Specifications

In this section, several conclusions regarding the project of the Kolsky Pressure Bars and the Specimen used are presented.

## Specimen Geometry

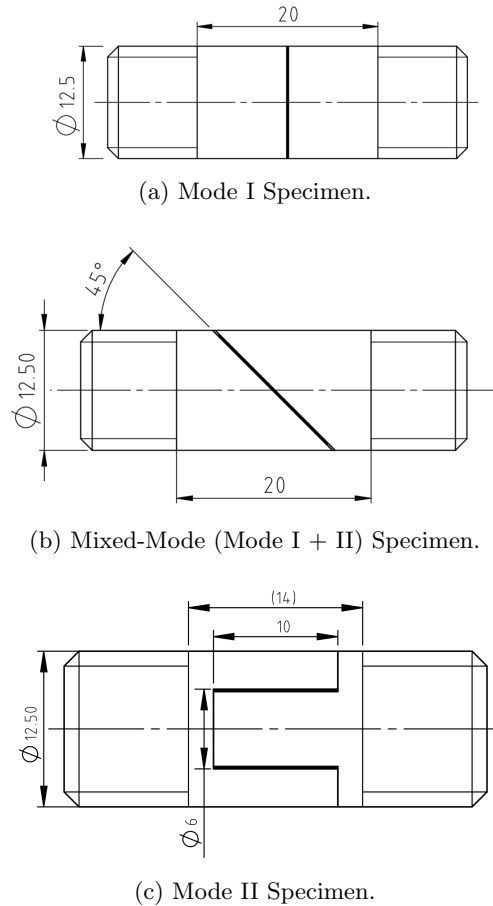


Figure 3.24: Designed Bonded Joint Specimen (BJS).

The results obtained using the models presented in subsection 3.1 showed that BJS with a diameter,  $\varnothing_s$ , of 12.5 mm do satisfies the recommendations of 2.3, at least when the adhesive is rigid. Figure 3.24 shows the geometry chosen for Mode I, Mixed-Mode and Mode II specimen, respectively. These geometries were determined following the previously obtained results, and the expertise of ADFEUP with adhesives and the specimen used with the Drop-weight machine.

Some notes should be highlighted regarding the presented specimen. The mixed-mode specimen of Figure 3.24b has the adhesive positioned with a  $45^\circ$  angle. However, this is merely an indicative value, since this inclination angle can be freely defined. Both mode I and mixed-mode specimen have a useful length of 20 mm (without threaded connections), while mode II specimen has been limited to 14 mm. This value is merely indicative, but must be larger than 10 mm length where there is a bonded joint. The bonded joint is only applied for a length of 10 mm, so that its bonding area is approximately equal to those of both mode I and mixed-mode bonded joints.

No geometry was defined for the Bulk Specimen, because after much deliberation with ADFEUP researchers, it was determined that these specimen may not be used for SHPB tests. Bulk Specimen cannot be manufactured with precise dimensions and have dimensional imprecisions, that may cause several unwanted wave reflections, possibly even trapping part of the wave for a long period of time. As such, it is advised to have a more thorough study of the viability on designing and testing adhesive bulk specimen.

#### **Testing of Flexible Adhesives**

As seen in the study of the stiffness and wave impedance ratios, the results for specimen of soft adhesive materials (both bulk and bonded joint) do not follow the expected values indicated in section 2.3. This problem occurs because both adhesive stiffness and wave impedance are several orders of magnitude lower than those of the pressure bars. This is a common problem for characterizing the behaviour of soft materials, which have the following characteristics: low stiffness, low wave impedance and low strength [3].

The mechanical response of soft materials is sensitive to loading conditions due to the aforementioned characteristics. The low wave speed of a flexible/soft adhesive makes stress equilibrium an harder condition to achieve in Kolsky Bars and, accordingly, specimen uniform deformation is not achieved. A possible solution is to have thinner specimen, which ease the occurrence of stress equilibrium during the start of the material deformation. It also alleviates possible stress wave attenuation in specimen of viscoelastic materials. However, thin specimen may cause unwanted interfacial friction between specimen and bars, leading to non-uniform uniaxial stress loading. Non uniform deformation in the axial direction may also lead to stress and strain gradients in the same direction, which are caused by axial inertia encountered in dynamic loading. Due to the Poisson's effect, the axial inertia also leads to radial inertia in the specimen and, consequently, may produce unwanted extra axial stress.

When characterizing soft materials, one observes that materials having lower wave impedance tend to make a nearly full reflecting of the incident wave. As such, the transmitted stress wave has extremely low amplitude, which means that regular strain gauges are not sufficiently sensitive to measure weak signals with reasonable signal-to-noise ratios. Highly sensitive transducers need to be applied in order to measure such weak signals [3].

Given these issues, a deeper study of the Kolsky Bar setups for soft material testing needs to be proposed to test flexible adhesives. Among the mentioned issues, several guiding principles should be mentioned to better solve these problems such as:

- Further study the design of flexible/soft adhesive specimen (both bulk and bonded joint), to achieve stress equilibrium and to mitigate axial and radial inertia effects;
- Study thoroughly SHPB setups that characterize soft materials, in order to implement a versatile impact testing machine that can characterize all kind of adhesives;

- Implement a sensitive instrumentation measuring system to adequately measure the low amplitude transmitted stress wave.

### Pressure Bar Specifications

When evaluating the results, several conclusions can be pointed as to some of the dimensions the pressure bars should have.

When first analyzing the charts displaying the striker bar length versus the different geometric, material and specimen response variables, it is verified that striker bars of any considered metallic materials has approximately the same length. However, when studying the required impact velocity for pulse generation with Stainless Steel bars, one sees that a lower striker bar velocity,  $v_{SB}$  is required to attain the desired specimen stress,  $\sigma_s$ , and specimen strain-rate,  $\dot{\epsilon}_s$ , when compared to Titanium or Aluminium Alloy Bars.

In order to determine the best length for the striker bar, the obtained striker bar lengths were analyzed. The results are significantly different depending on the type of specimen considered. When BJS were analyzed, the length,  $L_{SB}$ , was below 0.3 meters, independently of the bar's material. However, for BS, the lengths varied drastically with the specimen's length,  $L_s$ , reaching values of up to 1.8 meters. These values are, of course, unrealistic and depend on the required failure energy, which is high for most adhesives. In this case, one must have a stress wave of low amplitude and extremely long time duration, and thus, being able to fracture a specimen, which is unwanted. It is then considered that a striker bar length of 0.25 meters is a good choice to characterize specimen. This value is used for the study of stiffness ratio,  $\alpha_k$ .

Given the results, a bar diameter,  $\varnothing_B$ , needs to be determined. Since it is considered that the Pressure Bars should be made of Stainless Steel, a bar diameter needs to be chosen so that it satisfies:

- That the specimen's stiffness and the stiffness of the loaded bar portion have the same order of magnitude;
- That the bar's wave impedance shouldn't be over 10 times the specimen's impedance.

After analyzing all ratios for Stainless Steel bars, a bar diameter of 20 mm seems to represent a good value, at least for characterizing both rigid adhesive bulk specimen as well as for BJS with rigid adhesives.

Either the bar diameter,  $\varnothing_B$ , or the bar material may be different for characterizing flexible adhesives. However, as previously stated, further study is needed to have an optimized SHPB setup for characterizing these materials.

### Machine Architecture

One dimension that was not defined so far is the length of the incident and the transmission bars. These lengths depend on the SHPB architecture adopted. Since it is intended for the test machine to do either compression or tensile impact testing, the

pressure bar setup needs to be flexible to change from one load condition to the other. In this manner, a SHPB setup architecture is proposed in Figure 3.25 that is able to perform both types of tests.

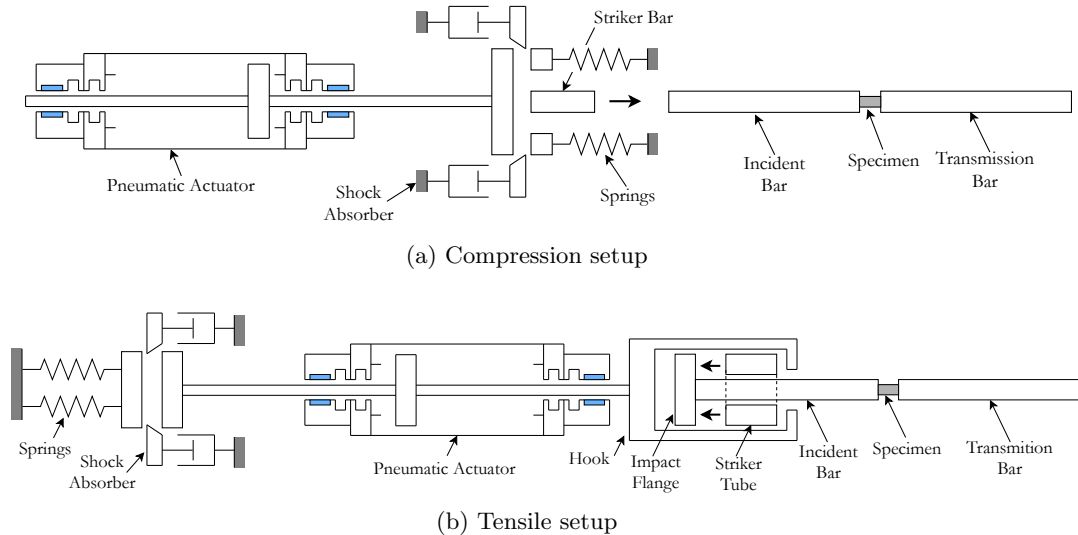


Figure 3.25: Adopted SHPB setup architecture.

The compression setup is quite simple, and similar to those normally used, with the exception of a pneumatic actuator to launch the striker bar. This setup uses the traditional pressure bars, where the striker bar impacts the free end of the incident bar, generating a stress wave moving towards the specimen. The specimen is placed in between the incident and the transmission bars. However, the striker bar is launched by a non-conventional pneumatic cylinder that can reach high velocities. This means that a specially designed braking system for the actuator's rod is needed, since, as previously seen, velocities of up to  $25 \text{ m s}^{-1}$  may be required.

This braking system is composed of mechanical springs, that store the rod's kinetic energy until it stops. At this point, the elastic energy will be given back to the rod, making it to move in the opposite direction. When this motion begins, shock absorbers will act, forcing the rod to slowly move to a resting point where the springs are no longer loaded.

The tensile setup works in almost the same way as the compression setup, but the actuator moves in the opposite direction, launching a striker tube with a hook attached to the actuator's rod. This striking element is sent towards an impact flange, generating a tensile wave. The pressure bar setup here is quite similar to the direct loading SHPB tensile setup shown in Figure 2.11.

With the proposed SHPB setup architecture just described, one can define the lengths of the incident and transmission bars. Normally, a bar should be able to store an entire pulse without it being reflected and/or transmitted. As previously stated, this

length is normally twice that of the striking element. However, for this tensile setup, the incident bar needs to be three times the length of the striker bar/tube, because it includes the length of the striking element [15, 11]. Therefore, the incident bar should have a minimum length of 750 mm and the transmission bar should have a length of 500 mm. Such values are important for the mechanical design of the pressure bars, but should not be considered definitive values, since mechanical and dimensional constraints may weight in the final length of these bars.

Finally, the dimensioning of the striker tube is also required. Since it should have the same wave impedance as the striker bar, and since they will be both made of the same material, then both elements should have the same cross-section area. Considering that the striker tube's inner diameter is equal to the incident bar's diameter, the outer diameter of the striker has a value of 28.3 mm.



## Chapter 4

# Functional Simulations

Given the study of several design architectures for the SHPB Tensile test machine, and given the study of requirements, a system that can launch the striking element at high speeds needs to be designed. As determined in Chapter 3, the required impact velocities can be of up to  $25 \text{ m s}^{-1}$ , or more, and therefore, non-conventional actuators need to be considered. Another important factor in the design of the actuator is that it needs to launch the striking element in both directions, in order to generate tensile and compression waves.

With these factors in mind for the design of the Kolsky Bar test machine, a non-conventional actuator needs to be conceived. As such, it was considered that a symmetric double-rod pneumatic cylinder, like the one schematically represented in Figure 4.1, would be the best actuator for the test machine.

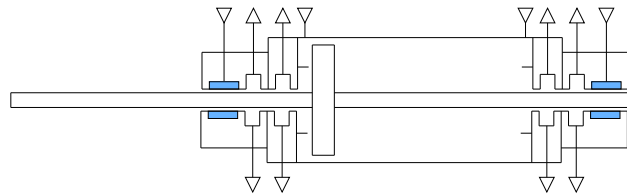


Figure 4.1: Schematic representation of the non-conventional actuator.

In order to launch the striking element at high velocities, this linear actuator must be designed with some special functional characteristics such as:

- Being able to move horizontally;
- Having reduced or no friction between moving elements;
- Having high accelerations, or in other words, attaining high velocities in short periods of time.

In order to achieve this, several design features and characteristics are considered for the cylinder. First of all, in order to remove dry friction between elements, the actuator should have neither piston seals, nor rod seals, nor guiding elements. This means that both rods and piston need to be supported by other means, like air bearings, that are represented in blue in Figure 4.1. This issue will be further studied in Chapter 5. Moreover, by removing seals in both the rods and the piston, there is a volume that connects both chambers, as well as each chamber and the atmosphere. This means that there is a leakage mass flow between both chambers (through the piston) and between the pressurized chamber and the atmosphere (through the rod and specially made exhaust channels in the cylinder).

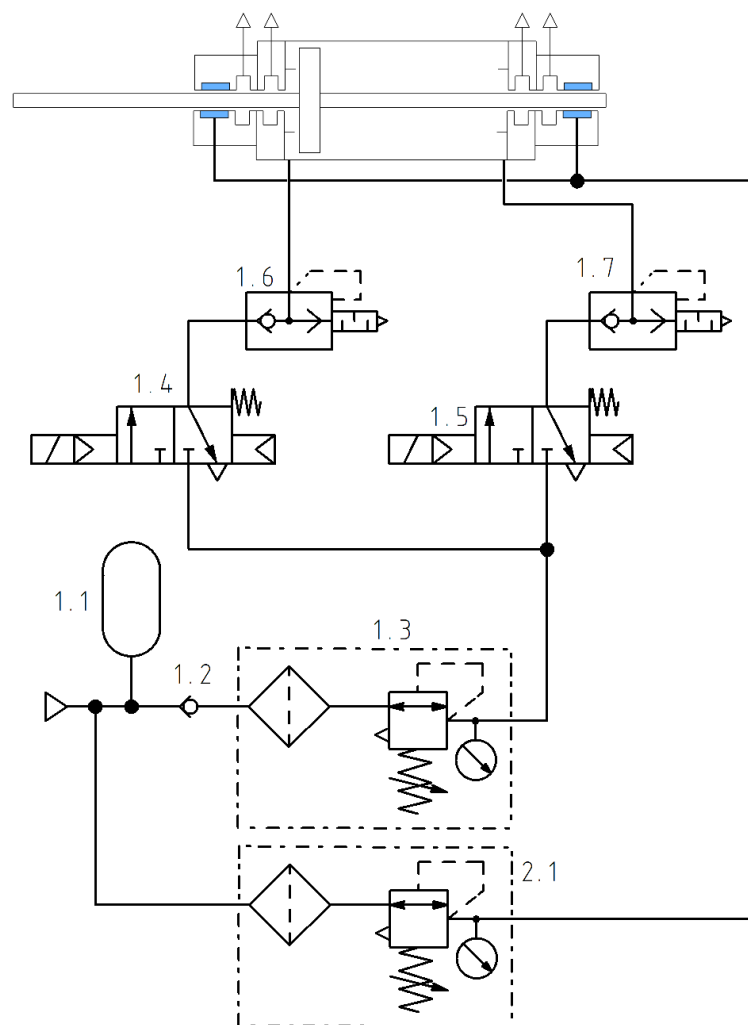


Figure 4.2: Proposed Pneumatic Circuit for the Actuator.

When defining the requirements of the actuation system, it was considered that a high air mass flow would be required in order to attain high velocities. As such, a

---

special air source needs to be implemented in this system that can maintain high air mass flow without fluctuations, like a dedicated reservoir.

In order to help initializing the piston movement without air flow going directly to the exhaust channels, an initially sealed antechamber needs to be incorporated, allowing a smooth starting motion. With this, in the first few millimeters of motion, air will only accelerate the piston.

These dynamics are important to define the behaviour of the cylinder and, consequently, a functional simulation of the whole system needs to be developed to validate the chosen architecture.

Also, several ways of stopping the actuator, after launching the striker bar, were put forth, and they needed to be simulated, to evaluate their feasibility and efficiency in stopping the rod. At first, it was considered that the cylinder's rod/piston would be stopped using a mechanical spring and air from the active pneumatic chamber.

In this setup, first, the rod/piston would be accelerated by maintaining one chamber pressurized, while the other chamber would release the air to the atmosphere, mainly through a quick exhaust valve. Afterwards the rod would hit the mechanical springs, launching the striking element. In this moment the mechanical springs would only store the kinetic energy. Therefore, both chambers would be short-circuited in order to have the same pressure. Afterwards, both chambers would depressurize in a controlled manner by letting air flow from each chamber to the atmosphere through a metering valve. This system was simulated using Simulink<sup>®</sup>, and the obtained results had shown that the rod would oscillate at high frequency, and thus had an unstable transient response. Therefore, this strategy was not adopted.

Another braking system is proposed using springs and shock absorbers, as presented in section 3.3. Figure 4.2 presents the pneumatic circuit for the actuator with this braking system (not shown in Figure). In this system, the rod/piston are accelerated in the same way, by commuting the directional valve 1.4, connecting the reservoir 1.1 to a pressurized chamber. Meanwhile, the other chamber exhausts air to the atmosphere through the quick exhaust valve 1.7. When the rod hits the mechanical springs, air from the pressurized chamber is released to the atmosphere through the quick exhaust valve 1.6. Thus the springs convert the rod's kinetic energy into potential elastic energy. Afterwards, the springs start to give back the stored energy, causing the rod to move in the opposite direction. When this movement starts, the shock absorbers start to act, causing the rod to slowly move until all the elastic energy is given back, thus stopping the rod/piston. With this system, it is possible to dissipate the energy stored by the springs, without exceeding the velocity limits imposed by commercially available shock absorbers.

In section 4.1 the systems models are described, presenting the assumptions, the laws and the simplifications used to obtain the models. As each model is presented, the values of geometric, dynamic and fluid constants are presented. In section 4.2, the main

results of the simulations are presented.

## 4.1 Subsystem Models

In order to validate the designed actuation pneumatic system and mechanical braking system, and to determine the velocities that the striker bar can reach, a functional simulation was implemented, using Simulink<sup>®</sup>, that includes several mathematical models. The system model, represented in Figure 4.3, is comprised of:

- A compressed air reservoir model that simulates the pressure source;
- Pneumatic valve subsystems, modeled according to ISO 6358 standard, that command the actuator;
- The pneumatic cylinder subsystem, which in turn, is composed of simplified thermodynamic model for each chamber, as well as a model that calculates air leakages;
- The actuator mechanics subsystem, based on Newton's 2<sup>nd</sup> Law of Motion.

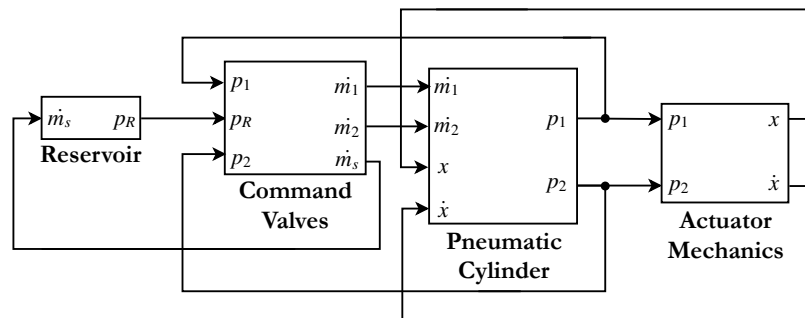


Figure 4.3: Schematic representation of the actuation system in block diagrams.

One should note that, these simulations were processed without a physical actuator present. Therefore, it is impossible to determine if the thermodynamic behaviour of each air chamber is adiabatic ( $n = \gamma = 1.4$ ), isothermic ( $n = 1$ ), or polytropic ( $1 < n < 1.4$ ). So, in order to have a good idea of the actuator's performance, the system was simulated with both extremes of polytropic index,  $n$ .

In the following subsection, each subsystem is described.

### 4.1.1 Reservoir

The actuator that launches the striker bar needs a stable pressure source in order to attain high velocities without fluctuations. The cylinder should not depend on the compressed air network, because the supply air mass flow is neither high enough, nor is sufficiently stable for a high speed actuation. Therefore, it is wise to have a pressurized air reservoir as a pressure source for the pneumatic system. The chosen reservoir is presented in subsection 5.1.1.

A simple model was developed based on the Perfect Gas Law, which states that

$$p_R V_R = m_R R T_R \quad (4.1)$$

where:

- $p_R$  is the supply pressure, or, in other words, the air pressure inside the reservoir;
- $V_R$  is the volume of the reservoir, and has a value of  $61 \cdot 10^{-3} \text{ m}^3$ , as presented in Table 5.1;
- $m_R$  is the mass of air inside the reservoir;
- $R$  is the Specific Gas Constant ( $R = 287 \text{ J (kg K)}^{-1}$ );
- $T_R$  is the absolute temperature of the air in the reservoir.

Differentiating and rearranging equation (4.1), the following relation is obtained

$$\frac{dp_R}{dt} = \frac{-\dot{m}_R R T_R}{V_R} \quad (4.2)$$

where  $\dot{m}_R$  is the mass flow that leaves the reservoir. The minus sign was added to equation (4.2) to reflect that air mass flow is leaving the reservoir, thus causing a lowering of pressure,  $p_R$ . This model is developed assuming that air temperature inside the reservoir,  $T_R$ , is constant. Further, it is assumed that the reservoir is at ambient temperature ( $T_R = 25 \text{ }^\circ\text{C} = 298.15 \text{ K}$ ). Figure 4.4 shows the simulation diagram block model implemented in Simulink<sup>®</sup>.

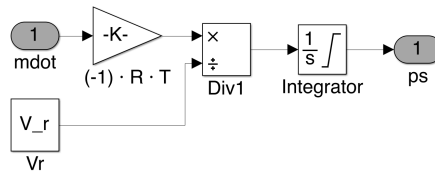


Figure 4.4: Simulink<sup>®</sup> Model of the Reservoir sub-system.

### 4.1.2 Pneumatic Valves

The cylinder begins to move when a signal is given to the directional pneumatic valve, thus allowing air to flow from the reservoir to the chamber that causes the motion of the rod (which is the **Pneumatic Chamber 1** sub-system implemented inside the **Pneumatic Cylinder** block, to be described in subsection 4.1.3). At the same time, air will flow from **Pneumatic Chamber 2** to the atmosphere through a quick exhaust valve. Afterwards, the cylinder will start to slow down thanks to the mechanical springs. In this moment, air inside the **Pneumatic Chamber 1** will flow through another quick exhaust valve towards the atmosphere.

One must model both input and output mass flows of the pneumatic cylinder, in order to determine its behaviour. This means that the three valves need to be simulated.

In light of this, a mathematical model for pneumatic valves was implemented based on the ISO 6358 Standard [23], which states that the mass flow of chamber  $j$ ,  $\dot{m}_j$ , is given by

$$\dot{m}_j = \begin{cases} C p_u \rho_a \sqrt{\frac{T_a}{T_u}}, & \text{where } r_p \leq b^* \\ C p_u \rho_a \sqrt{\frac{T_a}{T_u}} \sqrt{1 - \left(\frac{r_p - b^*}{1 - b^*}\right)^2}, & \text{where } r_p > b^* \end{cases} \quad (4.3)$$

where:

- $C$  is the sonic conductance;
- $p_u$  and  $T_u$  are the pressure and absolute temperature of the upstream point, respectively;
- $\rho_a = 1.225 \text{ kg m}^{-3}$  and  $T_a = 298.15 \text{ K}$  are the mass density and absolute temperature of air at ambient conditions, respectively;
- $r_p$  is the ratio between the upstream and the downstream pressure,  $r_p = \frac{p_u}{p_d}$ , where  $p_d$  is the pressure downstream;
- $b^*$  is the critical pressure ratio that separates sonic and choked (or subsonic) flows. This value can be determined experimentally [23], according to standard ISO 6358, which should be stated by the valve manufacturer. Alternatively, if such information is not available, the critical pressure ratio value can be estimated from the study of compressible flow by equation (4.4) [5, 24].

$$b^* = \frac{p^*}{p_o} = \left(\frac{2}{\gamma + 1}\right)^{\frac{\gamma}{\gamma - 1}} = 0.5283 \quad (4.4)$$

In the following equation,  $p^*$  and  $p_o$  are the critical and the stagnation pressures respectively, and  $\gamma = 1.4$  is the heat capacity ratio of air, or, in other words, the polytropic index when the air is adiabatic.

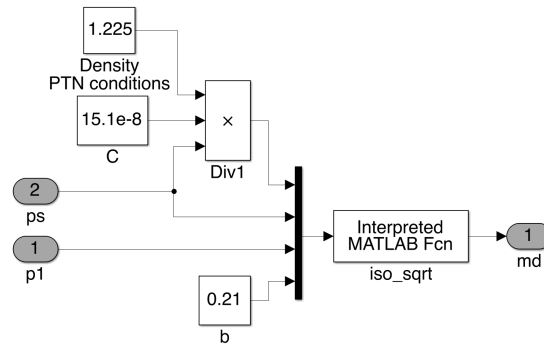


Figure 4.5: Simulink<sup>®</sup> Model of Valve.

Figure 4.5 shows the simulation diagram block model implemented in Simulink® for a valve. Both the upstream and the downstream points for each valve depend on the stage of operation. It should be noted that, if both values of sonic conductance,  $C$ , and critical pressure ratio,  $b$ , are not present in valve characteristics, then these values are calculated according to the available effective area,  $A_e$ , defined as

$$A_e = C \rho_a \sqrt{s R T_a} \quad (4.5)$$

where:

- $C$  represents the sonic conductance to be calculated, and  $R$  is the Specific Gas Constant;
- $\rho_a$  and  $T_a$  are the mass density and absolute temperature of air at ambient conditions, respectively;
- $s$  is the coefficient of compressibility effect, defined as

$$s = \frac{1}{1 - b^*} \quad (4.6)$$

according to ISO 6358 Standard [23].

It should be noted that when the system transitions to the next state, there may be commutation of one or several valves, which is not done instantly. In other words, there is a commutation time for each valve due to several electrical and mechanical delays. However, some valve data-sheets do not include this information, and simulating this transient behaviour may lead to further indetermination. As such, the valve commutation was ignored for simulation purposes.

Table 4.1: Parameters for simulation of valves.

Valve	Type	$C$ [m <sup>3</sup> (Pa s) <sup>-1</sup> ]	$b^*$	Upstream point
1.4	Directional Valve	$15.1 \cdot 10^{-8}$	0.21	Reservoir
1.6	Quick Exhaust Valve	$3.47 \cdot 10^{-7}$	0.5283	Pneumatic Chamber 2
1.7	Quick Exhaust Valve	$3.47 \cdot 10^{-7}$	0.5283	Pneumatic Chamber 1

Table 4.1 identifies the simulated valves and presents the various parameters required for simulation.

### 4.1.3 Pneumatic Cylinder

As previously stated, the actuator is a linear cylinder with double rod, and has some special characteristics due to its geometric and mechanical features, such as:

- The lack of piston seals and guiding tape in the piston, as well as wiper-seals and rod seals, to reduce the friction between the piston/rods and the cylinder's wall/heads. Consequently, there will be leakage between both chambers of the linear actuator as well as between each chamber and the atmosphere;

- The division of one chamber into two parts by a rod seal, when the piston is on one end of its stroke, like on normal impact pneumatic cylinders. This means that, for the smaller chamber, there is an antechamber where pressurized air will first enter. After a small displacement, the rod seal will no longer seal the antechamber, opening access to the other part of the pneumatic chamber. This will make a discrete change on chamber volume.

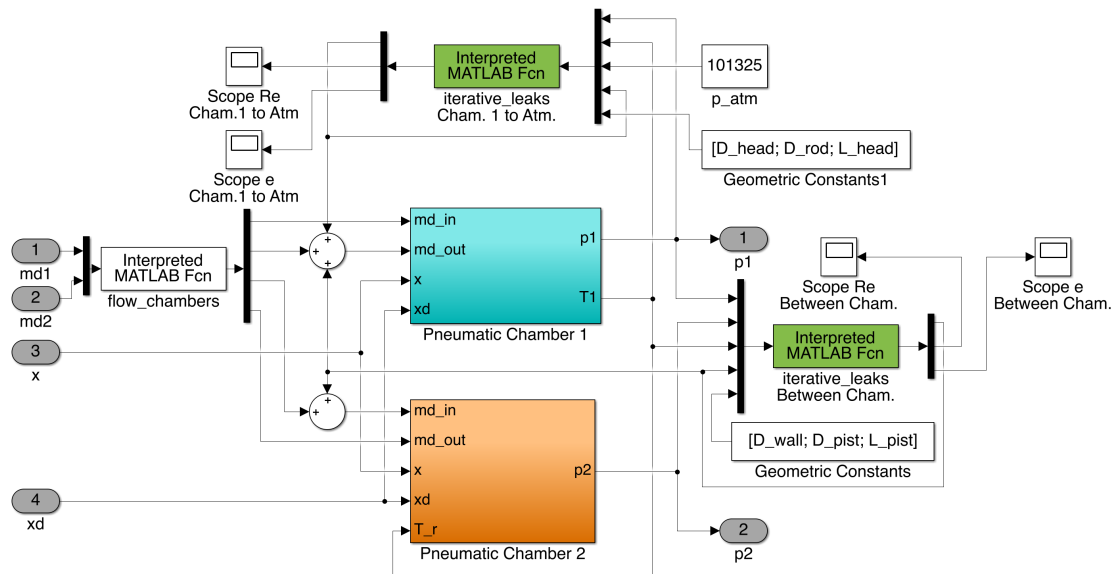


Figure 4.6: Simulink<sup>®</sup> Pneumatic Cylinder sub-system.

Knowing these characteristics, a model of the Pneumatic Cylinder is proposed, shown in Figure 4.6, where several sub-systems are implemented, namely:

- The **Pneumatic Chamber 1**, that promotes the rod movement, and the **Pneumatic Chamber 2**, that exhausts all of its pressurized air to the atmosphere;
- The models that simulate both the leakages between each chamber, as well as the leakage between Chamber 1 and the atmosphere. This model is implicit, thus, it is implemented with a *Interpreted MATLAB Function* named `iterative_leaks`;
- A *Interpreted MATLAB Function* named `flow_chambers` that determines which mass flow will go to each of the two chambers.

It is important to mention that the air leaks between the **Pneumatic Chamber 2** and the atmosphere are not modeled, since the air in this chamber will exit mostly through the quick exhaust valve 1.7. Also, as mentioned before, this subsystem is simulated twice, comparing the extreme cases where the gas present in both chambers is either adiabatic ( $n = \gamma = 1.4$ ), or isothermic ( $n = 1$ ).

Both the pneumatic chamber and the iterative leakage models are explained in the the following parts.



## Pneumatic Chambers

When the actuator moves, air enters and leaves the chambers, according to the given commands and the implemented pneumatic circuit. The thermodynamic behaviour of the fluid in each chamber affects the launch of the striking element. Therefore, modeling the behaviour of the fluid in both chambers is relevant in determining the behaviour of the system.

The used model is deduced with the application of the First Law of Thermodynamics applied to an open system, and the Principle of Mass Conservation. The following hypotheses were considered:

- The air is an ideal gas and, as such, follows the Ideal Gas Law, which states that

$$p = \rho R T \quad (4.7)$$

where  $p$  is the absolute pressure in each chamber,  $\rho$  represents the mass density of the fluid,  $T$  is the gas temperature in each chamber, and  $R$  is the specific gas constant;

- the chambers are at the same height and the velocities of the air inside the chamber are negligible. This means that kinetic and potential energies are negligible;
- the thermodynamic variables pressure,  $p$ , temperature,  $T$ , and mass density,  $\rho$ , are uniform inside both chambers;
- the viscous work due to the flow inside each chamber is negligible.

The obtained model is given by the two differential equations

$$\begin{cases} \frac{dp}{dt} = -\gamma \frac{p}{V} \frac{dV}{dt} + \gamma \frac{R}{V} \dot{m}_{in} T_{in} - \gamma \frac{R}{V} \dot{m}_{out} T - \frac{\gamma-1}{V} \dot{Q} \\ \frac{dT}{dt} = \frac{T}{V} \frac{dV}{dt} (1-\gamma) - \dot{m}_{out} \frac{RT^2}{Vp} (\gamma-1) + \dot{m}_{in} \frac{RT}{Vp} (\gamma T_{in} - T) - \frac{\gamma-1}{pV} \dot{Q} \end{cases} \quad (4.8)$$

where:

- $V = V(x)$  is the volume of each chamber;
- $\dot{m}_{in}$  and  $\dot{m}_{out}$  are the mass flows that enter and leave each chamber, respectively;
- $T_{in}$  is the temperature of the air entering the chamber;
- $\dot{Q}$  is the heat transfer between each actuator chamber and its walls.

One should note that the variables  $p$ ,  $T$ ,  $V$  and  $\rho$  refer to the pressure, temperature, volume and mass density of the air in each chamber [25, 26].

The model is too complex for simulation purposes and, therefore, some simplifications are considered. However, this approach must not jeopardize the accuracy of the physical model. Firstly, it is considered that the heat transfer between each chamber

and the surrounding walls is negligible. The movement of the rod should be quick and the heat transfer is quite small in that time period, which means that its contribution to the thermodynamic behaviour is small.

The second simplification is to consider that the temperature variation is negligible in the small amount of time that takes for the actuator to move. Since force and kinematic variables depend directly on air pressure, it is reasonable to remove temperature as a state variable. Alternatively, the temperature differential equation is replaced by the polytropic law, which states that

$$T = T_a \left( \frac{p}{p_a} \right)^{\frac{n-1}{n}} \quad (4.9)$$

where  $p_a$  and  $T_a$  are the ambient pressure and temperature, respectively. As previously stated, it is impossible to determine the polytropic index,  $n$ , in order to define the thermodynamic behaviour of each chamber. It is known that this index can vary between the isothermal process ( $n = 1$ ) and the adiabatic process ( $n = \gamma = 1.4$ ), which means that simulating the two cases should yield the extreme thermodynamic behaviours and, consequently, the extreme dynamic behaviours of the rod are also obtained.

The simplified model for an adiabatic process is given by

$$\begin{cases} \frac{dp}{dt} = -\gamma \frac{p}{V} \frac{dV}{dt} + \gamma \frac{R}{V} (\dot{m}_{in} T_{in} - \dot{m}_{out} T) \\ T = T_a \left( \frac{p}{p_a} \right)^{\frac{n-1}{n}} \end{cases} \quad (4.10)$$

and if the isothermal process is considered, then the following system is obtained

$$\begin{cases} \frac{dp}{dt} = -\frac{p}{V} \frac{dV}{dt} + \frac{R}{V} (\dot{m}_{in} T_{in} - \dot{m}_{out} T) \\ T = T_a \end{cases} \quad (4.11)$$

One should note that the volume of a chamber,  $V$ , is a discontinuous function due to the discrete change when physical contact between the rod and the rod seal ceases to exist. When this happens, the pressurized antechamber and a dead volume are connected. This can be described by the following equation

$$V = V(x) = \begin{cases} V_A + A_A x, & \text{when } x \leq x_{tr} \\ V_A + V_D + A x, & \text{when } x > x_{tr} \end{cases} \quad (4.12)$$

where:

- $V_A$  and  $V_D$  are the initial volume of the antechamber and the dead volume of the chamber, respectively;
- $x$  is the rod's position;
- $x_{tr}$  is the position when the discrete transition of volume occurs;

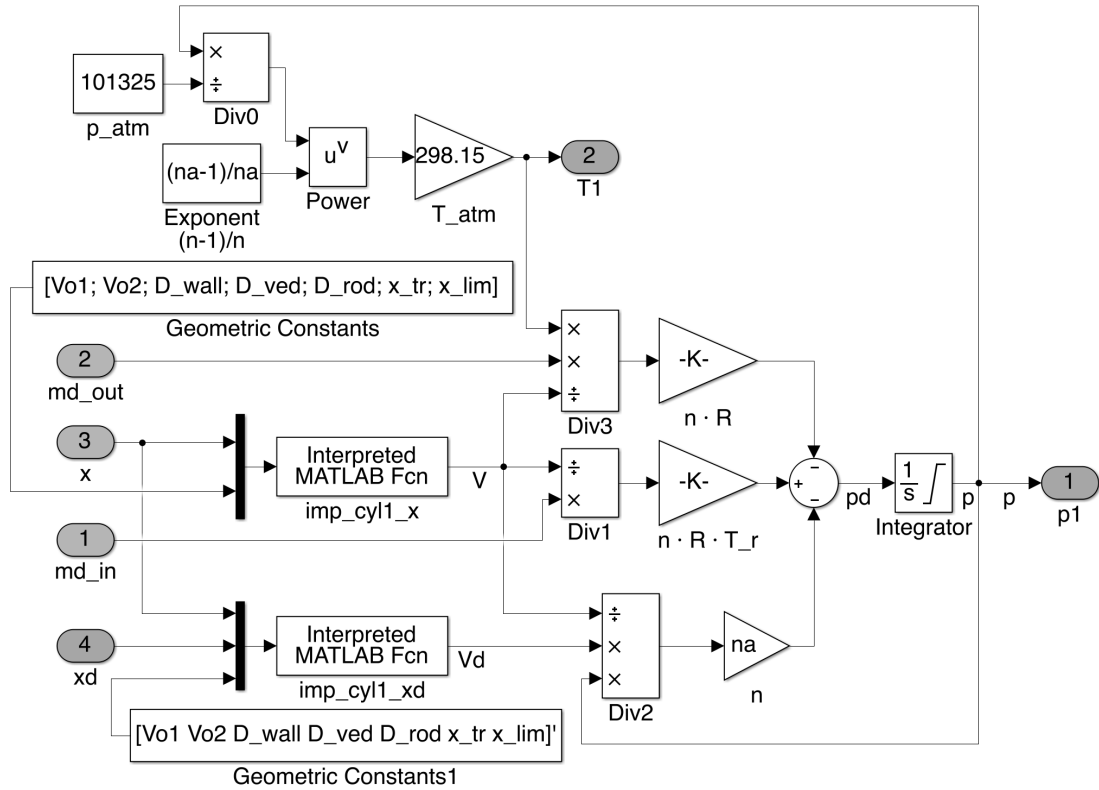


Figure 4.7: Simulink<sup>®</sup> model of the Pneumatic Chamber 1, for the Adiabatic Process.

- $A_A$  and  $A$  denote the areas of the antechamber and of the chamber, respectively, and are calculated as

$$A_A = \frac{\pi}{4} (\varnothing_{wall}^2 - \varnothing_{seal}^2) \quad (4.13a)$$

$$A = \frac{\pi}{4} (\varnothing_{wall}^2 - \varnothing_{rod}^2) \quad (4.13b)$$

where  $\varnothing_{wall}$  is the diameter of the cylinder's wall,  $\varnothing_{rod}$  is the diameter of the cylinder's rods, and  $\varnothing_{seal}$  is the diameter of the seal that separates the antechamber and the dead volume.

The rate of volume change,  $\dot{V} = \frac{dV}{dt}$  is given by

$$\dot{V} = \frac{dV}{dt} = \begin{cases} A_A \dot{x}, & \text{when } x \leq x_{tr} \\ A \dot{x}, & \text{when } x > x_{tr} \end{cases} \quad (4.14)$$

where  $\dot{x}$  is the velocity. Equations (4.12) and (4.14) are only applicable for the Pneumatic Chamber 1. For the Pneumatic Chamber 2, one should replace  $x$  with  $(l - x)$ , in both equations, where  $l$  is the stroke of the cylinder.

As an example, Figure 4.7 shows the Simulink<sup>®</sup> model of the Pneumatic Chamber

1, considering that its thermodynamic behaviour is adiabatic. Table 4.2 lists all the geometric variables used in this model and its values.

Table 4.2: Geometric variables and values for **Pneumatic Chamber 1** and **Pneumatic Chamber 2**.

Variable	Value
Wall Diameter, $\varnothing_{\text{wall}}$ [m]	0.140
Rod Diameter, $\varnothing_{\text{rod}}$ [m]	0.040
Seal Diameter, $\varnothing_{\text{seal}}$ [m]	0.050
Antechamber Volume, $V_A$ [m <sup>3</sup> ]	$3.6 \cdot 10^{-4}$
Chamber's Dead Volume, $V_D$ [m <sup>3</sup> ]	$1.6 \cdot 10^{-5}$
Position for Volume Transition, $x_{tr}$ [m]	0.012

### Iterative Leakage Models

There are no seals between the piston and the cylinder wall, as well as between each rod and its respective head. Therefore, it is important to implement a mathematical model that simulates the air leakage, in order to more comprehensively study the actuator, the thermodynamic behaviour of each chamber and, consequently, its mechanical behavior. All leakage channels have a ring cross-section of small constant area and the difference between both types of channels is only dimensional. As such, all leakage channels can be simulated using the same model.

The problem of studying and defining a valid and accurate leakage model for control purposes was addressed by Moreira [27], In his work, a model was determined using the following assumptions:

- The cross-section area of leakage channel,  $A_l$ , is constant in its entire length;
- The fluid flow is unidirectional and parallel with the normal direction of the cross-section area. Thus, the leakage mass flow,  $\dot{m}_l$ , can be calculated by means of

$$\dot{m}_l = \rho v A_l \quad (4.15)$$

where  $\rho$  is the mass density of air and  $v$  is the flow velocity.

- The mass density of air,  $\rho$ , is not constant, but can be calculated using the perfect gas law presented in equation (4.7);
- Given that the air passing through the leakage channel is being throttled and that the channel is of small length, then the flow can be considered isenthalpic. Since the air can be described according to the perfect gas law, then the flow is also isothermic;
- The mass flow is not sufficiently large to observe turbulent flow, and, as such, it can be assumed that the leakage flow is laminar;
- The velocity of the piston is negligible, given that air will flow with higher speed than the piston.

It should be noted that the two last assumptions are not completely valid. In the sequel, equations (4.16) to (4.21) follow the modeling ideas proposed by Moreira.

Applying the force balance to a differential volume of infinitesimal length, one can obtain, after some mathematical manipulation, the following equation

$$\dot{m}_l = \frac{-R T_u \Psi_{IJ} + \sqrt{(R T_u \Psi_{IJ})^2 - 8 \ln \left( \frac{p_{l,u}}{p_{l,d}} \right) R T_u \Psi_I (-p_{l,u}^2 + p_{l,d}^2)}}{4 \ln \left( \frac{p_{l,u}}{p_{l,d}} \right) R T_u \Psi_I} \quad (4.16)$$

where:

- $T_u$  is the absolute temperature of the upstream pneumatic chamber;
- $p_{l,u}$  and  $p_{l,d}$  are the upstream and downstream absolute pressures at both ends of the throttling, respectively, as shown in Figure 4.8;
- $\Psi_I$ ,  $\Psi_J$  and  $\Psi_{IJ}$  are constants dependent on the geometry of the leakage channel and on the viscosity of air,  $\mu$ , that can be assumed constant for a small temperature range, and are expressed by

$$\Psi_I = \frac{1}{A_l^2} [\text{m}^{-4}] \quad (4.17a)$$

$$\Psi_J = \frac{96 A_l \mu}{(\varnothing_e - \varnothing_i)} \frac{(\varnothing_e + \varnothing_i)}{(\varnothing_e^2 - \varnothing_i^2)} L [\text{kg s}^{-1}] \quad (4.17b)$$

$$\Psi_{IJ} = \Psi_I \Psi_J [\text{kg (m}^4 \text{ s)}^{-1}] \quad (4.17c)$$

where  $\varnothing_e$  and  $\varnothing_i$  are the outer and inner diameter of the ring channel, respectively, and  $L$  is its length. It should be noted that, according with the bibliography, the value of air viscosity,  $\mu = 18,46 \cdot 10^{-6} \text{ N s m}^{-2}$ , for atmospheric pressure and temperature was assumed [28].

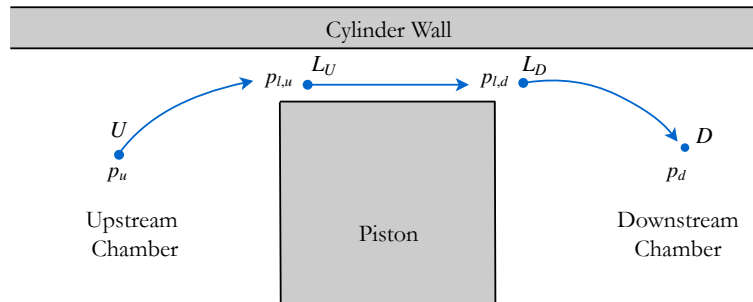


Figure 4.8: Schematic representation of leaks between chambers.

Equation (4.16) is valid between two points of a completely developed laminar flow, but does not relate fluid pressures at each chamber. As such, equation (4.16) does

not take into account fluid acceleration and deceleration, as well as the compressibility effects. It is then necessary to relate mathematically the upstream chamber pressure,  $p_u$ , with the pressure at the beginning of the channel,  $p_{l,u}$ . It is also necessary to relate the pressure at the end of the channel,  $p_{l,d}$ , with the downstream chamber pressure,  $p_d$ . Moreira initially proposed using the First Law of Thermodynamics between points  $U$  and  $L_U$ , as well as  $L_D$  and  $D$ , thus obtaining

$$p_u - p_{l,u} = (K_{L,u} + 1) \frac{1}{2} \frac{\dot{m}_l^2}{A_l^2 \rho_{l,u}} \quad (4.18)$$

$$p_{l,d} - p_d = (K_{L,d} - 1) \frac{1}{2} \frac{\dot{m}_l^2}{A_l^2 \rho_{l,d}} \quad (4.19)$$

where  $K_{L,u}$  and  $K_{L,d}$  are the local loss coefficients, with values between 0 and 1.

When trying to use these equations to relate the pressures between both ends of the throttling channel and each chamber, several problems emerge such as the difficulty of obtaining precise values of  $K_{L,u}$  and  $K_{L,d}$  to accurately represent the pressure drops. Another drawback was that these equations were not a practical model for control purposes, since they were dependent on the leakage mass flow,  $\dot{m}_l$ . Furthermore, even if these equations (with arbitrated values for  $K_{L,u}$  and  $K_{L,d}$ ) were adopted, the simulations would not reflect measured results from experimental setups, because:

- Exact measurements of the chamber pressure cannot be acquired;
- Leakage channels do not have a perfect geometry and are susceptible to dimensional and geometric tolerances;
- Air is assumed to be idle inside each pneumatic chamber, which is not accurate.

Given these problems, an alternative solution was proposed. Equation (4.19) can still be applied between points  $L_D$  and  $D$ , with a local loss coefficient of  $K_{L,d} = 1$ . This means that  $p_d$  is equal to  $p_{l,d}$  and, consequently, the model needs only two equations. However, an empirical law, is adopted for describing the pressure drop between points  $U$  and  $L_U$

$$p_{l,u} = p_d - \Psi_l \frac{p_u - p_d}{\frac{p_{l,u}}{T_u} \bar{R}} \quad (4.20)$$

where  $\Psi_l$  is a constant that needs to be determined experimentally. After some mathematical manipulations, the following relation is obtained

$$p_{l,u} = \frac{p_u + \sqrt{p_u^2 - 4 \Psi_l (p_u - p_d) T_u \bar{R}}}{2} \quad (4.21)$$

It was experimentally verified that equation (4.21) yields better results, than equations (4.18) and (4.19).

Given this state of affairs identified in the work of Moreira, it seems clear that such

approach cannot be used, since there is no way to determine  $\Psi_l$  without experimental results [27].

The present work adopts an iterative program to calculate the leakage mass flow,  $\dot{m}_l$ , based on equations (4.16), (4.18) and (4.19). Using the pressures in each chamber to start the process, the MATLAB function first calculates the leakage mass flow and afterwards the pressure in both extreme ends of the throttling channel, which will be used in the following iteration. In order to determine that the algorithm converges to an acceptable value, the relative error of iteration  $j$ ,  $e|_j$ , is calculated using the obtained mass flow in iterations  $j - 1$  and  $j$ ,  $\dot{m}_l|_{j-1}$  and  $\dot{m}_l|_j$ , respectively, as presented

$$e|_j = \left| 1 - \frac{\dot{m}_l|_j}{\dot{m}_l|_{j-1}} \right| \quad (4.22)$$

If the relative error at iteration  $j$ ,  $e|_j$ , is smaller than 1%, then it can be assumed that the function has converged to an acceptable value. It should be noted that the local loss coefficients have the values  $K_{L,u} = K_{L,d} = 0.5$  [24].

Table 4.3 lists all the geometric variables used to calculate the leakage mass flow, between **Pneumatic Chamber 1** and **Pneumatic Chamber 2**, and between, **Pneumatic Chamber 1** and the atmosphere.

Table 4.3: Geometric variables used in `iterative_leaks`.

Variable	Value	Leakage Model
Wall Diameter, $\varnothing_{\text{wall}}$ [m]	0.140	Flow between both chambers
Piston Diameter, $\varnothing_{\text{piston}}$ [m]	0.1397	
Piston Length, $L_{\text{piston}}$ [m]	0.050	
Head Diameter for Rod, $\varnothing_{\text{head}}$ [m]	0.041	Flow between <b>Pneumatic Chamber 1</b> and the atmosphere
Rod Diameter, $\varnothing_{\text{rod}}$ [m]	0.040	
Length of leakage channel in head, $L_{\text{head}}$ [m]	0.085	

#### 4.1.4 Actuator Mechanics

After obtaining the pressure in each chamber of the cylinder, one can use Newton's 2<sup>nd</sup> Law,  $\sum F = m \ddot{x}$ , to determine the rod's kinematic variables. The sum of forces exerted on the rod is the sum of the forces caused by the pressure in **Pneumatic Chamber 1**,  $F_1$ , and **Pneumatic Chamber 2**,  $F_2$ , and the estimated viscous force caused by air viscosity,  $F_{\text{air}}$ . Besides these, a spring force,  $F_{Sp}$ , and a dissipative force caused by a Shock Absorber,  $F_{SA}$ , will act at specific positions. Thus, the force equilibrium equation is written as

$$F_1 - F_2 - F_{\text{air}} - F_{Sp} - F_{SA} = m \ddot{x} \quad (4.23)$$

where  $m$  is the system's mass, composed of the rod/piston and the striker bar/tube. The total mass of these components are approximately equal to 10 kg.

The rigidity of the mechanical components was not considered, since it is negli-

gible when compared with other mechanical effects. Forces caused by the air compressibility were modeled in subsection 4.1.3. Figure 4.9 shows the Simulink<sup>®</sup> block model for the **Actuator Mechanics** sub-model.

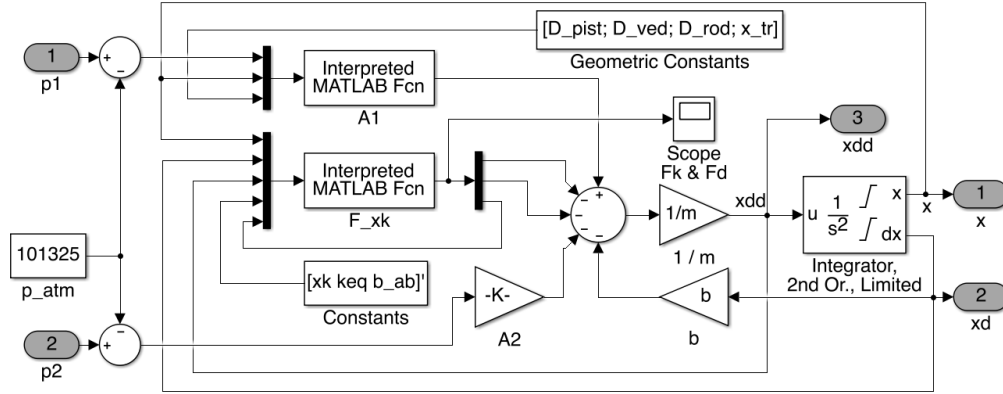


Figure 4.9: Simulation Model of the **Actuator Mechanics**.

The cylinder's stroke limits were inserted in the **Integrator, Second-Order Limited** as the position integration limits. When the rod reaches one of the limits, the integrator imposes null velocity for the rod.

In the following parts, a discussion is made regarding the forces included in equation (4.23).

### Forces caused by fluid dynamics

The force caused by the pressure in **Pneumatic Chamber 1**,  $F_1$ , is defined by the multiplication of the relative pressure,  $p_1 - p_a$ , and the area of the piston where the pressure acts,  $A_{\text{piston},1}$ , obtaining

$$F_1 = (p_1 - p_a) A_{\text{piston},1} \quad (4.24)$$

The piston area,  $A_{\text{piston},1}$  is defined as

$$A_{\text{piston},1} = \begin{cases} \frac{\pi}{4} (\varnothing_{\text{piston}}^2 - \varnothing_{\text{seal}}^2), & x \leq x_{tr} \\ \frac{\pi}{4} (\varnothing_{\text{piston}}^2 - \varnothing_{\text{rod}}^2), & x > x_{tr} \end{cases} \quad (4.25)$$

where  $\varnothing_{\text{piston}}$  is the diameter of the piston,  $\varnothing_{\text{seal}}$  is the seal diameter,  $\varnothing_{\text{rod}}$  is the rod diameter and  $x_{tr}$  is the position when the discrete transition of volume occurs. These values are listed in Table 4.2 and 4.3.

The force caused by the pressure in **Pneumatic Chamber 2**,  $F_2$ , is calculated in the same way. However, it is considered that the piston area is constant, because, ideally,



the piston should not reach the Seal. The force  $F_2$  can be expressed as

$$F_2 = (p_2 - p_a) A_{\text{piston},2} = (p_2 - p_a) \frac{\pi}{4} (\varnothing_{\text{piston}}^2 - \varnothing_{\text{rod}}^2) \quad (4.26)$$

The force caused by air viscosity,  $F_{\text{air}}$ , is given by

$$F_{\text{air}} = b_{\text{air}} \dot{x} \quad (4.27)$$

where  $b_{\text{air}}$  represents the viscous-friction coefficient and  $\dot{x}$  is the velocity of the rod. The value of  $b_{\text{air}}$  is very low for this actuator, since it was designed with the purpose of having low friction. Therefore, after trying several values iteratively, a value of  $b_{\text{air}} = 100 \text{ N s m}^{-1}$  was considered as a good approximation.

### Elastic spring Force

The elastic force caused by the mechanical springs is defined as

$$F_{Sp} = \begin{cases} 0, & x \leq x_{Sp} \\ k_{Sp} (x - x_{Sp}), & x > x_{Sp} \end{cases} \quad (4.28)$$

where  $k_{Sp}$  is the springs stiffness and  $x_{Sp}$  is the position where the springs start acting. This position divides the actuator's stroke in two parts. When the piston/rod does not reach this position, the striking element accelerates. When the piston/rod reaches this position (considered  $x_{Sp} = 0.5 \text{ m}$  in the simulation), the striker bar/tube is launched and the actuator begins to slow down.

A value for the springs stiffness needs to be defined and, an energetic study was made to determine its value. The rod's kinetic energy needs to be completely converted in potential elastic energy by the spring system. It can then be deduced that

$$k_{Sp} = \frac{2K}{(l - x_{Sp})^2} = \frac{2 \frac{m \dot{x}|_{\text{max}}^2}{2}}{(l - x_{Sp})^2} \approx 70000 \text{ N m}^{-1} \quad (4.29)$$

where  $l$  is the actuator's stroke,  $m$  is the rod/piston mass (approximately 10 kg),  $\dot{x}|_{\text{max}}$  is the rod's maximum velocity (*a priori* assumed as being  $25 \text{ m s}^{-1}$ ), and  $K$  is the rod's kinetic energy.

The obtained value for  $k_{Sp}$  was first introduced in the functional simulations. However, the results for rod's position showed that not all of the kinetic energy was converted into elastic energy, and, consequently, the piston collided with the actuator's head at the extreme end of its stroke. This was observed because, it was assumed that both chambers would be at atmospheric pressure, which may not happen. As such, a higher spring stiffness was heuristically estimated and the spring system should have a stiffness of  $1.20 \cdot 10^5 \text{ N m}^{-1}$ .

### Shock Absorber Force

A dissipative force is needed to stop the actuator's rod/piston. This means that a shock absorber must be selected. This element is required to dissipate, at least, the rod's kinetic energy, with an approximate value of 3125 J, and must have a minimum stroke of 0.3 meters. With these requirements in mind, the shock absorber model CA3X12EU-1, manufactured by ACE - Automation Control Equipment, is selected. Table 4.4 presents the main characteristics of the selected industrial shock absorber [29].

Table 4.4: Characteristics of Industrial Shock Absorber CA3X12EU-1 [29].

Stroke [mm]	305
Max. Energy Capacity per cycle [J]	33900
Max. Velocity [ $\text{m s}^{-1}$ ]	5
Min. Return Force [N]	270
Max. Return Force [N]	730

According to ACE, the stopping force is constant in almost all of its stroke, as shown in Figure 4.10. Therefore, the dissipation energy,  $E_D$ , can be expressed as

$$E_D = F_{SA} l_{SA} \quad (4.30)$$

where  $F_{SA}$  represents the exerted force by the shock absorber, and  $l_{SA}$  is its stroke. The damping force generated by shock absorber,  $F_{SA}$ , is proportional to the velocity,  $\dot{x}$ , and can be defined as

$$F_{SA} = b_{SA} \dot{x} \quad (4.31)$$

where  $b_{SA}$  is the absorber's damping coefficient. Combining equations (4.30) and (4.31), one can calculate the maximum damping coefficient as

$$b_{SA} = \frac{E_D|_{\max}}{l_{SA} \dot{x}} = \frac{33900}{0.305 \cdot 5} \approx 22\,230 \text{ N s m}^{-1} \quad (4.32)$$

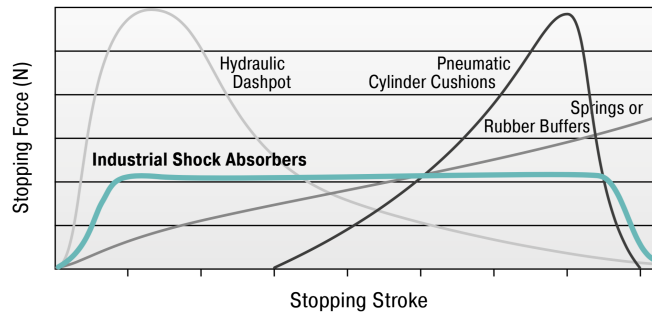


Figure 4.10: Comparison of ACE Shock Absorber Force versus its stroke, with other damping systems [29].

The shock absorber dissipation force,  $F_{SB}$ , presented in equation (4.23), can be defined in abstract terms, but, there is no explicit logical condition on where it is applied.

In other words, the position where the shock absorber starts exerting a force is dependent on the rod's kinematic behaviour, which is dependent on the initial pressure. Therefore, it is impossible to define the position where the shock absorber exerts force.

An auxiliary logical variable,  $S$ , is defined to determine when the rod's velocity is  $\dot{x} = -5 \text{ m s}^{-1}$ . When the rod attains this velocity, the variable  $S$  switches from 0 to 1. Since the shock absorbers will be placed excentrically to the rod's axis, unwanted torques may appear. By placing a second shock absorber in the symmetrical point, this torque disappears, which means that there will be two shock absorbers in parallel. Therefore, the damping coefficient is twice that of the selected shock absorber,  $b_{SA} = 2 \cdot 22\,230 = 44\,460 \text{ N s m}^{-1}$ . Then, the force exerted by the shock absorber,  $F_{SB}$ , is defined as

$$F_{SB} = S b_{SA} \dot{x} \quad (4.33)$$

As the chosen shock absorber is the one with the smallest dissipation capacity for a stroke of 0.3 meters, then it is decided that two absorbers of the same size should be placed. This means that the dissipation capacity is higher than required, ensuring a smoother operation.

## 4.2 Results

After having the models defined and knowing the parameters numerical values, the simulations can be performed. Several parameters were monitored, namely, the piston's position, velocity and the pressure for each chamber, which are represented in Figures 4.11, 4.12 and 4.13, respectively. In these Figures, it is considered that the initial relative pressure in both chambers is  $p_1 = p_2 = 8 \text{ bar}$  (or  $9 \text{ bar}$ , if the absolute pressure is considered).

When studying the position of the rod, one can see that initially it moves quite fast, almost reaching the end of the stroke in roughly 0.1 seconds. Indeed, the instant before the springs start acting on rod, the attained acceleration is of  $\ddot{x} = 700 \text{ m s}^{-2}$ . Afterwards, the springs start exerting a force contrary to the rod's movement, and, consequently, the rod's acceleration starts lowering. When the acceleration is null, the rod attains its maximum velocity, which may vary between  $22.3 \text{ m s}^{-1}$  and  $23 \text{ m s}^{-1}$ , depending if the air in pressure chambers are adiabatic or isothermic, respectively.

In a second phase, the actuator velocity lowers significantly and the rod's acceleration decreases rather quickly, attaining a minimum value of almost  $-2400 \text{ m s}^{-2}$ . It is in this instant that the rod's position attains its maximum value, reaching positions between  $0.76 \text{ m}$  (when the pneumatic chambers are adiabatic) and  $0.78 \text{ m}$  (when the pneumatic chambers are isothermic).

Afterwards, the rod starts moving in the opposite direction and its velocity is negative and decreasing. There is a small period of time when the rod moves in the opposite direction because the springs start giving back the stored energy to the rod.

When the rod's velocity reaches  $\dot{x} = -5 \text{ m s}^{-1}$ , the shock absorbers start acting

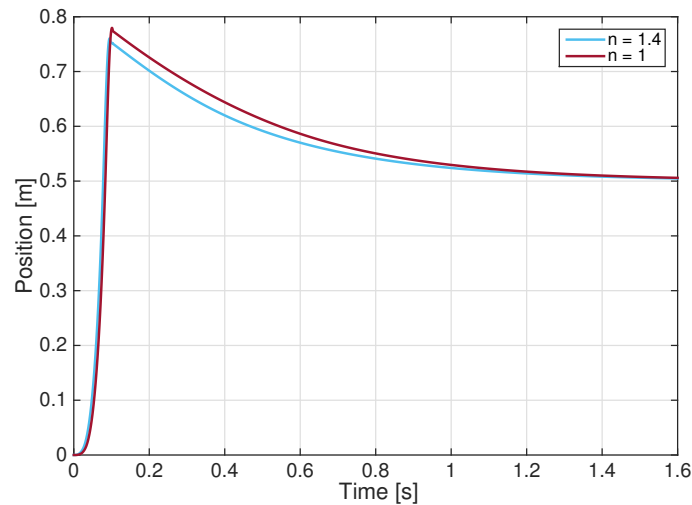


Figure 4.11: The rod position,  $x$ , versus time for the adiabatic ( $n = \gamma = 1.4$ ) and the isothermic ( $n = 1$ ) cases.

on the rod, forcing it to move slowly. Indeed, the rod's velocity augments, first attaining a value of  $\dot{x} = -0.5 \text{ m s}^{-1}$ . Afterwards, the velocity tends to zero as the springs decompress, and the rod's position tends exponentially to 0.5 m, where the spring no longer acts on the rod.

When observing the pressure behaviour in both chambers for the adiabatic and isothermic cases, it can be deduced that there are no major differences between each case. At first, pressure in **Pneumatic Chamber 2** drops quickly until it reaches the atmospheric pressure and no more mass flow travels through the quick exhaust valve (Valve 1.7 in Figure 4.2). Meanwhile the pressure behaviour in **Pneumatic Chamber 1** varies somewhat with the case considered. If one analyses the adiabatic case, it can be seen that the pressure drops 1 bar (roughly  $1 \cdot 10^5 \text{ Pa}$ ) as volume  $V_1$  expands. However, pressure  $p_1$  for the isothermic case remains mostly constant during the volume's expansion. This may be a result of the fact that the fluid's temperature varies if the chamber is considered adiabatic, while temperature remains constant if the chamber is isothermic.

When the rod hits the springs, the directional valve (Valve 1.4 in Figure 4.2) commutes, and air inside **Pneumatic Chamber 1** flows to the atmosphere through the quick exhaust valve (Valve 1.6 in Figure 4.2). In this instant, it is observed that pressure  $p_1$  drops exponentially with time, as expected. However pressure drops at a faster rate for the adiabatic case, when compared with the isothermic case. Once again, this may be explained due to the temperature behaviour between both cases.

Meanwhile, pressure inside **Pneumatic Chamber 2** rises temporarily roughly at instant 0.1 s for both cases. This coincides with the instant when the rod as stopped and starts moving in the opposite direction. It is then inferred from this behaviour that

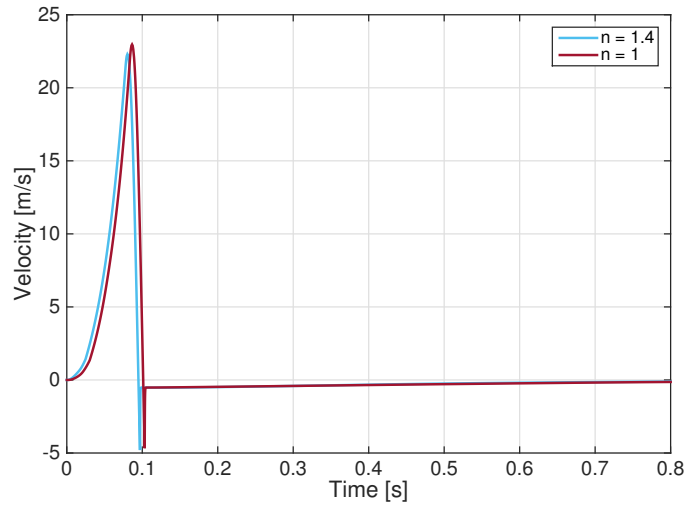


Figure 4.12: The rod velocity,  $\dot{x}$ , versus time for the adiabatic ( $n = \gamma = 1.4$ ) and the isothermic ( $n = 1$ ) cases.

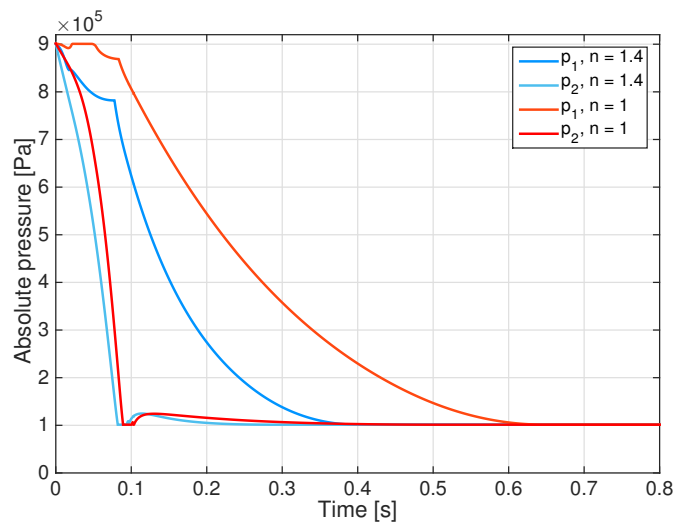


Figure 4.13: Pressures,  $p_1$  and  $p_2$ , as a function of time for the adiabatic ( $n = \gamma = 1.4$ ) and the isothermic ( $n = 1$ ) cases.

pressure  $p_2$  rises due to the fact that mass flows between both chambers due to the leakage channel, and the quick exhaust valve needs a residual pressure in order to let air flow to the atmosphere.

Overall, one concludes that the actuator has a stable behaviour and is able to attain the required velocities. However, more work needs to be done as to the influence of the initial pressure has in the cinematic variables.



## Chapter 5

# Mechanical Design

After having simulated the actuation system and validated its architecture, this chapter discusses the design of the actuator, its various mechanical parts, and the elements that integrate the pneumatic circuit.

Section 5.1 describes the pneumatic components that command the pneumatic cylinder. These are represented in the pneumatic circuit shown in Figure 4.2. Section 5.2 presents the mechanical design of the actuator.

### 5.1 Pneumatic Circuit

In this section, the selected pneumatic components for the SHPB machine actuator are described. These components are shown in the pneumatic circuit of Figure 4.2.

#### 5.1.1 Reservoir

As mentioned in chapter 4, a dedicated pneumatic reservoir needs to be implemented in the pneumatic circuit, in order for the actuator to have a stable supply of air, without pressure variations.



Figure 5.1: Pressurised gas cylinder from *Amtrol-Alfa* [30].

Given the pressures needed to sustain the functioning of the actuator, a high volume reservoir is needed (1.1 in Figure 4.2). A pressurized gas cylinder manufactured

by *Amtrol-Alfa*, presented in Figure 5.1 is chosen for this function. The catalogue does not present a reference code for this gas container, but its characteristics are summarized in Table 5.1 [30].

Table 5.1: Pressurised gas cylinder characteristics [30].

Height [mm]	1150
Diameter [mm]	300
Volume [dm <sup>3</sup> ]	61.0
Tare Weight [kg]	27.4

### 5.1.2 Air Filter & Regulator

The pneumatic components require a clean air mass flow in order to work under normal conditions. A stable regulation of the pressure must be included to assure stable functioning conditions. Therefore, an air filter and pressure regulator is selected for the main pneumatic circuit that controls the actuator's motion. Furthermore, another air supply unit that regulates the air flow for the air bushings needs to be selected.

The air filter and regulator combination for the main pneumatic circuit (1.2 in Figure 4.2) is the model AC40B-F06D, manufactured by SMC<sup>®</sup>. The equipment is composed of the air filter model AF40-06, and the pressure regulator model AR40-06 [31]. Figure 5.2 shows a 3D representation of this F.R. unit.

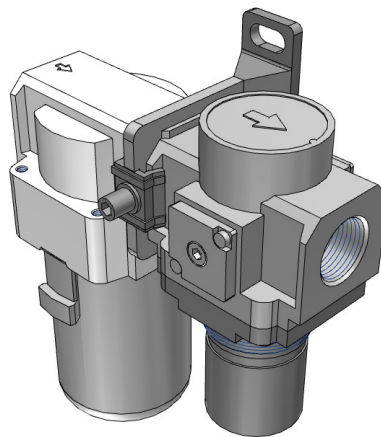


Figure 5.2: 3D representation of F.R. unit model AC40B-F06D [31].

For the air bushing pneumatic supply (2.1 in Figure 4.2), the model ACG20B-F02DG1, manufactured by SMC<sup>®</sup>, is selected for the air filter and regulator combination. The air filter and the pressure regulator are the models AF20 and ARG20, respectively [32].

Table 5.2 presents the most relevant specifications of the two F.R. units.



Table 5.2: Air filter and regulator specifications [31, 32].

Model	AC40B-F06D	ACG20B-F02DG1
Port size	G3/4	G1/4
Set pressure range [bar]	0.5 to 8.5	0.5 to 8.5
Maximum operating pressure [bar]	10	10
Nominal filtration rating [ $\mu\text{m}$ ]	5	5

### 5.1.3 Pneumatic Valves

As shown in Figure 4.2, the pneumatic circuit that controls the non-conventional actuator includes two directional valves (1.4 and 1.5 in Figure 4.2) and two quick exhaust valves (1.6 and 1.7 in Figure 4.2). Each directional valve controls the mass flow that enters the chamber to which it is connected. The quick exhaust valve allows air from a given pneumatic chamber to flow to the atmosphere as quickly as possible, therefore, allowing the actuator's rod/piston to reach high accelerations. Additionally, a check valve between the reservoir and the F.R. unit is present, in order to prevent back flow of air (1.2 in Figure 4.2). Figure 5.3 shows the selected valves.



Figure 5.3: Selected valves.

Table 5.3: SMC® VP 742 valve flow characteristics [33].

Port Size		G 1/2
1 $\leftrightarrow$ 2 or P $\leftrightarrow$ A	$C$ [ $\text{m}^3 (\text{Pa s})^{-1}$ ]	$15.1 \cdot 10^{-8}$
	$b^*$ [-]	0.21
	$\dot{V}$ [slpm]	3 637
2 $\leftrightarrow$ 3 or A $\leftrightarrow$ R	$C$ [ $\text{m}^3 (\text{Pa s})^{-1}$ ]	$15.3 \cdot 10^{-8}$
	$b^*$ [-]	0.22
	$\dot{V}$ [slpm]	3 707

The selected directional valve model, VP 742K-5YOD-04FA, presented in Figure 5.3a, is a 3/2 directional valve, of normally closed type. The valve is electrically actuated with pilot operation and is spring returned, also with pilot operation. As previously stated, the required actuator velocities are high, which means that this valve must have high flow characteristics. Tables 5.3 and 5.4 list the specifications of the valve. In is

noted that, the values of the critical ratio pressure,  $b^*$ , and sonic conductance,  $C$ , used during the simulations correspond to the values for flow between ports 1 and 2 ( $1 \leftrightarrow 2$  or  $P \leftrightarrow A$ ).

Table 5.4: SMC<sup>®</sup> VP 742 valve specifications [33].

Internal pilot operating pressure range [bar]	2 to 10
Response time at 5 bar [ms]	22 or less
Coil rated voltage [V]	$24 \pm 10\%$
Power consumption [W]	1.5
Dimensions [mm $\times$ mm $\times$ mm]	$162.1 \times 135.5 \times 66$
Manual override	Push-turn locking slotted type

The quick exhaust valve model AQ5000-F06, manufactured by SMC, is chosen to be included in the pneumatic circuit. This valve uses a diaphragm, made of Nitrile Rubber (NBR), as the element that closes the unused port [34]. Table 5.5 lists the valve's specifications. It must be noted that the value of sonic conductance,  $C$ , is deduced according to the method proposed in subsection 4.1.2, using the effective area for the OUT  $\leftrightarrow$  EXH connection.

Table 5.5: SMC<sup>®</sup> AQ5000-F06 valve specifications [34].

Operating pressure range [bar]	0.5 to 10
Port Size	G 3/4
Dimensions [mm $\times$ mm $\times$ mm]	$85 \times 75 \times 85$
Effective Area ( $1 \leftrightarrow 2$ or IN $\leftrightarrow$ OUT) [mm <sup>2</sup> ]	1.5
Effective Area ( $2 \leftrightarrow 3$ or OUT $\leftrightarrow$ EXH) [mm <sup>2</sup> ]	Push-turn locking slotted type

Finally, the check valve model XTO-647-04E, manufactured by SMC<sup>®</sup>, is chosen to integrate the pneumatic circuit. Figure 5.3c shows the valve and Table 5.6 shows its specifications.

Table 5.6: SMC<sup>®</sup> XTO-647-04E valve specifications [35].

Port Size	Rc 1/4
Operating Pressure Range [bar]	0.1 to 10
Sonic Conductance, $C$ [m <sup>3</sup> (Pa s)] <sup>-1</sup>	$10.5 \cdot 10^{-8}$
Critical Pressure Ratio, $b^*$	0.45
Dimensions [mm $\times$ mm]	$\varnothing 32 \times 55$

## 5.2 Mechanical Design of the Actuator

In this section, the mechanical design of the actuator, which is represented in Figure 5.4, and its components is discussed. This design is based on considerations first stated in Chapter 4, like the fact that:

- The cylinder's wall and the piston should not have any physical contact at all. Therefore, no piston seals or guide elements are present in the piston;

- The rods must be supported by means that do not involve physical contact between components. Air bushings are chosen to support the rods;
- At both cylinder stroke ends, there must be a sealed antechamber that allows the start of the rod's motion without air flowing out to the chamber.

It should be mentioned that the dimensions listed in the Tables 4.2 and 4.3 are present in the mechanical design of the actuator. The design of the assembly and its components was undertaken using *SolidWorks*. The mechanical drawings are present in Appendix B.

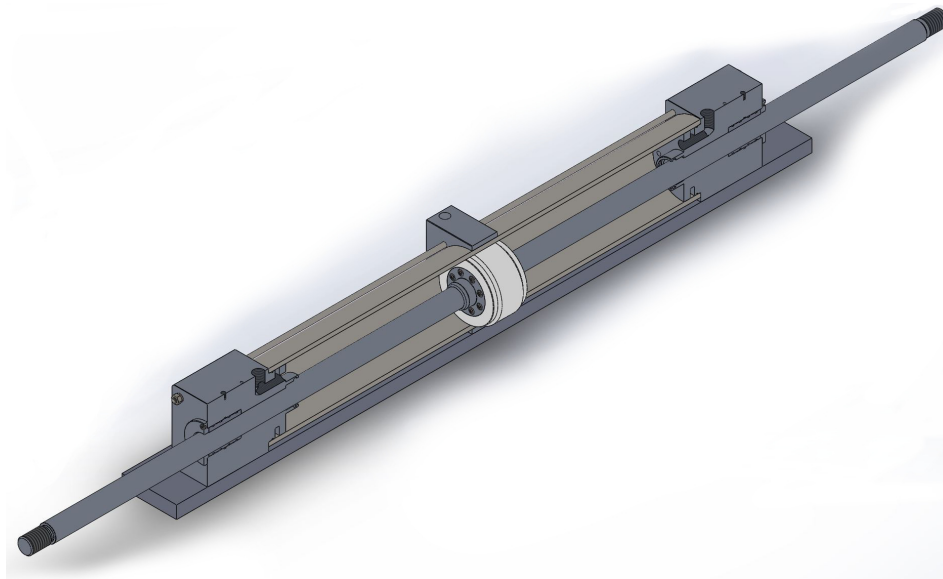


Figure 5.4: Pneumatic Actuator Assembly.

Besides the design characteristics mentioned, it should be considered that the rods are long and, consequently, they may have a high deflection due to their weight. Thus, the rods and the piston should be as light as possible while, at the same time, as rigid as possible.

### 5.2.1 Piston

#### Piston & Piston Cap

Normal pneumatic and hydraulics cylinders usually have steel or aluminium pistons. However, as previously stated, this actuator needs to have:

- A channel between both chambers, in order to minimize friction between elements, which means that the piston must not physically contact the cylinder wall. However, in the eventual case that there is contact between both elements, friction should still be as minimum as possible, in order to avoid hindering the actuator's performance;

- Rods/Piston with minimum weight possible, and, consequently, minimizing the deflection.

In light of this, the designed piston is made of Nylon, a polymer that is machinable, in order to assure tight tolerances for the leakage channel. This material is also a polymer, which means that it reduces the ensemble's weight when compared to metallic pistons.

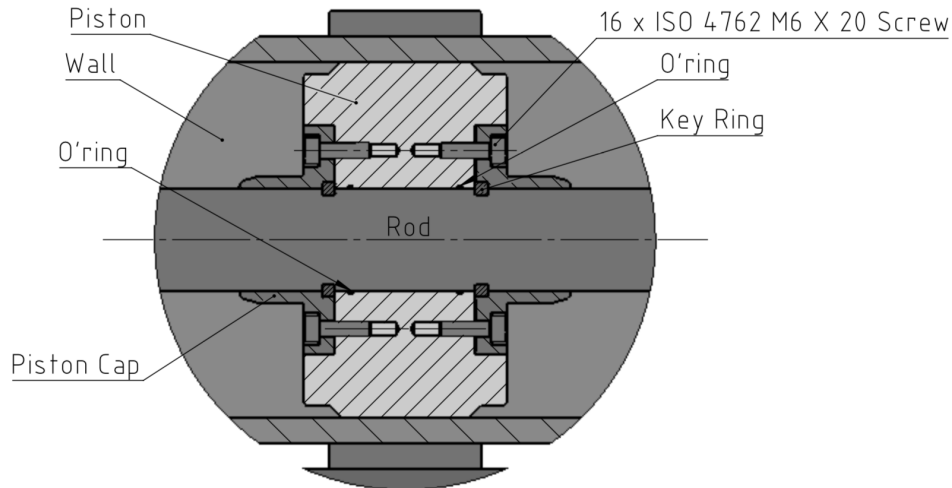


Figure 5.5: Cut view of the Piston.

To assure that the piston is fixed to the rod, it is mounted with four Key Rings, two by each side, as shown in Figure 5.5. Then, to ensure that the parts are fixed together, two Piston Caps, made of Aluminium Alloy 6063-T6, are placed at both ends of the piston, and are fixed with sixteen M8 × 20 screws, eight for each side.

In order to ensure that the piston has high rigidity, while still having the leakage gap with the 50 mm of leakage channel length, as defined in Table 4.3, the piston presents a echeloned cylindrical geometry.

It should be noted that the Piston Cap has a echeloned geometry near the rod. This is made in order to allow a rod seal, which is placed on each head, to fully isolate the cylinder's antechamber during the start of the piston's motion.

### Key Ring

As previously mentioned, the piston is positioned thanks to the Key Rings, shown in Figure 5.6, but also helps transmitting loads between the Piston, the Piston Cap and the Rod. It is, therefore, important to design this element for shear stress and surface pressure. This component's material is steel Ck 45, which has a Tensile Yield Strength,  $\sigma_y$ , of 580 MPa. Therefore, the Shear Yield Strength,  $\tau_y$ , is

$$\tau_y = \frac{\sigma_y}{2} = 290 \text{ MPa} \quad (5.1)$$

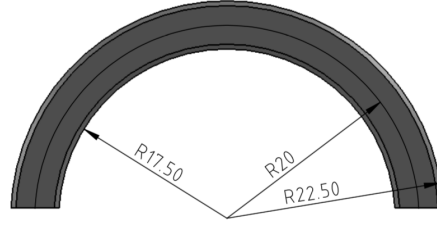


Figure 5.6: Front View of Key Ring.

First of all, the load applied to the Key Rings is, in the worst case scenario, the sum of the resultant force applied to the piston due to chamber pressure and the force exerted by the spring system.

$$\begin{aligned}
 F = F_p + F_{Sp} &= \frac{\pi}{4} (\varnothing_{\text{Piston}}^2 - \varnothing_{\text{Rod}}^2) p + k_{Sp} (l - x_k) = \\
 &= \frac{\pi}{4} (0.14^2 - 0.04^2) 10 \cdot 10^5 + 1.20 \cdot 10^5 \cdot 0.3 \approx 50\,000 \text{ N} \quad (5.2)
 \end{aligned}$$

The shear stress area,  $A_\tau$ , is defined as

$$A_\tau = \varnothing_m \pi h = 0.04 \pi L \quad (5.3)$$

where  $L$  is the length of the Key Ring, and  $\varnothing_m$  is the diameter where the shear stress is applied. Dividing the load considered with the shear stress area, one obtains the shear stress,  $\tau = \frac{F}{A_\tau}$ . Considering the steel's Shear Yield Strength,  $\tau_y$ , one obtains

$$\tau_w \geq \frac{F}{0.04 \pi L} \Leftrightarrow L \geq 2.75 \text{ mm} \quad (5.4)$$

Now the pressure,  $p$ , between the key and the hub (Rod) is calculated

$$p = \frac{F}{\frac{\pi (\varnothing_m^2 - \varnothing_i^2)}{4}} = \frac{50\,000}{\frac{\pi (0.04^2 - 0.035^2)}{4}} \approx 170 \text{ MPa} \quad (5.5)$$

which is inferior to the Tensile Yield Strength.

### 5.2.2 Rod

The actuator's rod, has a diameter of 40 mm, according to the specifications of the Air Bushing, as indicated in Table 5.8. As previously stated, the rod should have the least deflection possible, thus avoiding contact between the piston and the wall. Therefore, in order to maintain rigidity and minimize weight, the rod's material is the Aluminium Alloy 6063-T6.

While no major mechanical dimensioning is required, it is noted that:

- The rod's ends must be screwed, in order to allow any element (like the hook that launches the striker tube) to be connected to the rod, as seen in Figure 5.7a;

- There must be notches in order to place the key rings that fix the piston. This is presented in Figure 5.7b.

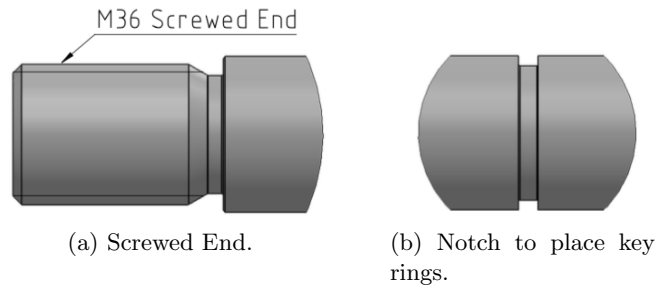


Figure 5.7: Rod Design details.

### 5.2.3 Head

The actuator's head is the most geometrically complex, since it needs to have:

- Pneumatic channels that connect to both chambers and air bushings to the pneumatic circuit. Furthermore, the channels that feed the pneumatic chambers of the actuator need to be sized accordingly to the required air mass flow;
- Exhaust channels that allow leakage air from each chamber and air bushing to easily flow separately to the atmosphere;
- Proper fixtures to the plate, especially considering the loads created by the spring system actuation and the attained pressures inside each chamber.

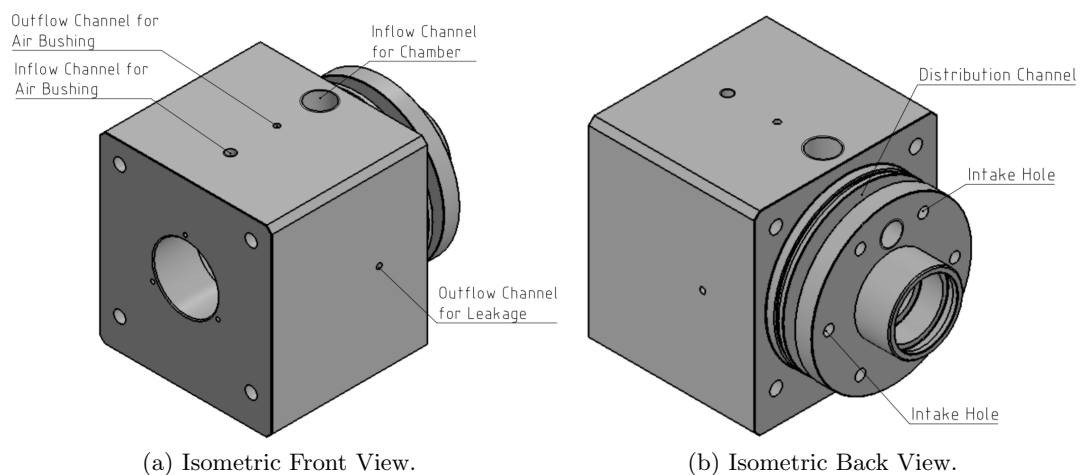


Figure 5.8: Isometric vies of the Head.

Figures 5.8 and 5.9 present some of these characteristics. There is a channel that allows for the supply of the air bearing, and it is positioned in the same axis as the

bushings pressure port. While some air will leave through the head cap, air may also have to leave to the opposite direction. Therefore, an exhaust channel must be made, as seen in Figure 5.8a.

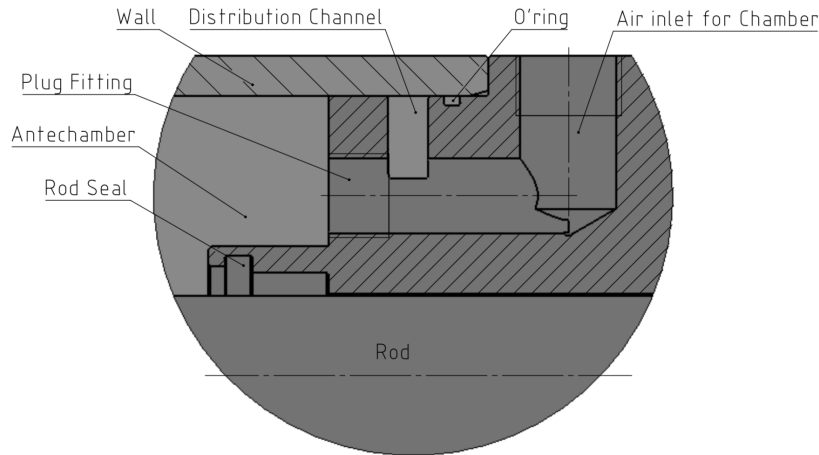


Figure 5.9: Halfway cut of the Head, showing the air bushing and head cap.

Also present is the port that allows the flow of air between the pneumatic valves and the chamber. It is connected to a air distribution channel, visible in Figures 5.8b and 5.9. Air can pass through six intake holes that allow for uniform air distribution to the pneumatic chamber. However, in order to make the flow channels to the chamber, it is necessary to drill a hole that connects directly the chamber's pressure port to the chamber, bypassing the distribution channel and the inflow holes. To avoid this problem, a plug fitting must be placed, sealing this specific passage.

It is noted that here are two outflow channels, on the each side of the head, specifically made to allow air from the rod's leakage gap to exhaust freely. One of these channels is presented in Figure 5.8a. It should be noted that these channels are placed perpendicularly to the air bushing's exhaust channel because of their proximity to each other.

### Screwed Connections

As mentioned, both actuator heads are to be fixed on a plate that will support the machine setup. This will be done using four ISO 4762 M10  $\times$  40, steel material class of 8.8, whose material properties are listed in Table 5.7. These screws will be under tensile loads, as well as bending, given that the loads are eccentric.

Table 5.7: Mechanical properties of Steel material class 8.8.

Tensile Yield Strength, $\sigma_y$ [MPa]	640
Ultimate Tensile Strength, $\sigma_m$ [MPa]	800

As a first analysis of these screws, one must consider the sum of force caused by

pressure  $p$ , and the force of the spring system,  $F_k$ , is equal to the dry friction Force,  $F_f$ , as observed in Figure 5.10. Knowing that, according to Coulomb's Law of Friction, the friction force is proportional to the Normal force,  $F_N$ , and considering that the Normal Force is equally distributed through the four screwed connections, it is then obtained that

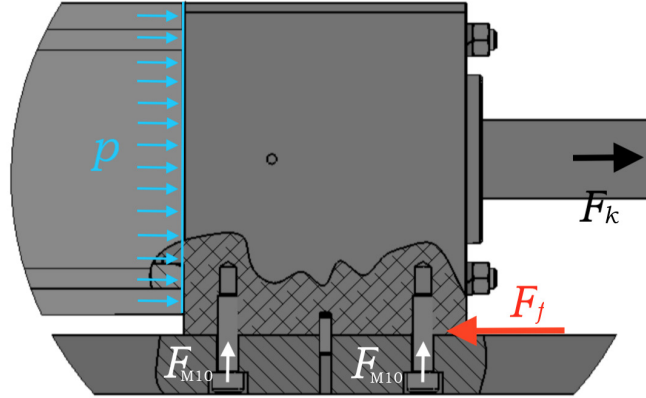


Figure 5.10: Tensile Load on screws.

$$F_{M10} = \frac{F_p + F_k}{4 \bar{\mu}} \quad (5.6)$$

where  $F_{M10}$  is the force that is applied in each M10 screw. The constant  $\bar{\mu}$  is the dry friction coefficient between two Aluminium surfaces, and is equal to 1.05 [36]. Considering that

$$\sigma_{t, M10} = \frac{F_{M10}}{A_{M10}} \quad (5.7)$$

where  $\sigma_{t, M10}$  is the applied tensile stress on the screw, and  $A_{M10}$  is the average cross-section of the screw, and is equal to  $58.1 \text{ mm}^2$  [37]. With equations (5.6) and (5.7), the following is obtained

$$\sigma_{t, M10} = \frac{F_p + F_k}{4 \bar{\mu} A_{M10}} \approx 205 \text{ MPa} \quad (5.8)$$

Now one must study the force applied by the screws, in order to counteract the torque caused by the fact that the sum of the pressure force,  $F_p$ , and the spring force,  $F_k$ . As such, and considering the lengths identified in Figure 5.11, equation (5.9) is obtained after applying the torque equilibrium,

$$(F_p + F_k) h = 4 w F_{M10} \quad (5.9)$$

In the present case,  $w$  is 50 mm, and  $h$  is equal to 90 mm. Using equation (5.7) and the



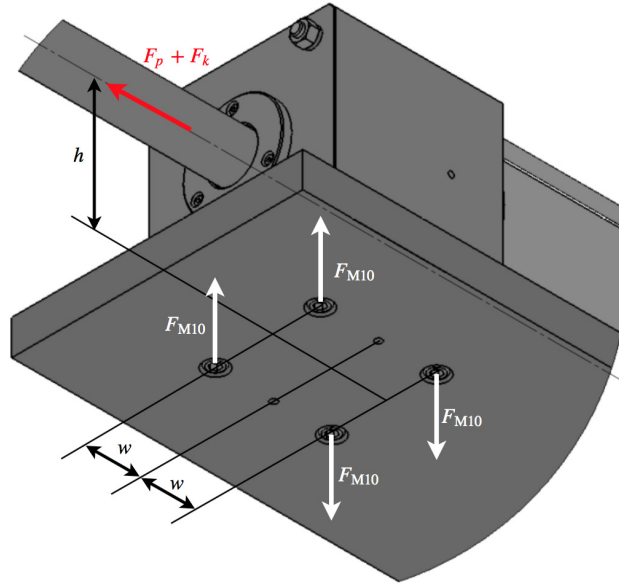


Figure 5.11: Bending Load on screws.

aforementioned dimensions, yields

$$\sigma_{b, M10} = \frac{(F_p + F_k) h}{4 w A_{M10}} \approx 388 \text{ MPa} \quad (5.10)$$

where  $\sigma_{b, M10}$  is the stress caused by this bending effect. It is noted that both values tensile stress are well below the Tensile Yield Strength of the screw's material.

It is noted that, two dowel pins have also been placed in both heads, for orientation purposes.

### Air Bushing

As discussed in Chapter 4, the actuator's rods should not have physical contact with the cylinder heads, in order to minimize any friction during the rod's motion. This means that no rod seals should be used. However, the rods must be supported. In this manner, a research of the various types of bearings and bushings was made in order to determine the best alternative.

The adopted solution consists of air bushings able to support the rods. Figure 5.12 presents the selected bearing, which is a bushing model OAV040MB manufactured by OAV<sup>®</sup> Air Bearings. This bearing has a core made of graphite, where a rod passes through it. Table 5.8 lists the bushing's specifications.

These bushings can be placed on a mounting block, or on a specially designed component, such as the head of the cylinder. There are three installation methods:

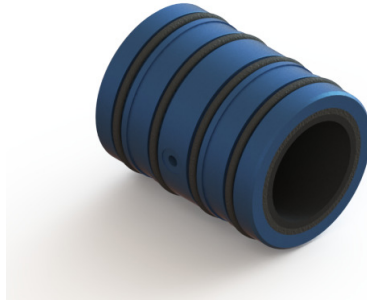


Figure 5.12: Model of the air bushing OAV040MB [38].

Table 5.8: OAV<sup>®</sup> bushing model OAV040MB specifications [38].

Input pressure [bar]	2.8 to 6.8
Radial Load [N]	866.3
Radial stiffness [N m <sup>-1</sup> ]	$72 \cdot 10^6$
Maximum Pitch Moment [N m]	3.1
Flow Rate [slpm]	$11.10 \cdot 10^{-3}$
Mass [g]	249.1
Inside Diameter [mm]	$40.018^{+0.005}_0$
Outside Diameter [mm]	$59.59^{+0.13}_0$
Length [mm]	76.2
Recommended shaft outside diameter [mm]	40g6
Pressure Port Thread	M5 × 0.8

- O’rings can be used, but they must be selected according to the bore’s dimensions and tolerances;
- The brushing can be placed with a light press, but bore’s dimensions and tolerances must also be considered;
- Epoxy can be injected with a syringe, but o’rings are still required and the mounting component needs to have special holes for syringe access.

It was decided that the bearing should be placed with o’rings, since it is the simplest of the three methods, and enables the mounting hole to be sealed.

### Head Cap

The head cap is a simple component, whose function is to fix the air bushing inside the cylinder’s head, while allowing the rod to pass through. This element is not subject to any particular load and, therefore, it is made of Aluminium Alloy 6063-T6. This cap is fixed using three ISO 4762 M4 × 10 screw, as seen in Figure 5.13.

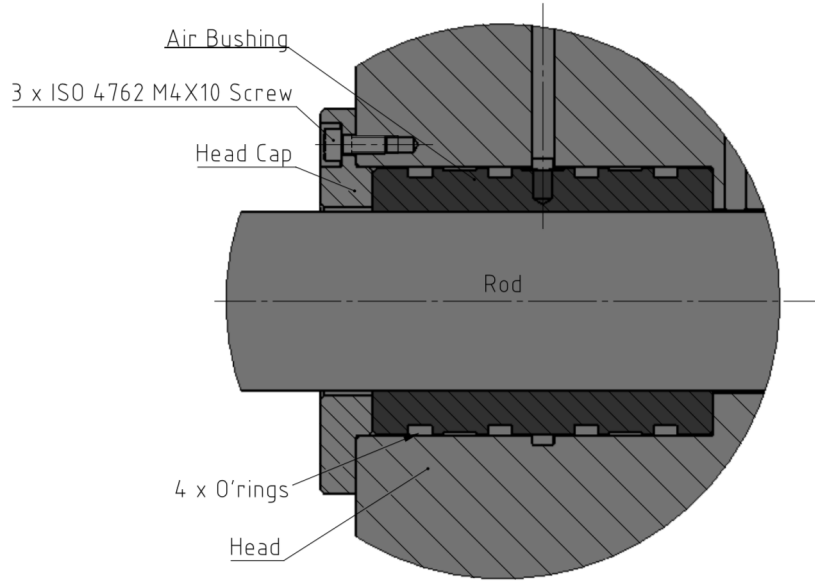


Figure 5.13: Halfway cut of the Head, showing the air bushing and head cap.

### Tie Rods

The tie rods maintain the cylinder heads and body fixed between each other, guaranteeing pressure acting on a chamber does not force it to open. As such, this component must sustain high stresses. Therefore, the tie rod's material is Stainless Steel AISI 304, and its mechanical properties are presented in Table 5.9.

Table 5.9: Mechanical properties of Stainless Steel AISI 304 [39].

Tensile Yield Strength, $\sigma_y$ [MPa]	180
Ultimate Tensile Strength, $\sigma_m$ [MPa]	460 - 680
Elasticity Modulus, $E$ [GPa]	200

Since these elements are subject to the pressure force,  $F_p$ , and considering that the pressure acting on a chamber is of 10 bar, then one obtains

$$F_p = \frac{\pi}{4} (\varnothing_{\text{Piston}}^2 - \varnothing_{\text{Rod}}^2) p \approx 14\,200 \text{ N} \quad (5.11)$$

This resultant force is distributed between the four tie rods. Given that each tie rod has a diameter of 10 mm, the resultant stress,  $\sigma$ , can be calculated as

$$\sigma = \frac{F_p}{4 A_{\text{textTR}}} = \frac{14\,200}{4 \frac{\pi 0.010^2}{4}} \approx 45 \text{ MPa} \quad (5.12)$$

which is well below the materials elasticity limits.

### 5.2.4 Seals and O’rings

As previously described, o’rings and Rod Seals must be placed in the assembly. O’rings are essential since they guarantee sealing in static conditions, and should be placed:

- In the air bushings, as seen in Figures 5.12 and 5.13. These o’rings are specifically designed for the air bushing, and are sold with the bearing;
- In each cylinder head, as seen in Figure 5.9, to remove the possibility of air leaking to the atmosphere through gaps between the head and the cylinder wall;
- In the piston, as seen in Figure 5.5, to avoid uncontrolled air leakage between both chambers, through crevices between the rod and the piston.

In this manner, o’rings must be selected. Table 5.10 lists the selected o’rings and Figure 5.14a presents the main o’ring dimensions.

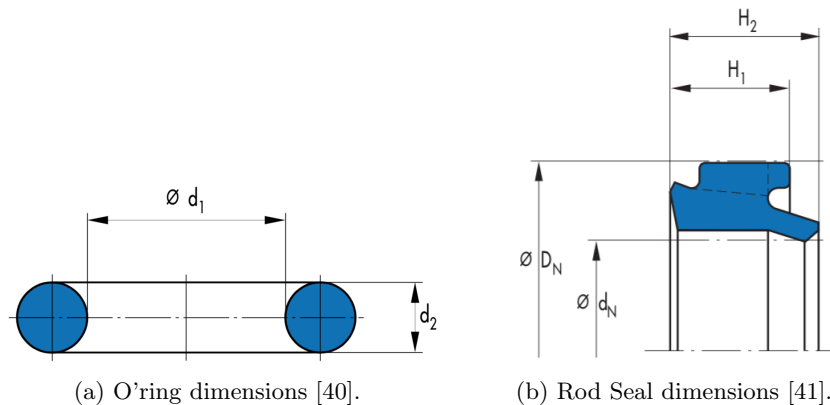


Figure 5.14: Dimensions of sealing elements.

Table 5.10: O’ring specifications [40].

Reference	445 642	14 452 149
$\varnothing d_1$ [mm]	40.00	137.00
$d_2$ [mm]	1.50	3.00
Material	72 NBR 872	72 NBR 872
Placement indicated in	Figure 5.5	Figure 5.9

A Rod Seal also has to be selected in order to seal the rod leakage channel from the pneumatic antechamber, in order to minimize leakage during at the start of the piston’s motion. Therefore, the Merkel Damper Seal AU DIP, manufactured by Simrit, is selected. Table 5.11, presents the main specifications of the seal and Figure 5.14b identifies the seal’s dimensions.

Table 5.11: Rod Seal specifications [41].

Reference	425 523
$\varnothing d_N$ [mm]	50
$\varnothing D_N$ [mm]	60
$H_1$ [mm]	6.2
$H_2$ [mm]	8
Material	High performance polyurethane
Material Code	94 AU 925
Hardness (Shore A)	94
Operating Pressure [bar]	$\leq 25$
Running Speed [ $m s^{-1}$ ]	$\leq 1$

### 5.2.5 Cylinder Wall

The cylinder wall is one of the most important structural elements of the actuator. It needs to sustain the pressures required for the actuator to work under normal conditions without observing any significant displacements. Therefore, the material adopted for the cylinder walls is the cold drawn Steel Alloy St 52.3, with an outside diameter,  $\varnothing_e$ , of 160 mm, and a diameter,  $\varnothing_i$ , of 140 mm. Table 5.12 lists the mechanical properties of the material when the wall thickness is under 16 mm.

Table 5.12: Mechanical properties of Steel Alloy St 52.3 [42].

Tensile Yield Strength, $\sigma_y$ [MPa]	520
Ultimate Tensile Strength, $\sigma_m$ [MPa]	600
Elongation [% min.]	14

Since the operating pressure range of the cylinder should be under 10 bar, no major elongation is expected.

### 5.2.6 Mid Support

One of the requirements for the design of the pneumatic actuator is to minimize the deflection of the rods/piston. However, the cylinder wall are also subject to the same issue. Unlike the rods, the cylinder wall is not subject to constructive restrictions and, therefore, it can also be fixed in the middle. Figure 5.15 presents the adopted solution.

This solution is composed of half shaped mid supports, made of Aluminium Alloy 6063-T6. These are connected to each other thanks to two  $M10 \times 60$  screws and the lower mid support is connected to the support plate with two  $M10 \times 40$ , which are also used in the heads.

### 5.2.7 Structural Simulations

The last step in validating the actuator design is to run a design of the assembly through static studies in *SolidWorks*, in order to verify its structural integrity, as well as the resultant deflection of the rod/piston. These studies are focussed on the most

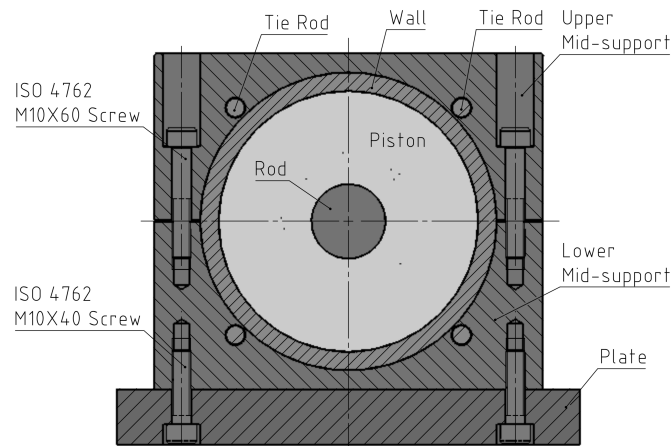


Figure 5.15: Cut view of the mid support sub assembly.

important structural and functional elements of the assembly and do not include normalized components. Also due to the software limitations, it is impossible to implement a simulation of the air busing and its effect on the rod.

These simulations are made considering that the piston is mid-stroke and that there is pressure in both chambers. In light of this, it is considered that the rods are fixed where the air bushings support it. It is also considered that both actuator heads and the mid support is fixed. Figure 5.16 shows the stress distribution in the various elements, while Figure 5.17 presents the resultant deflection in the vertical direction ( $y$  axis).

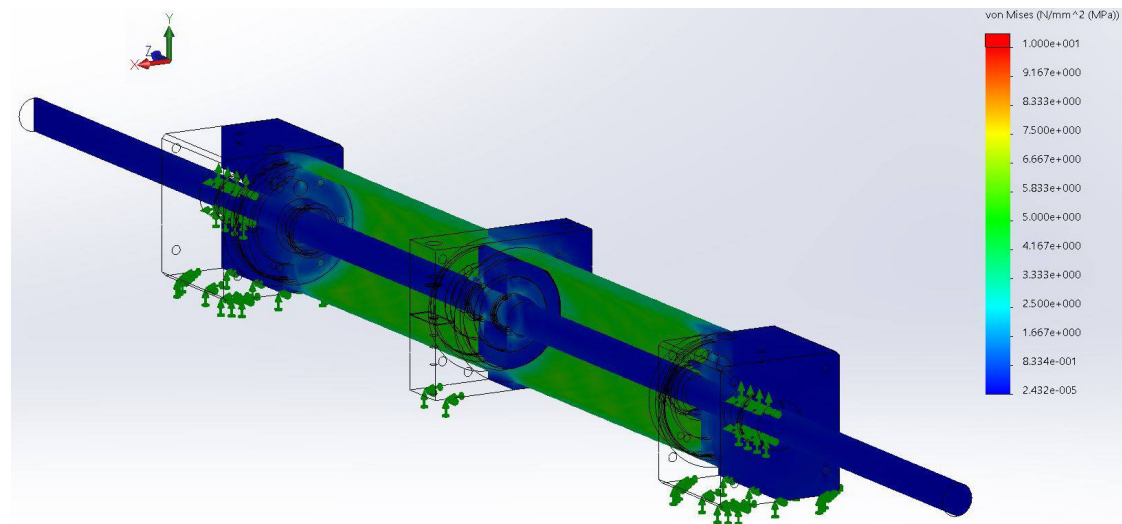


Figure 5.16: Stress distribution on the various elements of the actuator assembly.

It can be seen that the stress distribution of the various elements is quite low,

where the highest stress value observed is on the cylinder wall, where stress values of up to 6 MPa are obtained. This stress value is significantly lower than that of the steel's Tensile Yield Strength, presented in Table 5.12.

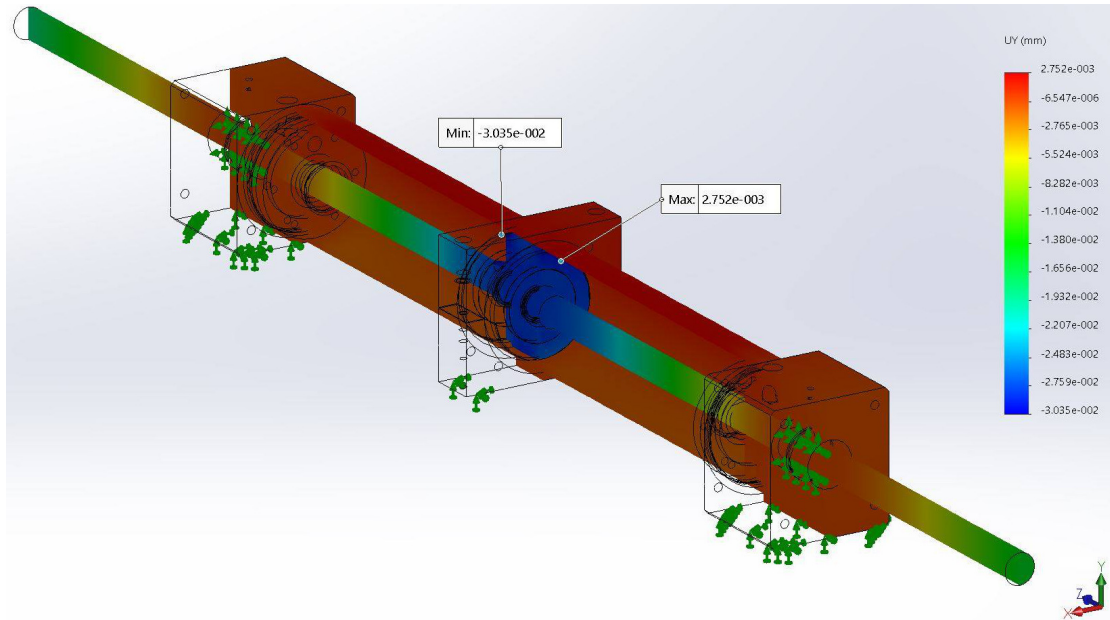


Figure 5.17: Deflection of the various elements of the actuator in the vertical direction ( $y$  axis).

When analyzing the deflection in the vertical direction, one can see that the obtained values are quite low. The piston's deflection is the highest of the assembly, reaching values of approximately 0.03 mm. However this is only 10 % of the difference between piston and cylinder wall's diameter, as seen from the presented values in Table 4.3. In other words, the observed deflection is low enough to consider that the leakage channel is circular, as first assumed in the functional simulations.

With the structural simulations complete, the mechanical design of the actuator is concluded.





## Chapter 6

# Conclusions and Future Works

This chapter presents the main conclusions of this thesis, highlights the achieved objectives, and proposes future works that may be developed in the continuation of this project.

### 6.1 Conclusions

In the beginning, a review of the mechanics of wave propagation, reflection and transmission through solid media was presented, in order to better understand the physical phenomena. Afterwards, simplified mathematical models of the mechanical behaviour of the SHPB setup and the energetic behaviour of the specimen deformation were studied. Several Kolsky Bar Tensile machine architectures were also discussed, as well as some design requirements and recommendations found in the literature.

In order to determine the proper geometries for the bars and the specimen, a study of the requirements was fulfilled. The models presented in Chapter 2 were tackled to evaluate the range of the striker bar velocities and lengths. A comparison of the stiffnesses and wave impedances between the bars and several specimen was also included. Afterwards, the obtained results were extensively analyzed and discussed. Based on these results, several conclusions were put forth as to:

- Which specimen can be used for impact testing, and their geometries;
- The dimensions of the bars in the SHPB setup;
- The proposed SHPB architecture and actuation system to be implemented.

In the proposed Kolsky Bar setup, a non-conventional pneumatic actuator, that can attain high velocities, was proposed. However, the actuator architecture needed to be simulated, as it needed to be functionally validated. As such, functional simulations were made, with mathematical models that describe the dynamic behaviours of the pneumatic circuit and the actuator. Results show that the actuator can attain the high

velocities required to launch the striker bar/tube.

With this, the elements present in the pneumatic circuit were selected. Lastly, the mechanical design of the actuator was made. Structural simulations were performed in order to verify and validate the design and demonstrate that good mechanical behaviour is achieved.

It is noted that the proposed SHPB setup is novel and innovative and, as such, a patent proposal was submitted to "UP Inovação", which can be seen in Appendix C.

## 6.2 Future Works

During the period of this thesis, several ideas emerged that could not be implemented due to time constraints. Also, some results show that further study of several details is recommendable for the progress and completeness of this project.

In chapter 3, when studying the results obtained with the mathematical models, namely for the dynamical behaviour of the SHPB machine, as presented, it was found that the designed bars are optimal for both Bulk Specimen (BS) and Bonded Joint Specimen (BJS) with rigid adhesives. In contrast, the stiffness and wave impedance of BS and BJS with flexible/soft adhesives are orders of magnitude lower than those of the bars. This is quite common for the characterization of soft materials under impact conditions [3]. This poses several problems on the design of the specimen and of the pressure bars ideal to test such materials. Therefore, it is advised to further study:

- The various Kolsky Bar setups that are able to characterize soft materials;
- The design of specially made specimen that are immune to radial and axial inertia effects;
- The adoption of special sensitive instrumentation measuring system that is able to measure low amplitude stress waves.

The functional simulations that were made have shown that the actuator has a good performance, attaining the required high velocities. However, further simulations need to be made in order to:

- Determine the velocity range that the rod/piston can attain versus the initial pressure inside the pneumatic chambers;
- Determine the positions that the rod stops, after hitting the springs, versus the initial position, as well as the position where the shock absorbers start acting on the rod, slowing it down.

Although the mechanical design of the actuator is complete, it is only a subsystem of the whole machine and requires the design of several other subsystems such as:

- The braking system composed of the springs and shock absorbers;

- The machine pressure bars and launching apparatus, like, for example, the impact flange and hook for tensile testing, among other;
- The mechanical structure that will support the pressure bars and the actuator.

It is also recommended that the initial chamber pressure to launch the striking element should be established using a proportional pressure regulating valve that is controlled by a computer software. It should be noted that this system would only act to control the initial pressure of the launching sequence.

Lastly, a selection of the wave measuring instrumentation needs to be made, as well as a computer software that controls the machine according to user commands, that displays the measured waves and that determines the mechanical properties and behaviour of adhesives under impact conditions.



# Bibliography

- [1] W. Brockmann, P. L. Geiß, J. Klingen, and B. Schröder, *Adhesive Bonding: Materials, Applications and Technologies*. Weinheim, Germany: Wiley-VCH, 1 ed., 2009.
- [2] L. da Silva, A. Öchsner, and R. Adams, *Handbook of Adhesion Technology*. Berlin, Germany: Springer-Verlag, 1 ed., 2011.
- [3] W. Cheng and B. Song, *Split Hopkinson (Kolsky) Bar: Design, Testing and Applications*. New York, New York, United States of America: Springer, 1 ed., 2011.
- [4] S. Sharma, V. Chavan, R. Agrawal, R. Patel, R. Kapoor, and J. Chakravartty, *Split-Hopkinson Pressure Bar: an experimental technique for high strain rate tests*. Mumbai, India: Department of Atomic Energy, Government of India, 2011.
- [5] D. R. R. de Sousa, “Development of the automation framework and rebound-capture system for a drop-weight test machine,” Master’s thesis, Faculdade de Engenharia da Universidade do Porto, Porto, Portugal, June 2017.
- [6] J. L. Lataillade, D. Grapotte, and F. Cayssials, “The impact resistance of CTBN-modified epoxy adhesive joints,” *Journal de Physique IV*, vol. 4, pp. 88–96, September 1994.
- [7] W. F. Smith, *Principles of Materials Science and Engineering*. Singapore, Singapore: McGraw-Hill, 2 ed., 1990.
- [8] E. Kreyszig, *Advanced Engineering Mathematics*. Hoboken, New Jersey, United States of America: John Wiley & Sons, 10 ed., 2011.
- [9] E. Weisstein, “d’Alembert Solution.” <http://mathworld.wolfram.com/dAlembertsSolution.html>, Consulted on the 19<sup>th</sup> February 2018.
- [10] K. F. Graff, *Wave Motion in Elastic Solids*. London, United Kingdom: Oxford University Press, 1 ed., 1975.
- [11] F. J. Ferreira, *Análise do Comportamento Dinâmico de Componentes Estruturais sob Solicitações Generalizadas*. PhD thesis, Faculdade of Engenharia da Universidade do Porto, May 2003.

- [12] J. Harding, E. . Wood, and J. D. Campbell, “Tensile testing of materials at impact rates of strain,” *Journal Mechanical Engineering Science*, vol. 2, no. 2, pp. 771–776, 1960.
- [13] U. S. Lincoln and L. M. Yeakley, “High strain-rate testing: Tension and compression,” *Experimental Mechanics*, vol. 8, pp. 1–9, January 1968.
- [14] T. Nicholas, “Tensile testing of materials at high rates of strain,” *Experimental Mechanics*, vol. 21, pp. 177–185, May 1981.
- [15] S. Nemat-Nasser, J. B. Isaacs, and J. E. Starrett, “Hopkinson techniques for dynamic recovery experiments,” *Proceedings: Mathematical and Physical Sciences*, vol. 435, pp. 371–391, November 1991.
- [16] R. Gerlach, C. Kettenbeil, and N. Petrinic, “A new split Hopkinson tensile bar design,” *International Journal of Impact Engineering*, vol. 50, pp. 63–67, December 2012.
- [17] P. Follansbee, P. Armstrong, J. Hockett, G. Dudder, and D. Erlich, “High strain rate compression testing,” *ASM Handbook*, vol. 8, pp. 190–207, 1985.
- [18] L. F. M. da Silva, D. A. Dillard, B. R. K. Blackman, and R. D. Adams, *Testing Adhesive Joints - Best Practices*. Weinheim, Germany: Wiley-VCH, 1 ed., 2012.
- [19] W. D. Callister, Jr., *Materials Science and Engineering, an Introduction*. New York, New York, United States of America: John Wiley & Sons, 7 ed., 2007.
- [20] F. J. P. Chaves, L. F. M. da Silva, M. F. S. F. da Sousa, D. A. Dillard, and V. H. C. Esteves, “Fracture mechanics tests in adhesively bonded joints: A litterature review,” *The Journal of Adhesion*, vol. 90, no. 12, pp. 955–992, 2014.
- [21] M. C. Maurício, “Dynamic analysis of structures with viscoelastic damping treatments: Complex modulus identification and transient response,” Master’s thesis, Faculdade de Engenharia da Universidade do Porto, Porto, Portugal, June 2017.
- [22] J. F. S. Gomes, *Mecânica dos Sólidos e Resistência dos Materiais*. Porto, Portugal: Edições INEGI, 1 ed., 2004.
- [23] “ISO 6358:1989 - Pneumatic fluid power - Components using compressible fluids - Determination of flow-rate characteristics,” standard, International Organization for Standardization, Geneva, CH, 1989.
- [24] F. M. White, *Fluid Mechanics*. New York, New York, United States of America: McGraw-Hill, 7 ed., 2011.
- [25] J. F. Carneiro and F. G. de Almeida, “Reduced-order thermodynamic models for servo-pneumatic actuator chambers,” *Proceedings of the Institution of Mechanical Engineers, Part I: Journal of Systems and Control Engineering*, vol. 220, pp. 301–314, June 2006.

- [26] X. Brum, *Commandes linéaires et non linéaires en électropneumatique. Méthodologies et Applications*. PhD thesis, Institut National des Sciences Appliquées de Lyon, December 1999.
- [27] L. C. F. Moreira, “Caracterização experimental de um atuador pneumático de baixo atrito,” Master’s thesis, Faculdade de Engenharia da Universidade do Porto, Porto, Portugal, July 2012.
- [28] T. L. Bergman, A. S. Lavine, F. P. Incropera, and D. P. Dewitt, *Fundamentals of Heat and Mass Transfer*. Hoboken, New Jersey, United States of America: John Wiley & Sons, 7 ed., 2011.
- [29] ACE - Automation Control Equipment, “Damping Technology - Main Catalogue,” 2017.
- [30] Amtrol-Alfa, “Refrigerant - Innovation Is Cool.”
- [31] SMC, “Modular F.R.L. Unit - Series AC.”
- [32] SMC, “Regulator with Built-in Pressure Gauge - Filter Regulator with Built-in Pressure Gauge - Series ACG/ARG/AWG.”
- [33] SMC, “3 Port Solenoid Valve - Series VP 300/500/700.”
- [34] SMC, “Quick Exhaust Valve - Series AQ.”
- [35] SMC, “Check Valves INA-14 and XTO-674.”
- [36] E. A. Avallone, T. B. III, and A. M. Sadegh, *Mark’s Standard Handbook for Mechanical Engineers*. New York, New York, United States of America: McGraw-Hill, 8 ed., 1978.
- [37] S. Morais, *Desenho Técnico Básico*. Porto, Portugal: Porto Editora, 25 ed., 2012.
- [38] OAV Air Bearings, “Product Book & Design Guide.”
- [39] C. Wegst and M. Wegst, “Stahlschlüssel - Key of Steel,” 2004.
- [40] Simrit, “O-Rings and Static Seals,” 2007.
- [41] Simrit, “Seals for Fluid Power,” 2007.
- [42] Teclena, “Aços para Cilindros Hidráulicos e Tubagens.”

## Bibliography

---



# Appendix A

## Machine Characterization

In this appendix, a showcase of additional results obtained for Stainless Steel Bars, Aluminium Alloy Bars and Titanium Alloy Bars is presented, for the models described in section 3.2.

### A.1 Steel Bars

#### Striker Bar Velocity

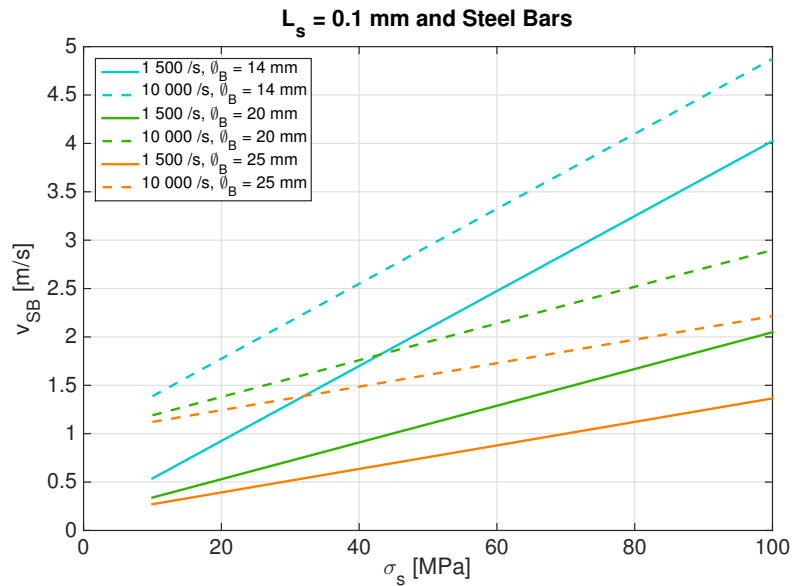


Figure A.1: Striker bar velocity required for Stainless Steel bars and specimen of length  $L_s = 0.1$  mm

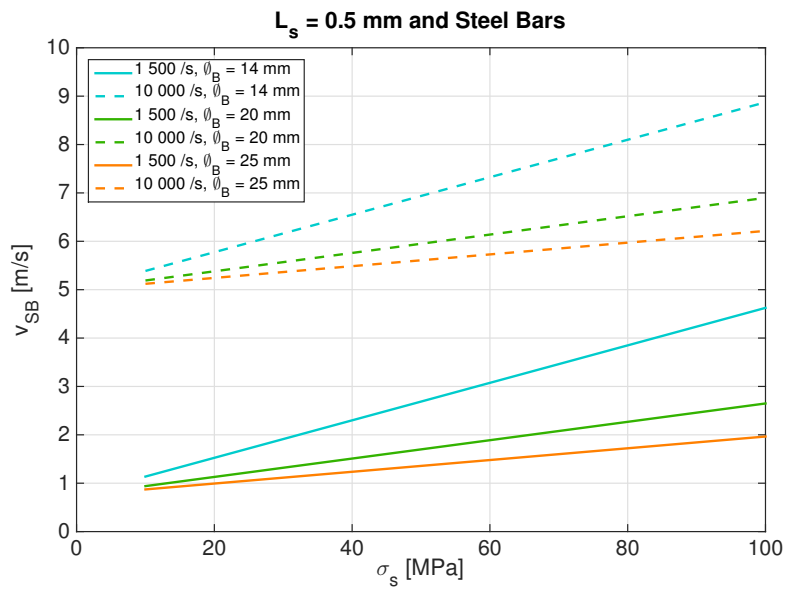


Figure A.2: Striker bar velocity required for Stainless Steel bars and specimen of length  $L_s = 0.5$  mm.

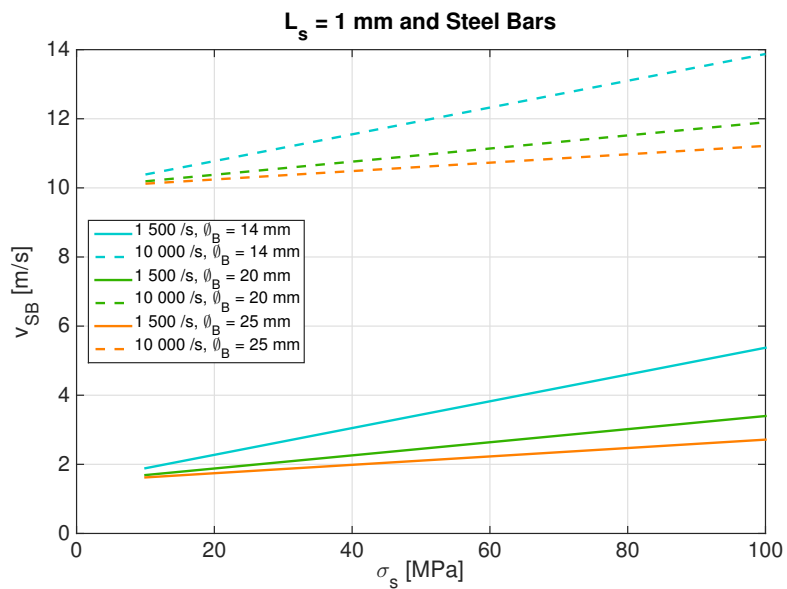


Figure A.3: Striker bar velocity required for Stainless Steel bars and specimen of length  $L_s = 1$  mm.

## A.2 Aluminium Alloy Bars

### Striker Bar Velocity

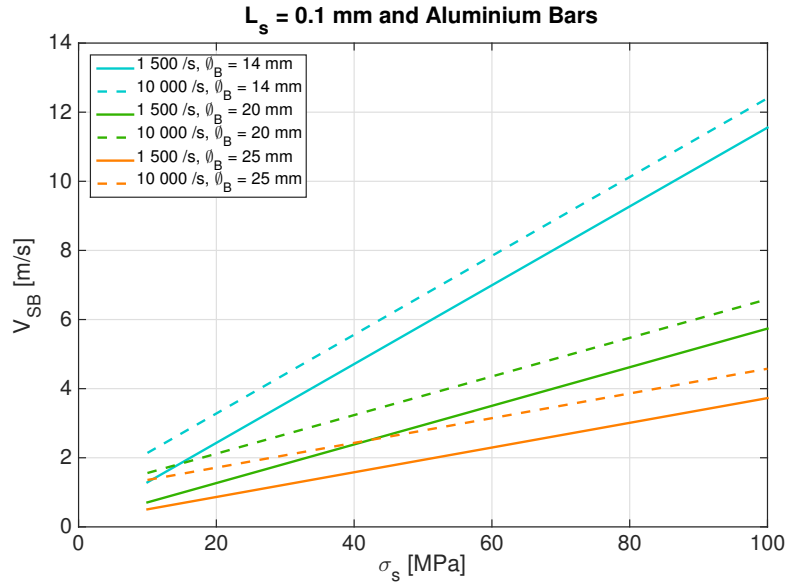


Figure A.4: Striker bar velocity required for Aluminium Alloy bars and specimen of length  $L_s = 0.1$  mm.

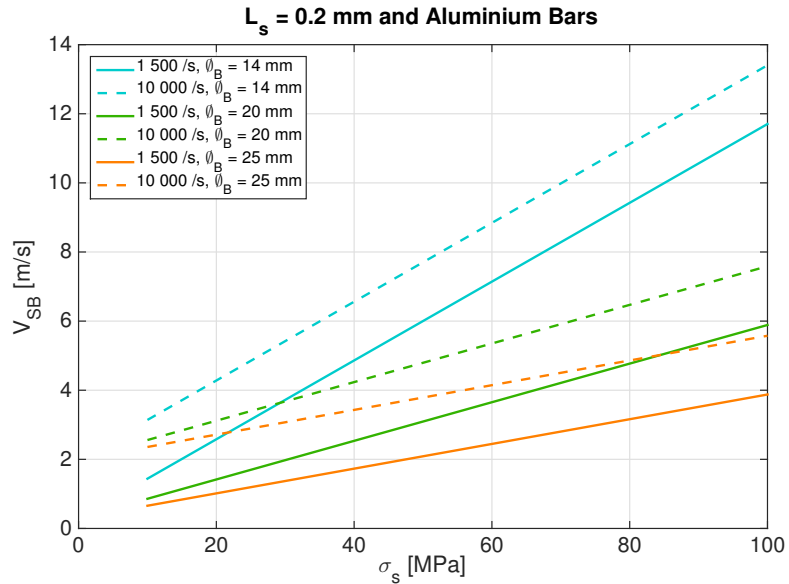


Figure A.5: Striker bar velocity required for Aluminium Alloy bars and specimen of length  $L_s = 0.2$  mm.

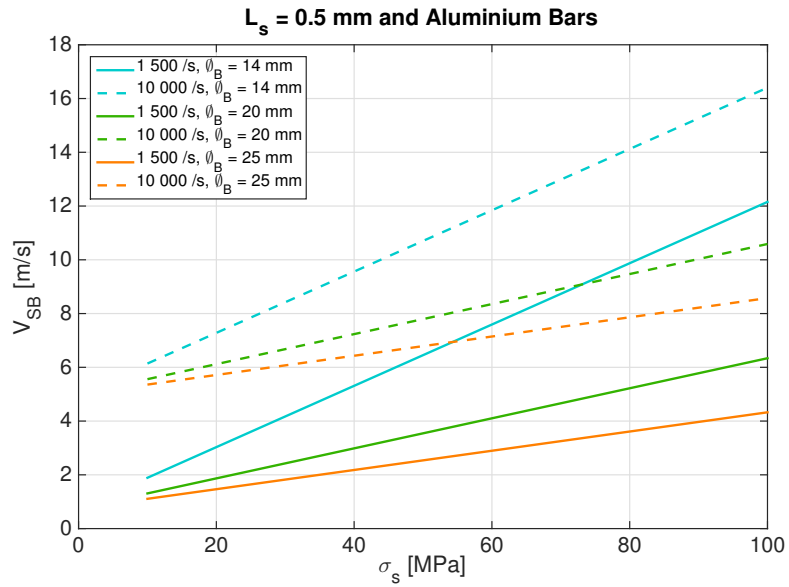


Figure A.6: Striker bar velocity required for Aluminium Alloy bars and specimen of length  $L_s = 0.5$  mm.

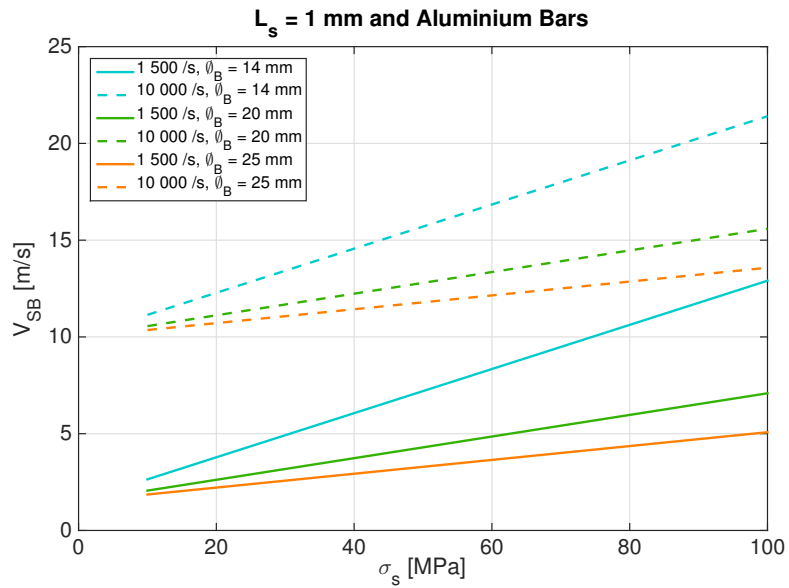


Figure A.7: Striker bar velocity required for Aluminium Alloy bars and specimen of length  $L_s = 1$  mm.

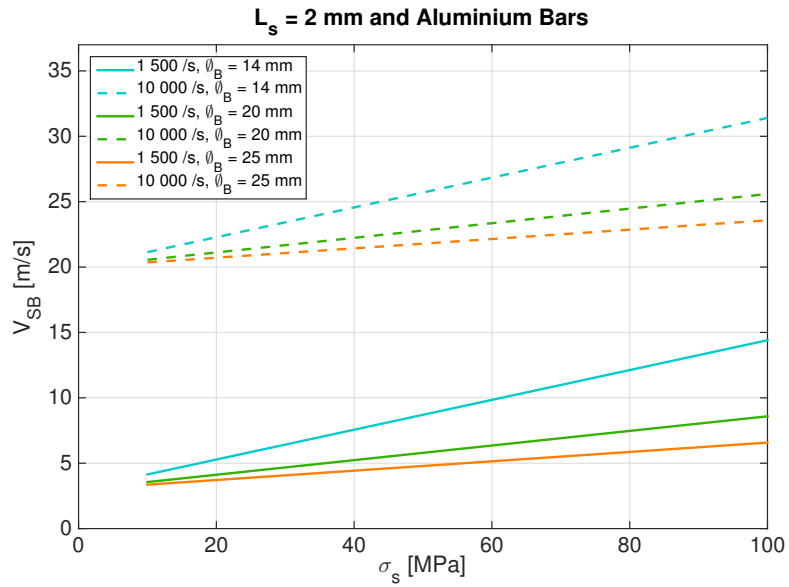


Figure A.8: Striker bar velocity required for Aluminium Alloy bars and specimen of length  $L_s = 2$  mm.

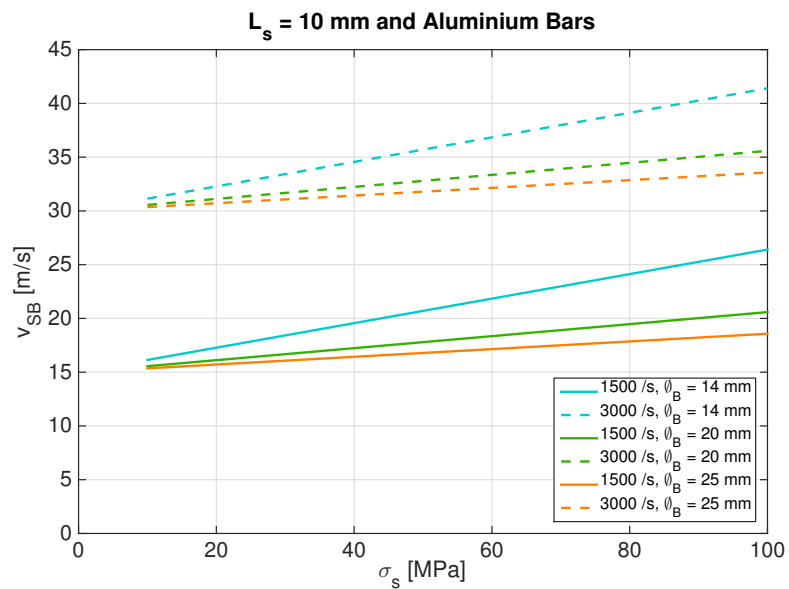


Figure A.9: Striker bar velocity required for Aluminium Alloy bars and specimen of length  $L_s = 10$  mm.

### Impedance & Stiffness Ratios

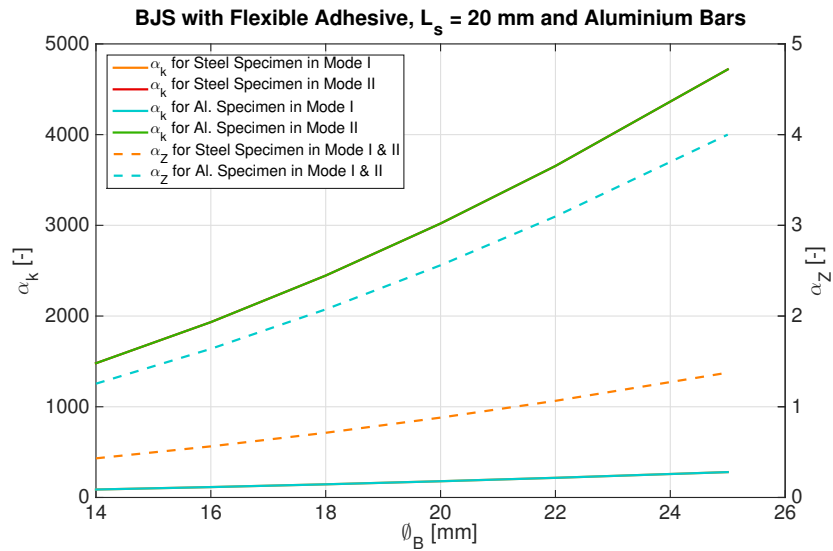


Figure A.10: Ratio comparison for BJS of 20 mm length, with flexible adhesives and Aluminium Alloy bars.

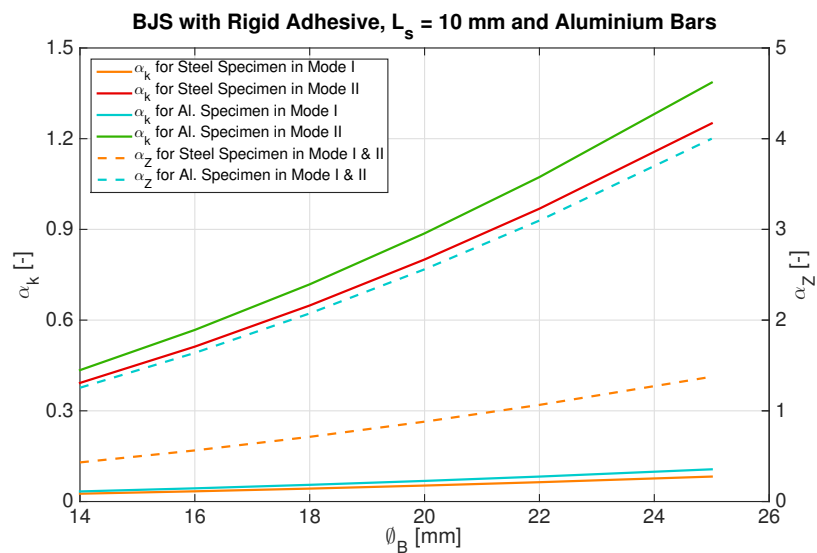


Figure A.11: Ratio comparison for BJS of 10 mm length, with rigid adhesives and Aluminium Alloy bars.

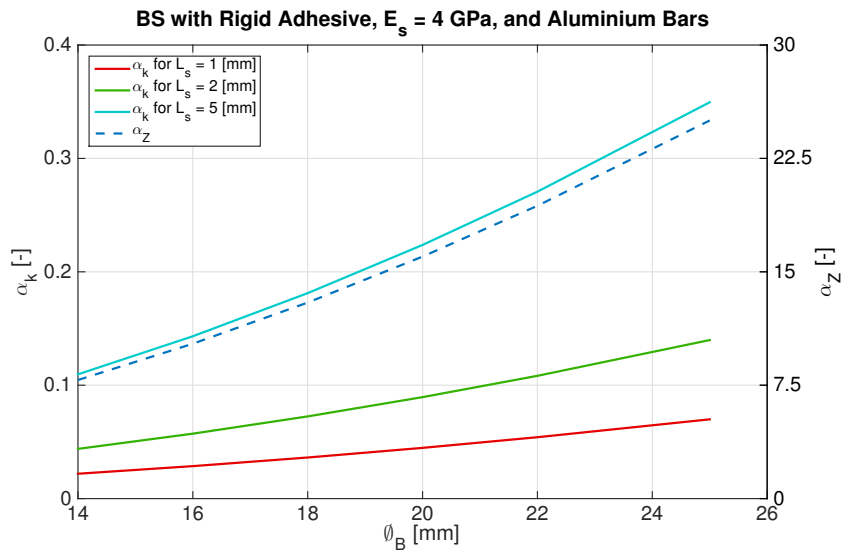


Figure A.12: Ratio comparison for BS, with rigid Adhesives and Aluminium Alloy bars.

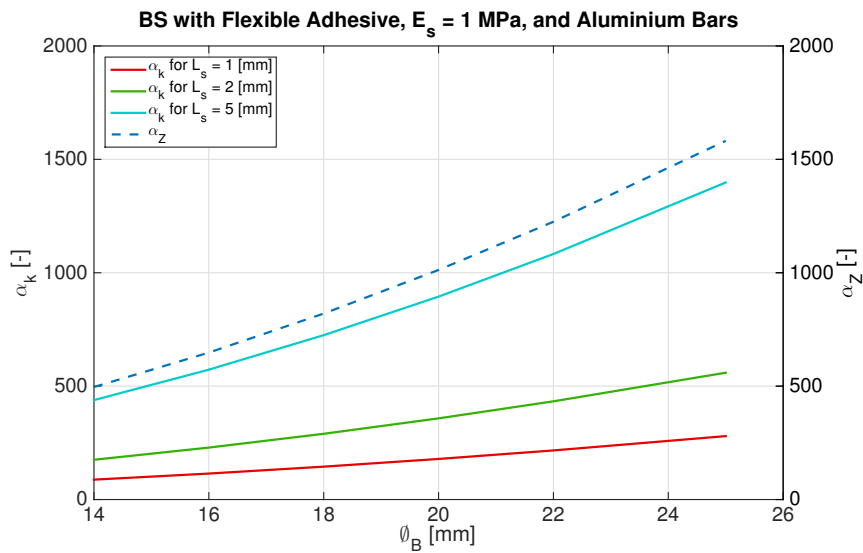


Figure A.13: Ratio comparison for BS, with flexible adhesives and Aluminium Alloy bars.

### A.3 Titanium Alloy Bars

#### Striker Bar Velocity

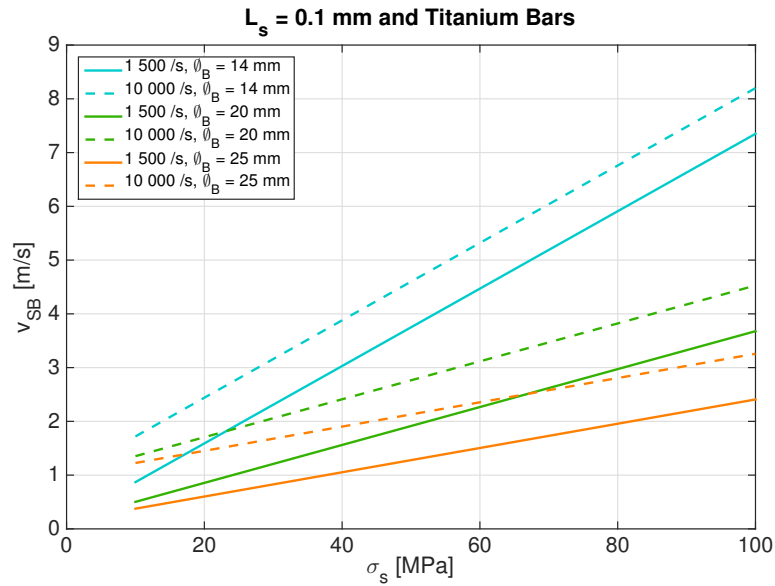


Figure A.14: Striker bar velocity required for Titanium Alloy bars and specimen of length  $L_s = 0.1$  mm.

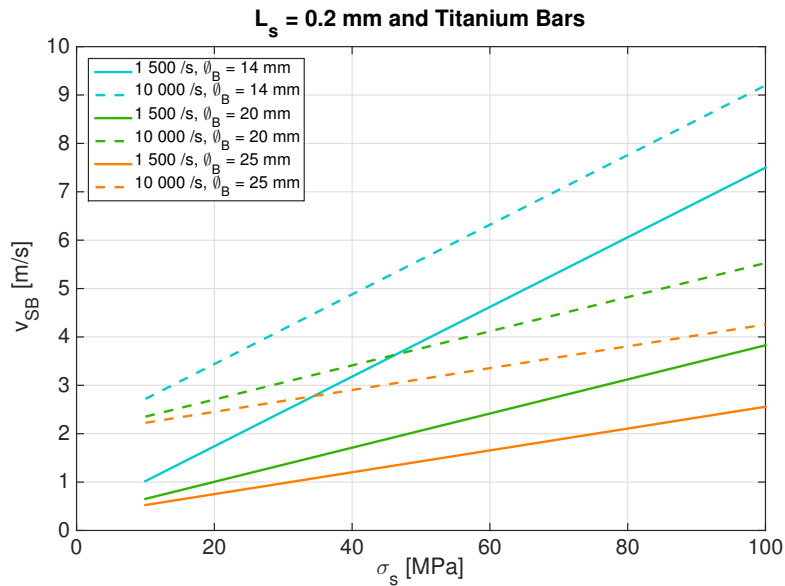


Figure A.15: Striker bar velocity required for Titanium Alloy bars and specimen of length  $L_s = 0.2$  mm.



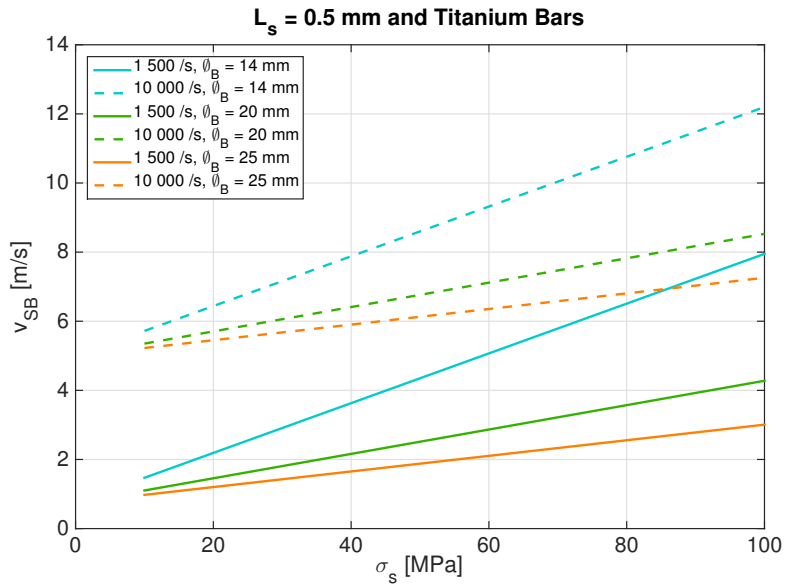


Figure A.16: Striker bar velocity required for Titanium Alloy bars and specimen of length  $L_s = 0.5$  mm.

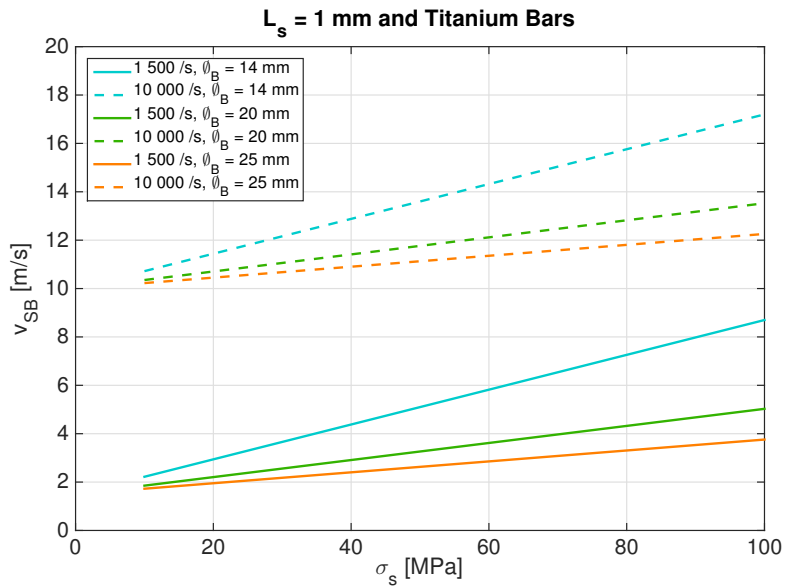


Figure A.17: Striker bar velocity required for Titanium Alloy bars and specimen of length  $L_s = 1$  mm.

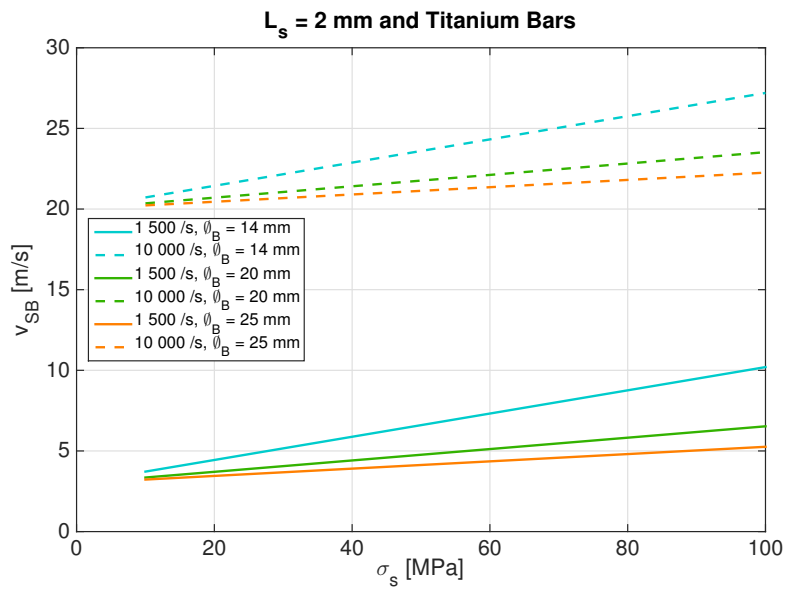


Figure A.18: Striker bar velocity required for Titanium Alloy bars and specimen of length  $L_s = 2$  mm.

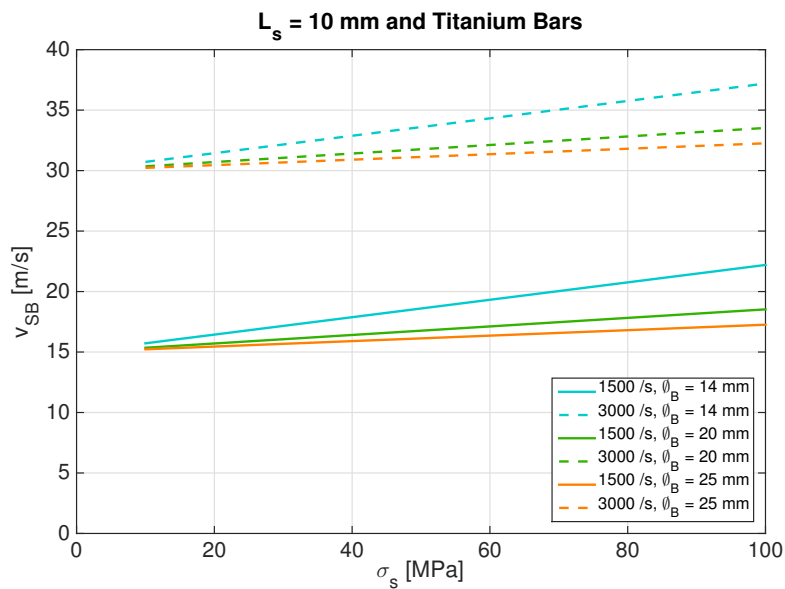


Figure A.19: Striker bar velocity required for Titanium Alloy bars and specimen of length  $L_s = 10$  mm.

Impedance & Stiffness Ratios

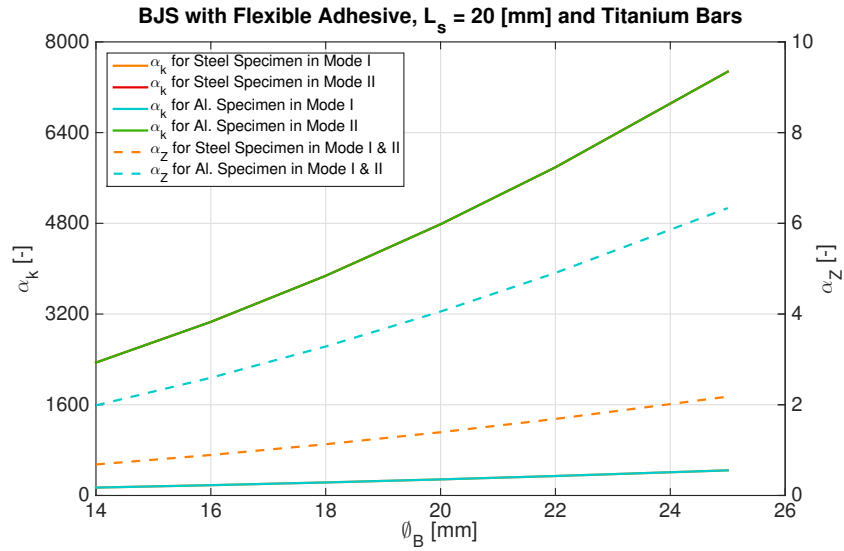


Figure A.20: Ratio comparison for BJS of 20 mm length, with flexible adhesives and Titanium Alloy bars.

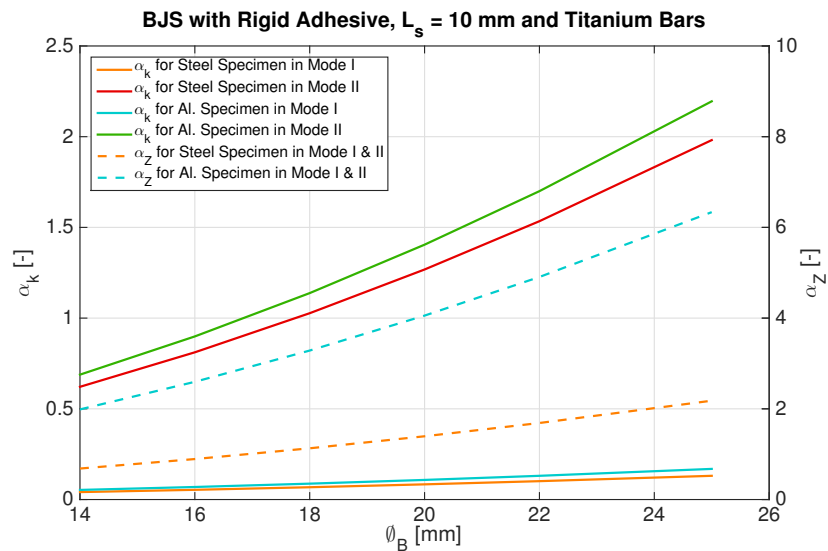


Figure A.21: Ratio comparison for BJS of 10 mm length, with rigid adhesives and Titanium Alloy bars.

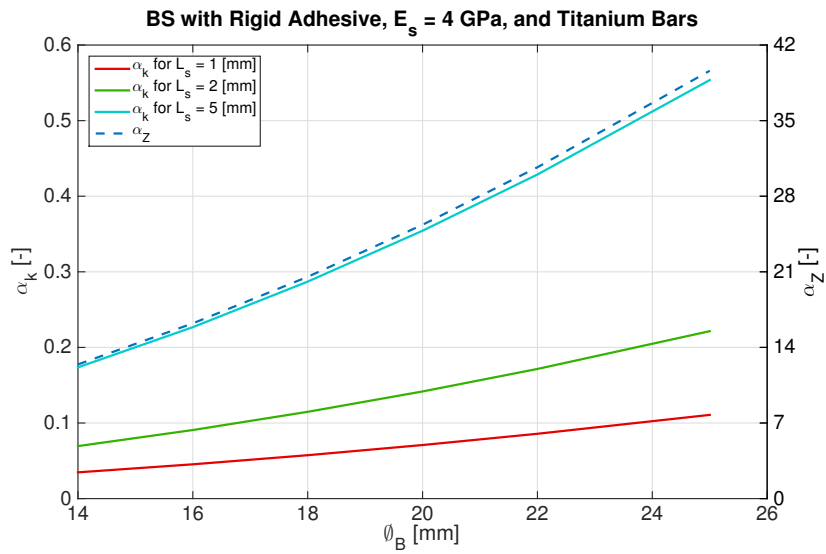


Figure A.22: Ratio comparison for BS, with rigid adhesives and Titanium Alloy bars.

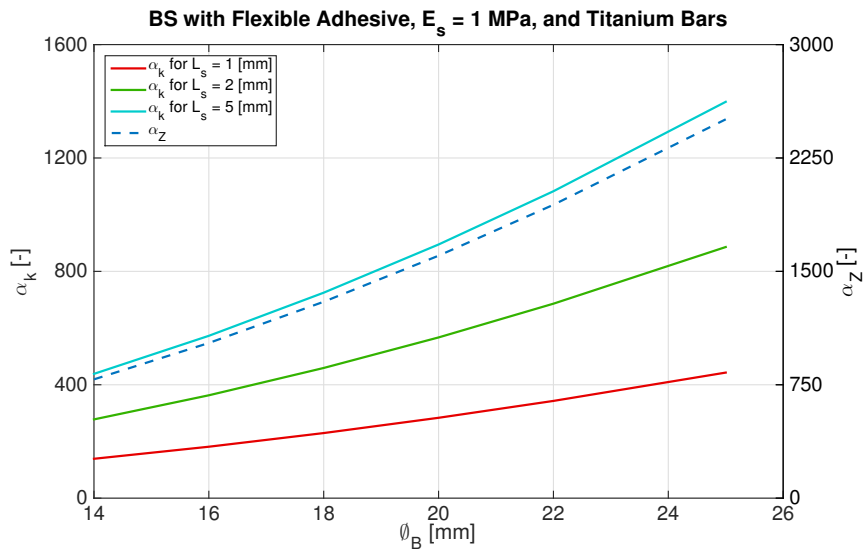
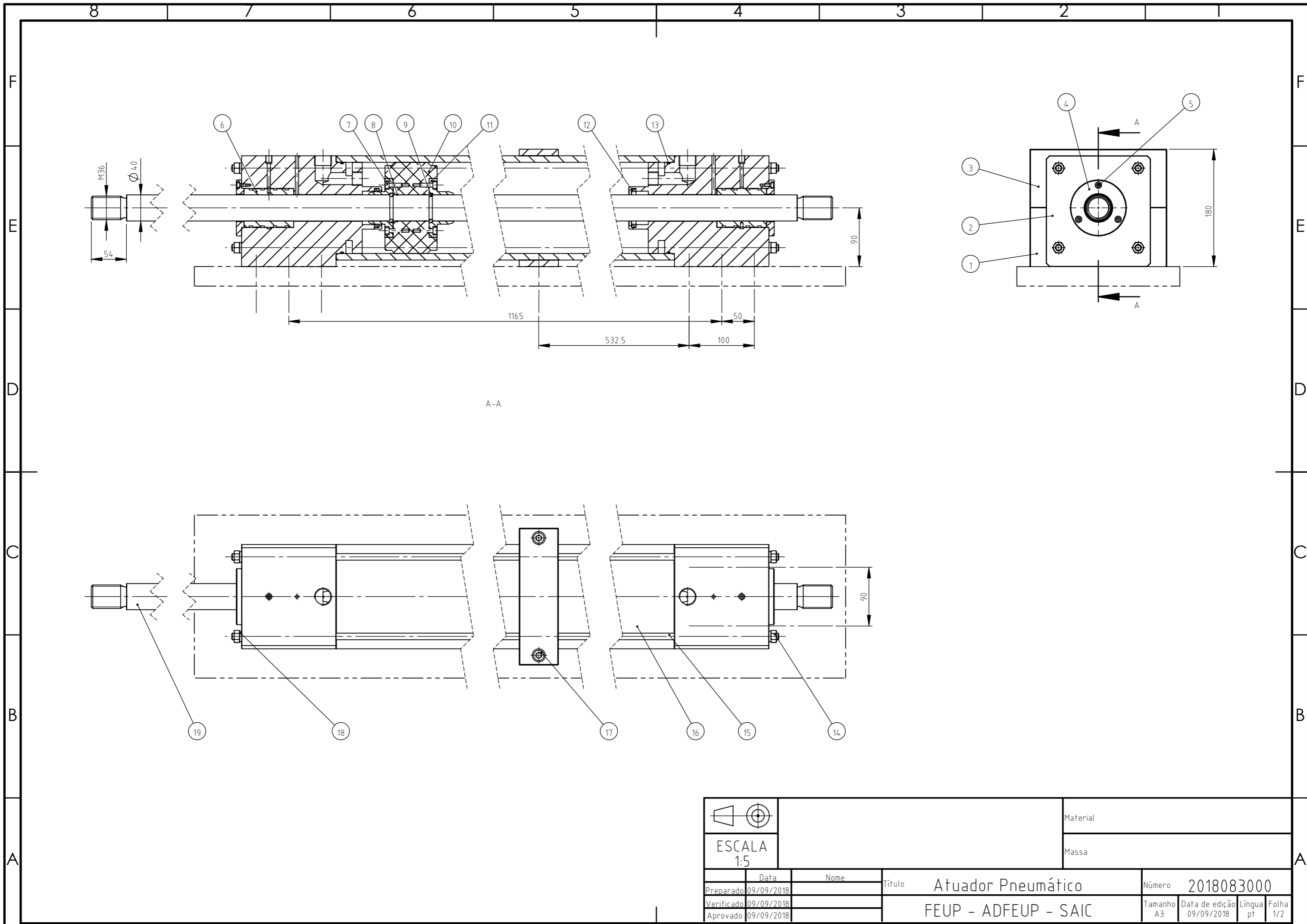
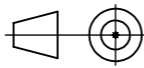


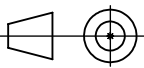
Figure A.23: Ratio comparison for BS, with flexible adhesives and Titanium Alloy bars.

## Appendix B

# Mechanical Drawings



 ESCALA 1:5				Material
				Massa
Preparado	09/09/2018	Nome	Título	Número
Verificado	09/09/2018		Atuador Pneumático	2018083000
Aprovado	09/09/2018		FEUP - ADFEUP - SAIC	Tamanho
				A3
				Data de edição
				09/09/2018
				Língua
				pt
				Folha
				1/2

4		3		2		1	
NUM.	PEÇA	DESCRIÇÃO		QUANT.			
1	Meio Apoio Inferior	2018083008		1			
2	Cabeça	2018083010		2			
3	Meio Apoio Superior	2018083007		1			
4	Tampa de Cabeça	2018083001		2			
5	Parafuso CHC	ISO 4762 M4×10		6			
6	Chumaceira	OAV040MB		2			
7	Parafuso CHC	ISO 4762 M6×20		16			
8	O'ring	Simrit 445 642		2			
9	Chaveta Circular	2018083003		4			
10	Êmbolo	2018083002		1			
11	Tâmpa de Êmbolo	2018083009		2			
12	Vedante	Simrit 425 523		2			
13	O'ring	Simirt 14 452 149		2			
14	Porca Hexagonal	ISO 4032 - M10		8			
15	Tirante	2018083005		4			
16	Corpo de Cilindro	2018083006		1			
17	Parafuso CHC	ISO 4762 M10×60		2			
18	Anilha W10 NF 25-515	W10 NF 25-515		8			
19	Haste	2018083004		1			
		Material					
ESCALA 1:5		Massa					
Data		Nome		Título		Número	
Preparado 09/09/2018				Atuador Pneumático		2018083000	
Verificado 09/09/2018				FEUP - ADFEUP - SAIC		Tamanho	
Aprovado 09/09/2018						Data de edição	
						Língua	
						Folha	
						2/2	

4 3 2 1

F

E

D

C

B

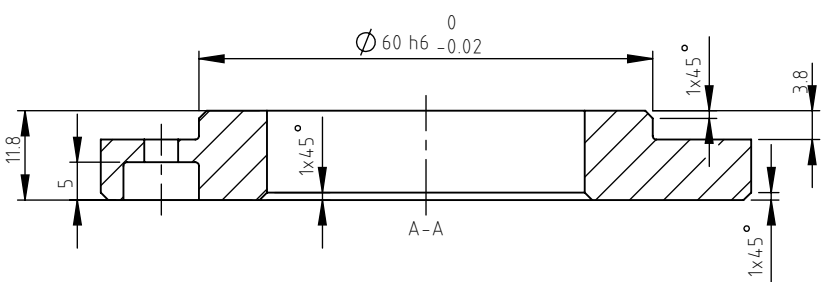
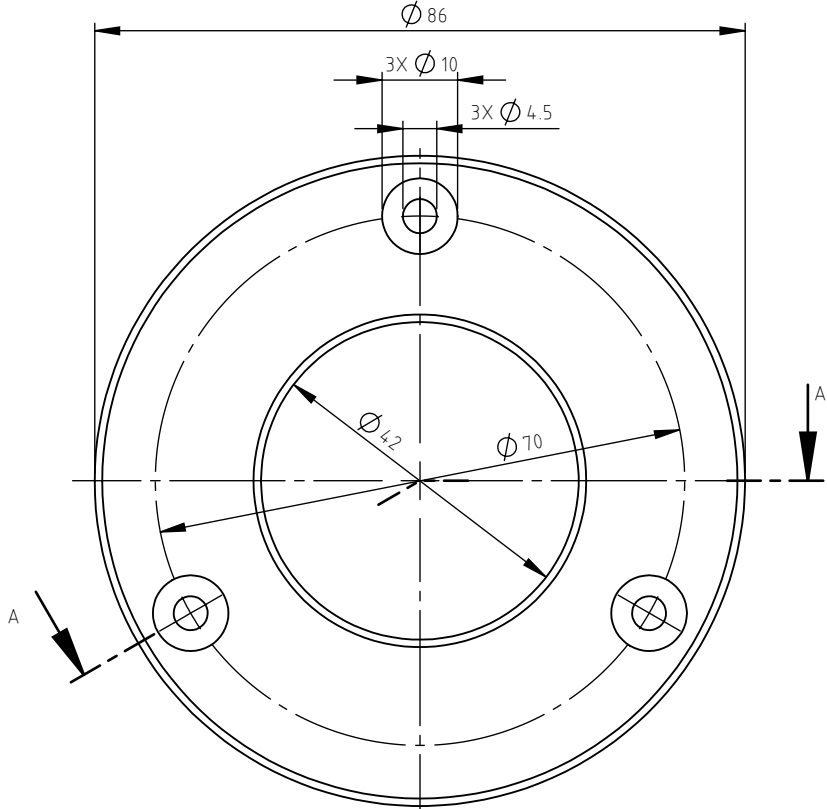
F

E

D

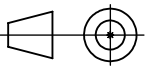
C

B



$\sqrt{\text{Ra } 3.2}$

ISO 2768 - mK  
2 peças



ESCALA  
1:1

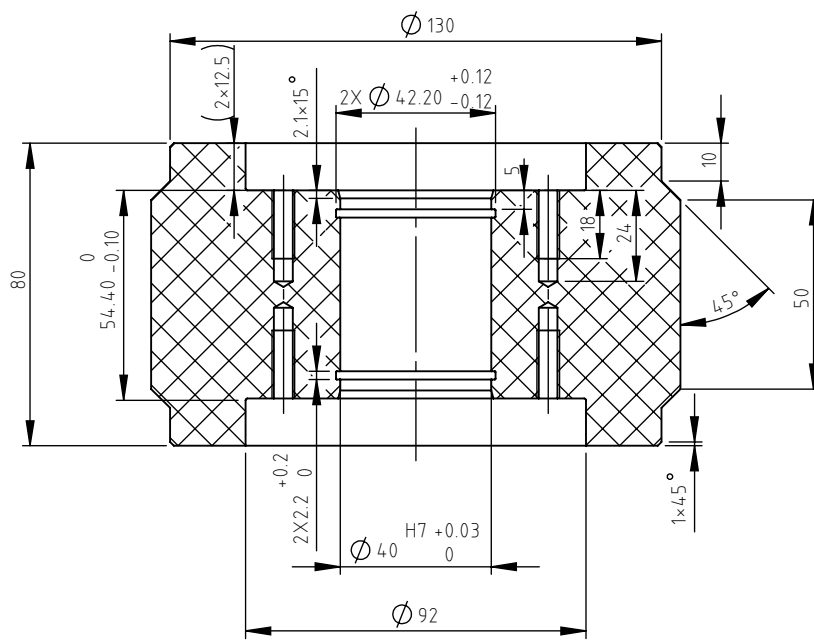
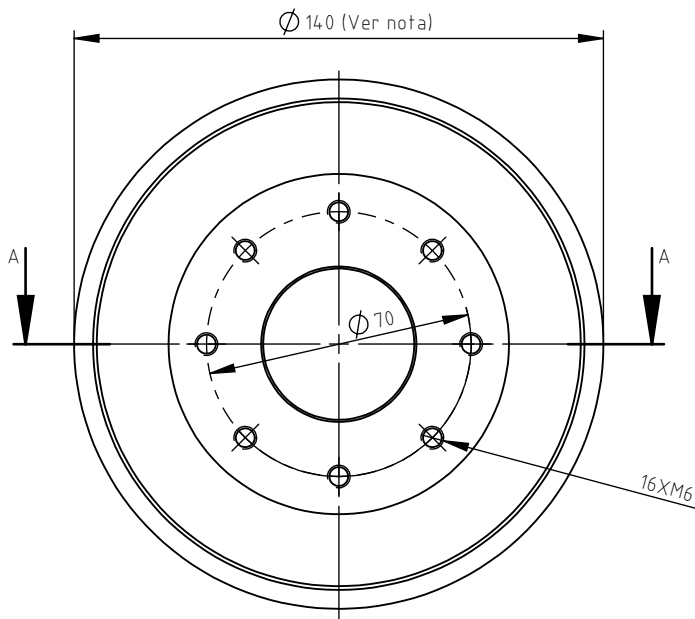
Material Alumínio 6063-T6

Massa

	Data	Nome	Título	Número		
Preparado	08/09/2018		Tampa de Cabeça	2018083001		
Verificado	08/09/2018		FEUP - ADFEUP - SAIC	Tamanho	Data de edição	Língua
Aprovado	08/09/2018			A4	08/09/2018	pt

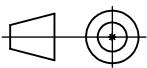
4 3 2 1





ISO 2768 - mK  
1 peça

Nota: Cota interna medida do corpo do (cilindro -  $0,3 \pm 0,01$ )

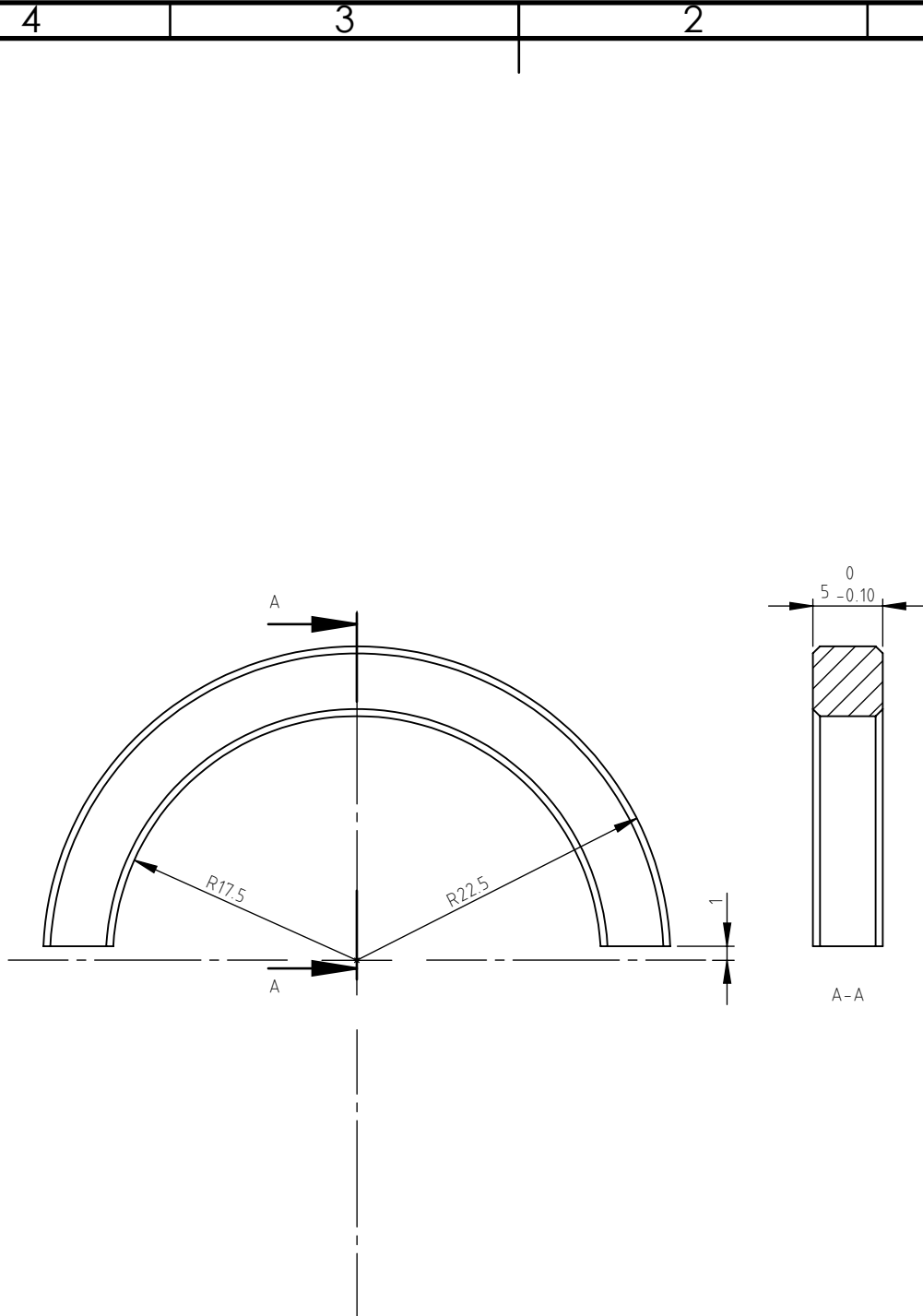


ESCALA  
1:2

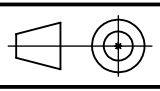
Material Nylon

Massa

Data		Nome		Título	Número	2018083002							
Preparado	08/09/2018					FEUP - ADFEUP - SAIC	Tamanho	Data de edição	Língua	Folha			
Verificado	08/09/2018				A4						08/09/2018	pt	1/1
Aprovado	08/09/2018												



Quebrar arestas  
 ISO 2768 - mK  
 4 peças

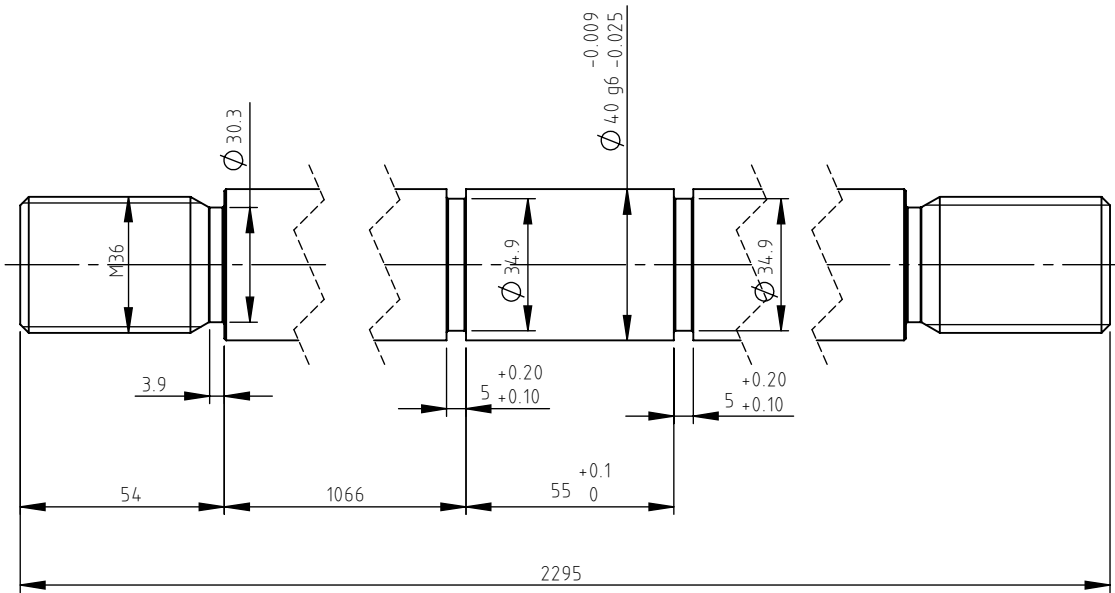


ESCALA  
 2:1

Material Ck45

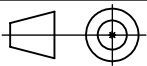
Massa

	Data	Nome	Título	Número			
Preparado	08/09/2018		Chaveta Circular	2018083003			
Verificado	08/09/2018		FEUP - ADFEUP - SAIC	Tamanho	Data de edição	Língua	Folha
Aprovado	08/09/2018			A4	08/09/2018	pt	1/1



$\nabla$  Ra 0.8

Raios de Concordância R0.3  
 Quebrar arestas  
 ISO 2768 - mK  
 1 peça



ESCALA  
1:2

Material Alumínio 6063-T6

Massa

	Data	Nome	Título	Número			
Preparado	08/09/2018		Haste	2018083004			
Verificado	08/09/2018		FEUP - ADFEUP - SAIC	Tamanho	Data de edição	Língua	Folha
Aprovado	08/09/2018			A4	08/09/2018	pt	1/1

4 3 2 1

F

F

E

E

D

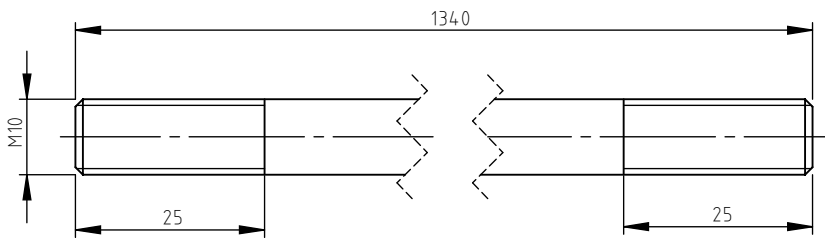
D

C

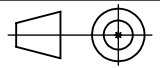
C

B

B



ISO 2768 - mK  
4 peças



ESCALA  
1:1

Material Aço Inox. AISI 304

Massa

A

A

	Data	Nome	Título	Número			
Preparado	08/09/2018		Tirante	2018083005			
Verificado	08/09/2018		FEUP - AD FEUP - SAIC	Tamanho	Data de edição	Língua	Folha
Aprovado	08/09/2018			A4	08/09/2018	pt	1/1

4 3 2 1

4

3

2

F

F

E

E

D

D

C

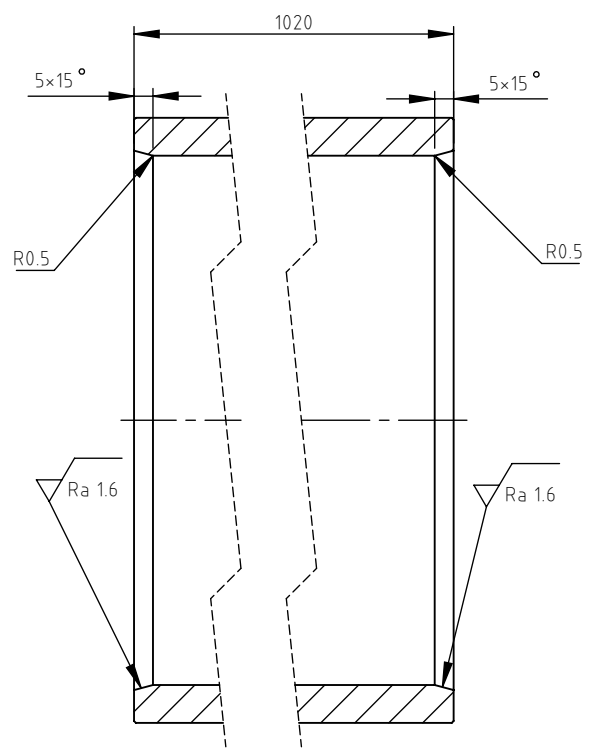
C

B

B

A

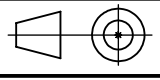
A



A-A

Quebrar arestas  
ISO 2768 - mK

Tubo Hidráulico  $\phi 160 \times \phi 140$  1 peça

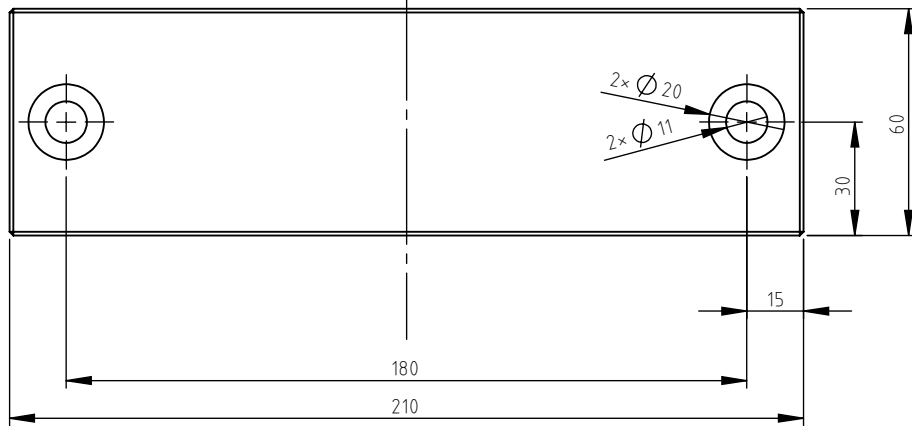
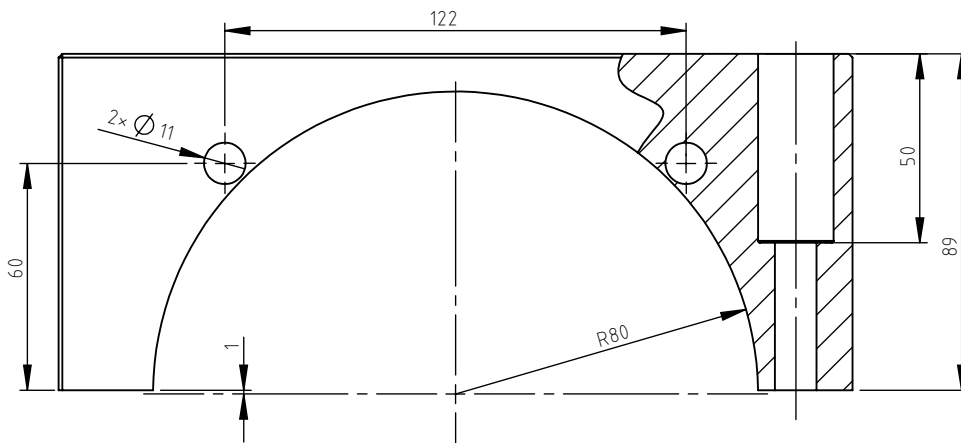


ESCALA  
1:2

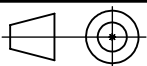
Material Aço St 52.3

Massa

	Data	Nome	Título	Número			
Preparado	08/09/2018		Corpo do Cilindro	2018083006			
Verificado	08/09/2018		FEUP - ADFEUP - SAIC	Tamanho	Data de edição	Língua	Folha
Aprovado	08/09/2018			A4	08/09/2018	pt	1/1



Quebrar arestas  
ISO 2768-mK  
1 peça

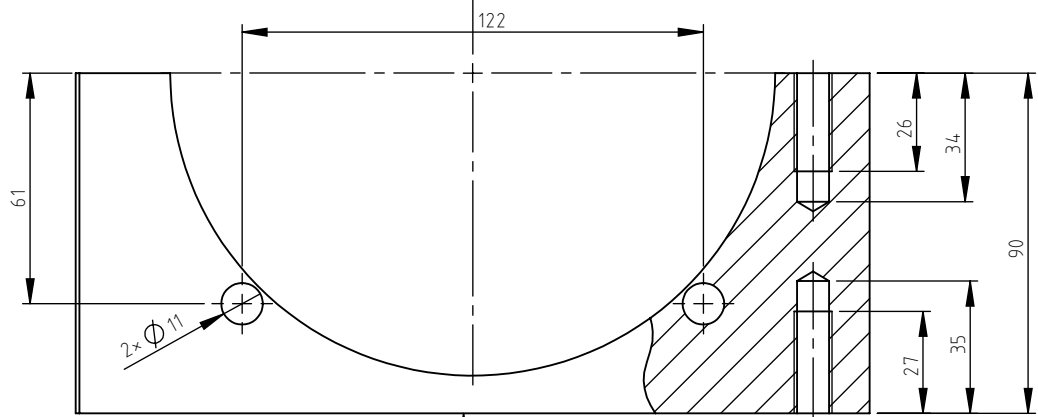


ESCALA  
1:2

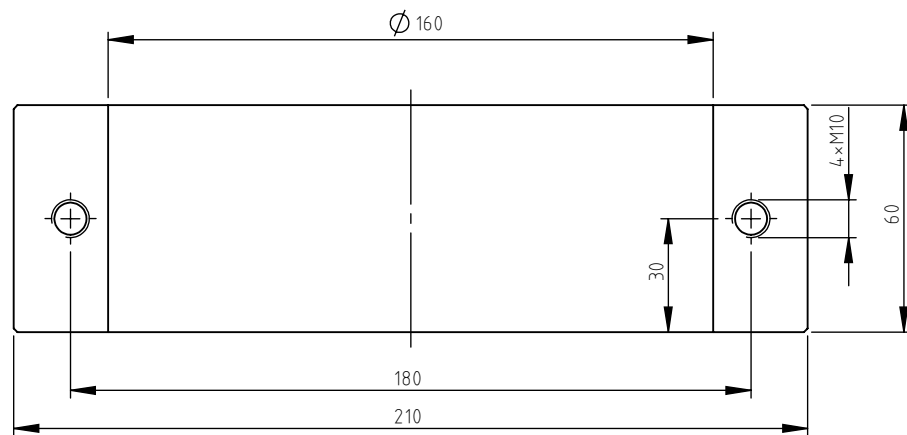
Material Alumínio 6063-T6

Massa

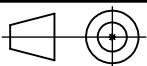
	Data	Nome	Título	Número			
Preparado	08/09/2018		Meio Apoio Superior	2018083007			
Verificado	08/09/2018		FEUP - ADFEUP - SAIC	Tamanho	Data de edição	Língua	Folha
Aprovado	08/09/2018			A4	08/09/2018	pt	1/1



0.16



Quebrar arestas  
ISO 2768-mK  
1 peça

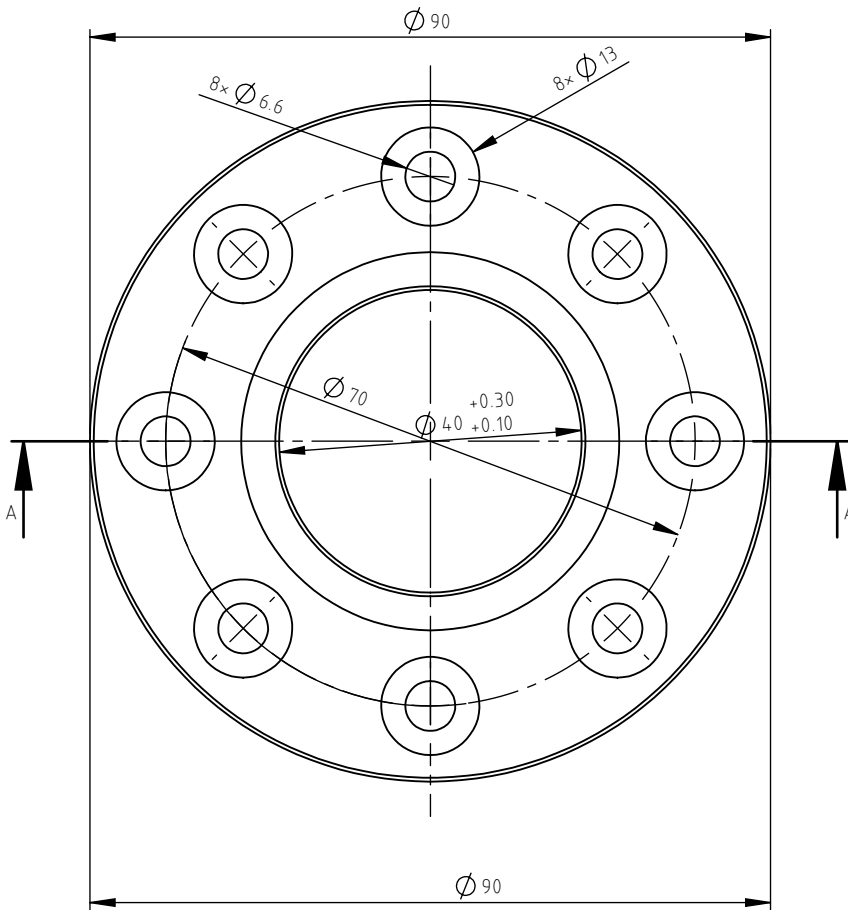
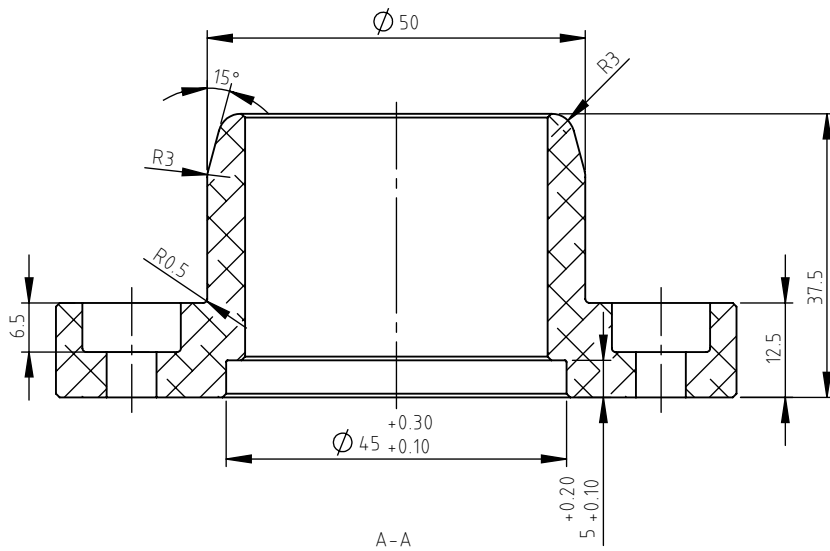


ESCALA  
1:2

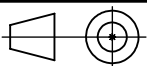
Material Alumínio 6063-T6

Massa

	Data	Nome	Título	Número			
Preparado	08/09/2018		Meio Apoio Inferior	2018083008			
Verificado	08/09/2018		FEUP - AD FEUP - SAIC	Tamanho	Data de edição	Língua	Folha
Aprovado	08/09/2018			A4	08/09/2018	pt	1/1



Chanfros 0.5x45°  
 ISO 2768 m-K  
 2 peças



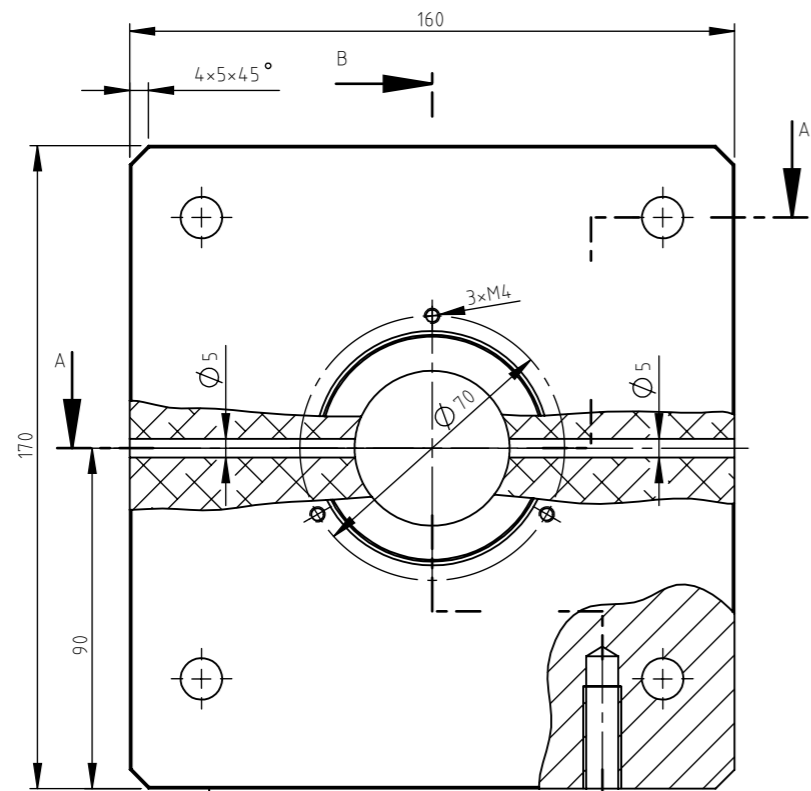
ESCALA  
 1:1

Material Alumínio 6063-T6

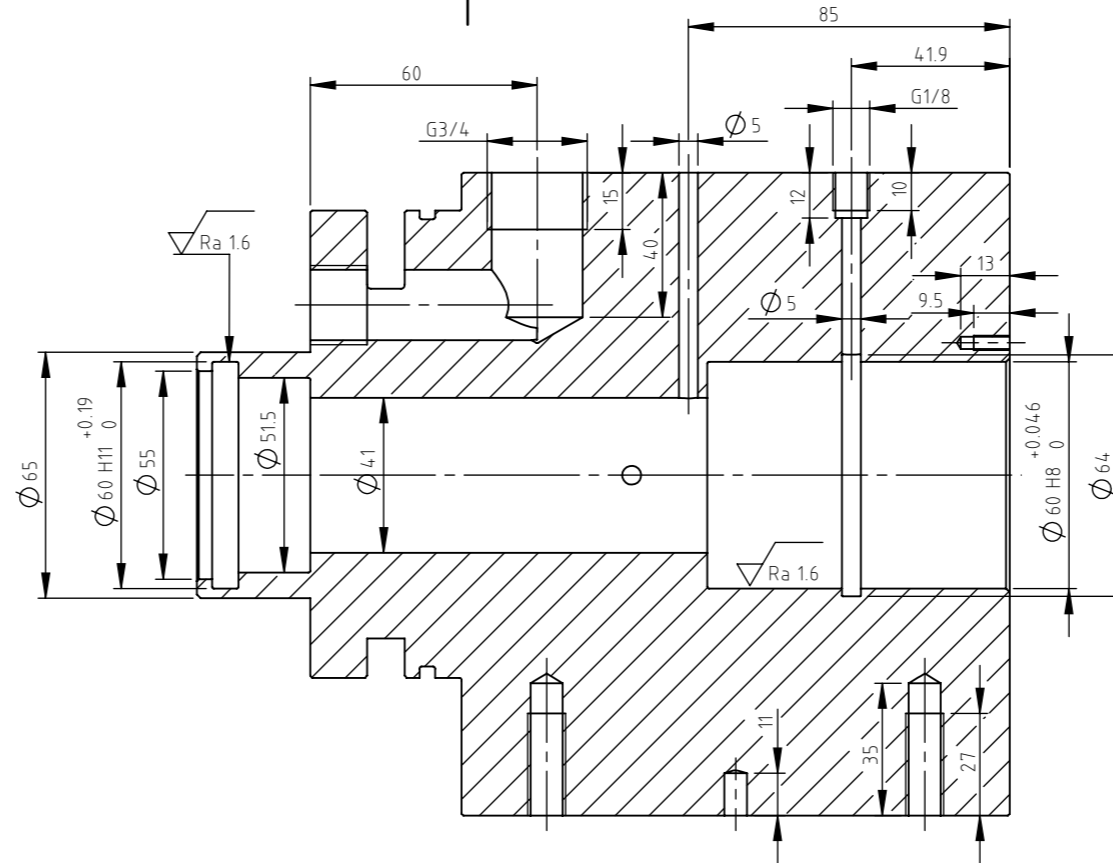
Massa

Preparado	08/09/2018	Nome		Título	Tampa do Êmbolo	Número	2018083009		
Verificado	08/09/2018				FEUP - ADFEUP - SAIC	Tamanho	A4	Data de edição	08/09/2018
Aprovado	08/09/2018					Língua	pt	Folha	1/1

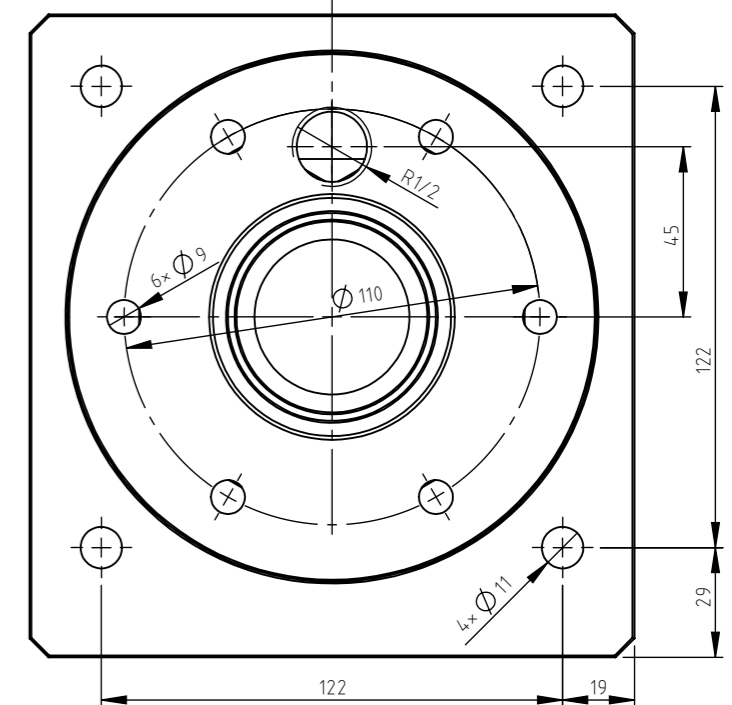




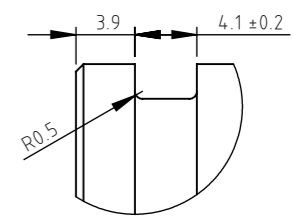
0.16  
Vista de Baixo



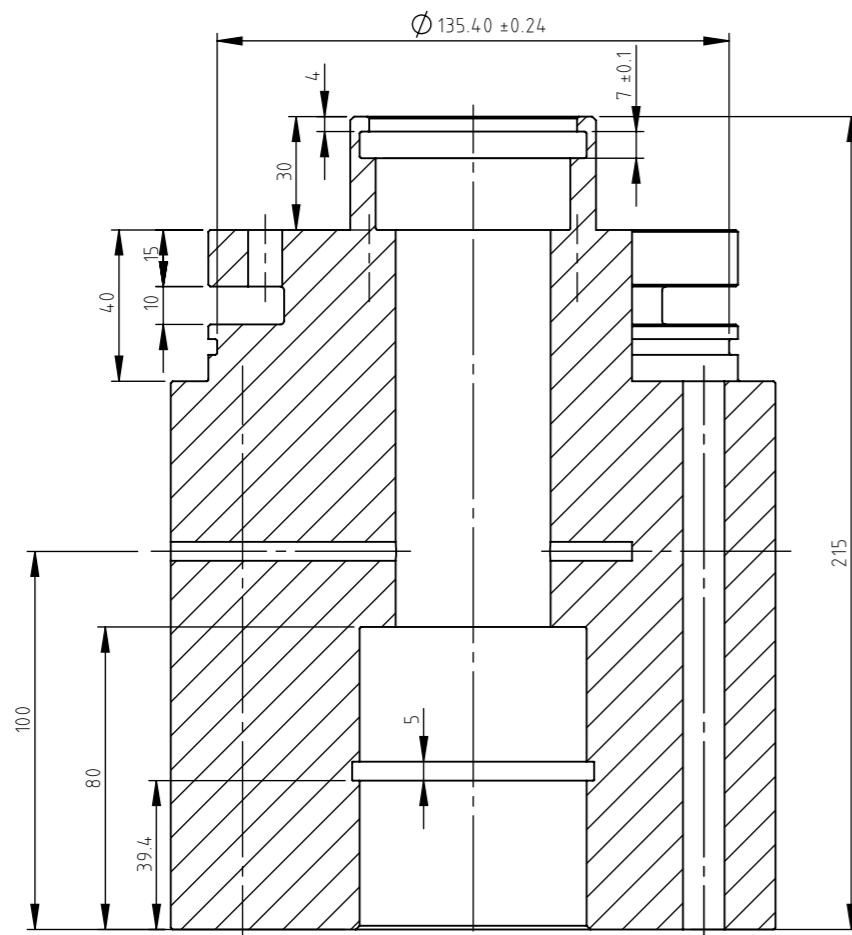
B-B



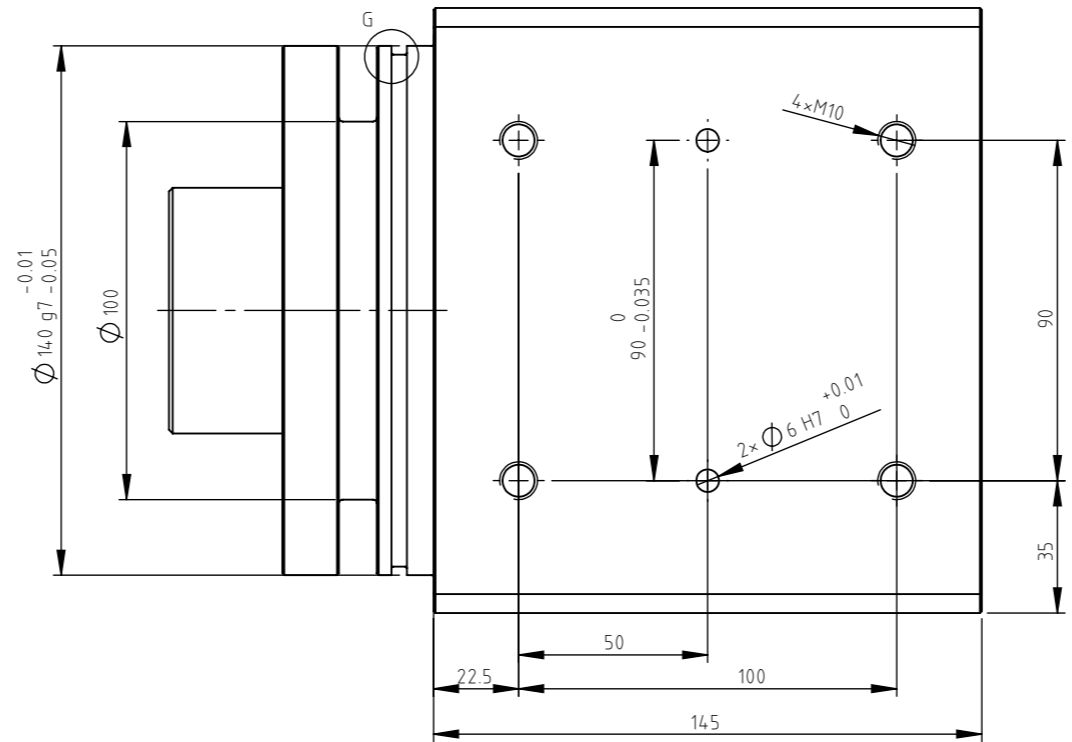
Vista de Baixo



DETAIL G  
SCALE 2 : 1



A-A



Quebrar arestas  
ISO 2768-mK  
2 peças

		Material Alumínio 6063-T6	
ESCALA 1:2		Massa	
Preparado	08/09/2018	Título Cabeça	
Verificado	08/09/2018	Número 2018083010	
Aprovado	08/09/2018	FEUP - AD FEUP - SAIC	
Tamanho	A3	Data de edição	08/09/2018
Língua	pt	Folha	1/1



## Appendix C

# Patent Request

# Split Hopkinson Pressure Bar Setup for Tensile and Compression Testing with Pneumatic Impact Actuator

António Francisco de Galhano Tenreiro<sup>1</sup>, Carlos Manuel de Sousa Moreira da Silva<sup>1</sup>, António Manuel Ferreira Mendes Lopes<sup>1</sup>, Lucas Filipe Martins da Silva<sup>1</sup>.

<sup>1</sup>Department of Mechanical Engineering, Faculty of Engineering, University of Porto, Portugal

## Description

This invention relates to the improved system that tests specimen under high strain conditions, like the Split Hopkinson Pressure Bar technique.

The Split Hopkinson Pressure Bar setup is regularly used to test material specimen in order to obtain mechanical properties under dynamic conditions such as high speed crashes or impact conditions. Normally in either tensile or compression testing, a projectile named Striker Bar (or Striker Tube), is launched by a given actuator (commonly a Gas Gun) and hits the free end of the Input Bar, generating a load pulse. This wave moves towards the other end of the bar, where the Specimen is connected. In this interface, part of the wave is reflected back, while the other part is transmitted to both the Specimen and the Output Bar placed on the other side of the Specimen. Transducers are placed on both the Input and Output Bars in order to measure the waves' amplitudes, and afterwards, are processed to determine the Specimen's behaviour.

It is the belief of the inventors that this technique, while being applied to several types of loading, does not have any versatile setups designed to test Specimen under various types of loadings. Normally, two different setups are used in order to make a compression or a tensile test, respectively, and not both types of test with one given architecture. Furthermore, some of the well established solutions are known to have imperfect control of velocity conditions, as well as energy loss before the collision between the striker and the Input Bars. Some machines may also have unwanted vibration problems. This invention provides a new way of launching the Striking element in one of two directions with high velocities, in order to generate either a tensile loading or a compression loading, while alleviating or eliminating the aforementioned problems.

In the present invention, a pneumatic impact-type symmetric double-rod linear actuator, that can attain high velocities, is presented. This actuator is able to move freely in both directions of its stroke in a horizontal disposition. In order to allow the actuator's piston to move with minimal friction, the rods are supported on air bearings, but can also work with hydraulic or electromagnetic bearings. No part of the rod or piston is in physical contact with the rest of the actuator, meaning that there are no seals, and there are reduced leakages between each chamber as well as the chambers and the atmosphere.

After attaining the desired velocity, a system of mechanical springs act when contacting with a disk, thus storing the energy of the moving rod. When the rod's velocity is low enough, dampers also enter in contact with this disk in order to dissipate part of the kinetic energy. When the mechanical springs start giving back the stored energy to the rod, it starts to move in the opposite direction, and the pressurised chamber that caused the initial motions of the piston will now act as a pneumatic damper that will dissipate the rod's kinetic energy.

The following drawings are provided in order to exemplify the behaviour of the invented actuation system:

- FIGURES 1 and 4 show the actuation system that launches the Striker Bar towards the Input Bar, in order to generate a compression wave for specimen testing.
- FIGURES 2 and 5 show the actuation system that launches the Striker Tube towards an Impact Flange attached to the Input Bar, thanks to a Hook attached to the rod, in order to generate a tensile wave for specimen testing.
- FIGURE 3 shows the pneumatic actuator without any other element associated.

# Claims

1. A Split Hopkinson Pressure Bar setup is presented with a pneumatic actuator that can move in both directions, in order to make compression and tensile tests.
2. The actuator presented in Claim 1 is a pneumatic impact actuator horizontally mounted.
3. The actuator presented in Claim 1 is a symmetric double-rod linear actuator.
4. The actuator presented in Claim 1 can attain velocities of 20 m/s to 50 m/s, depending on the geometric dimensions of the actuator.
5. The rods of the actuator, presented in Claim 1, are supported on air bearings.
6. The rods and piston of the actuator, presented in Claim 1, have no physical contact with the walls of the actuator.
7. The Actuator's rods, as stated in Claim 3, can also be supported with hydraulic or electromagnetic bearings.
8. Near the end of the stroke of the actuator described in Claim 1, a system of mechanical springs and dampers is used to, respectively, store part of the rods kinetic energy, and dissipate the other fraction of the kinetic energy.
9. The energy dissipation system described in Claim 8 can also be made with pneumatic or hydraulic cylinders, or both, that act as mechanical dampers.
10. The energy dissipation system described in Claim 8 can be placed in either sides of the disc in both compression and tensile testing.

# List of Components

The following list of components is common to FIGURES 1 to 5.

1	Output Bar	2	Specimen
3	Input Bar	4	Striker Bar
5	Mechanical Spring & Damper System	6	Disk
7	Pneumatic Impact Actuator	8	Rod
9	Air Bearing	10	Piston
11	Wall	12	Impact Flange
13	Hook	14	Striker Tube

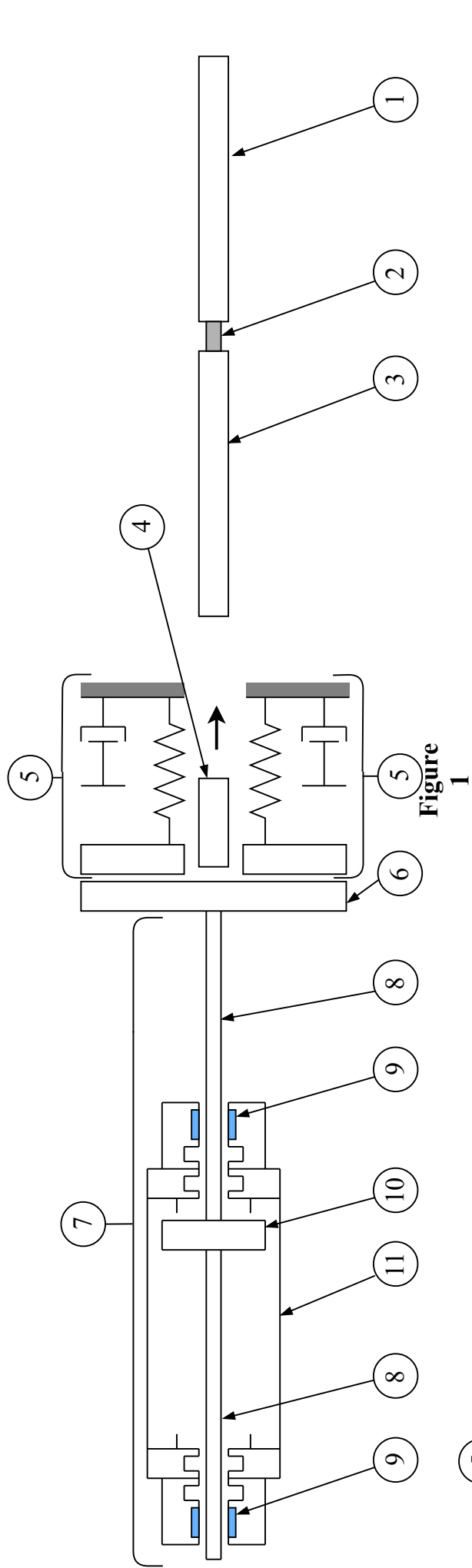


Figure 1

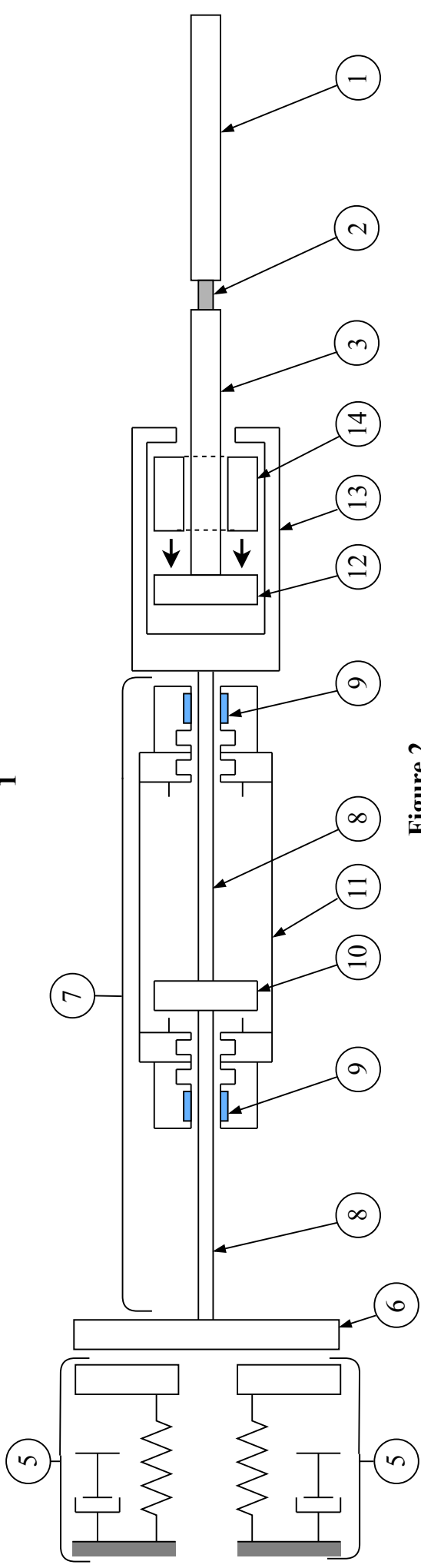


Figure 2

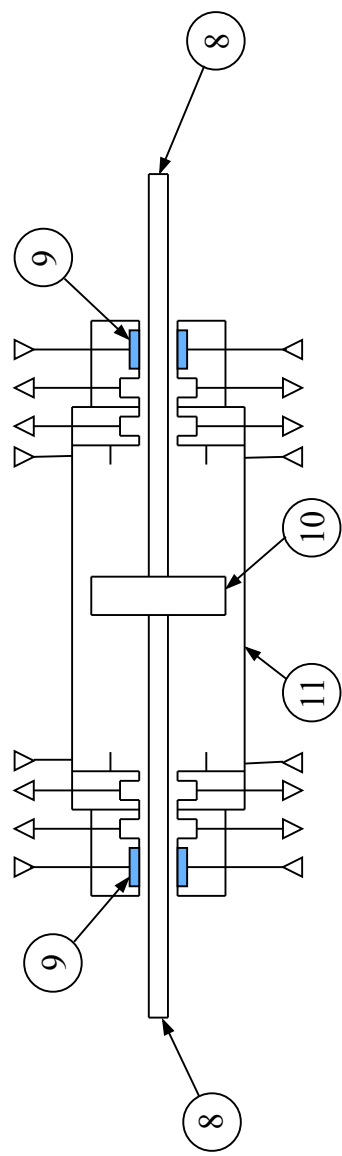


Figure 3

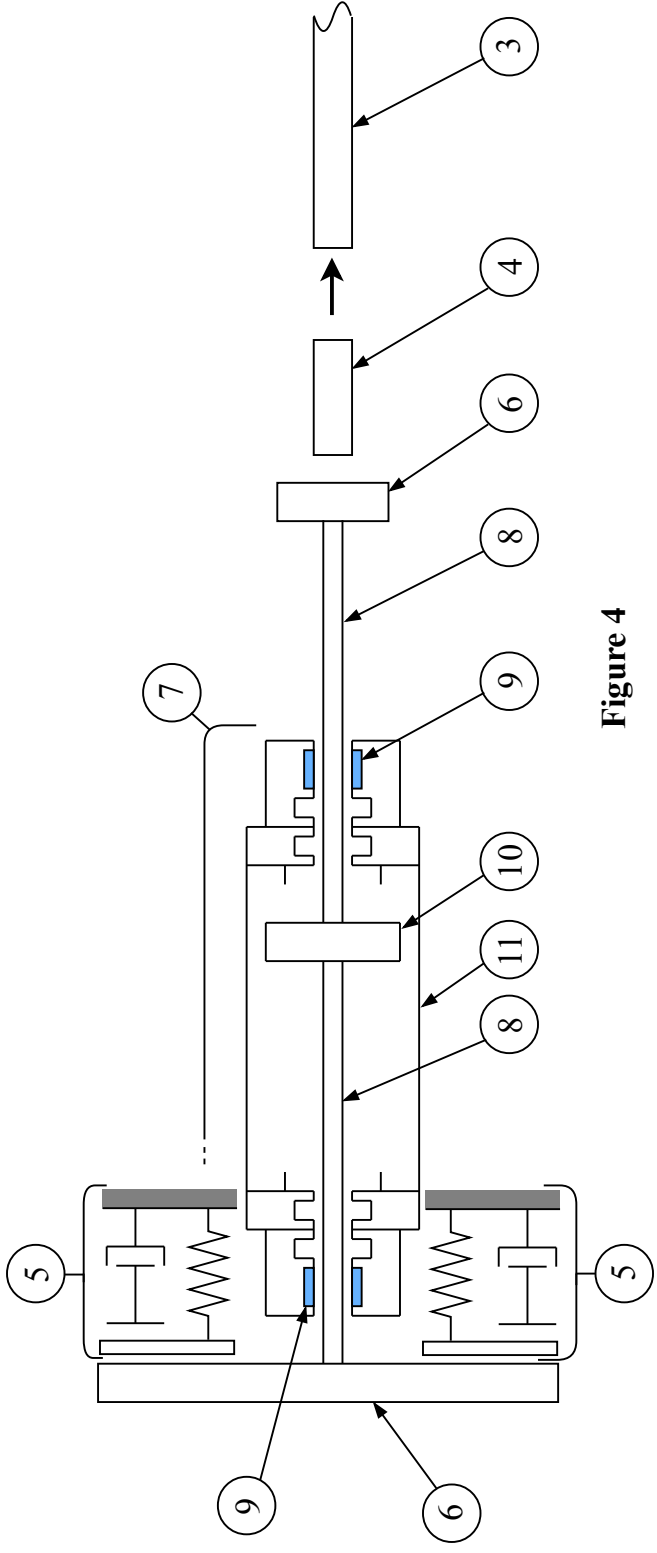


Figure 4

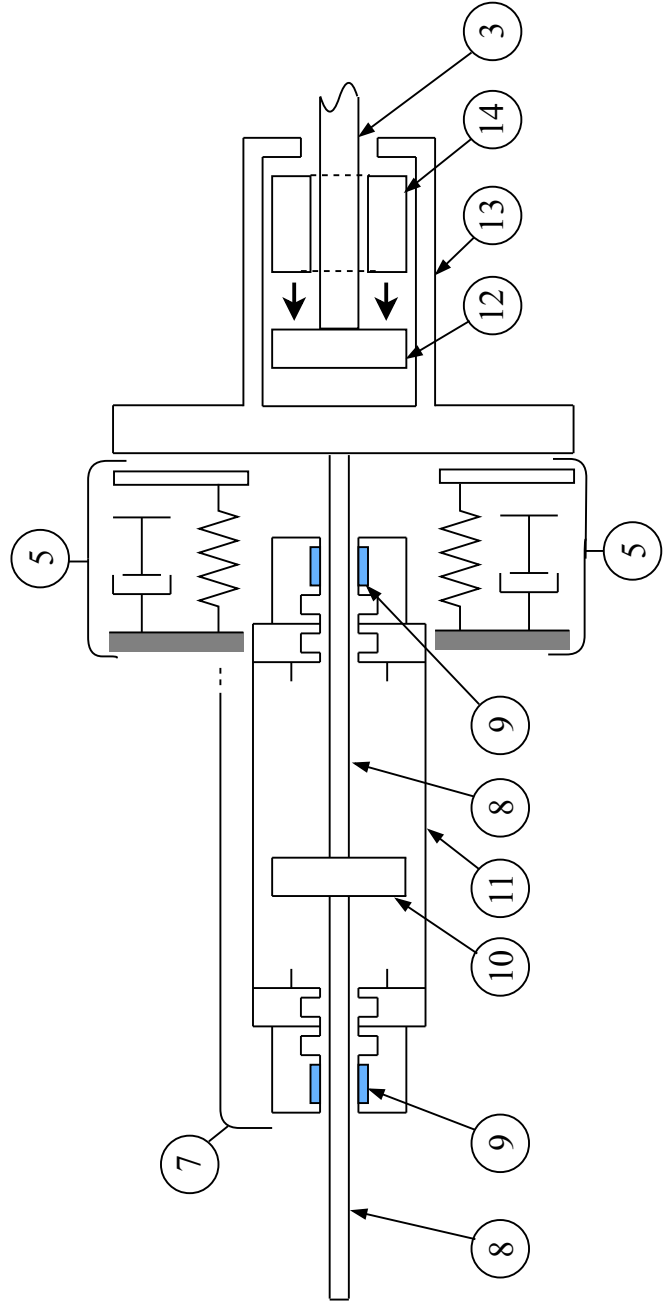


Figure 5